LBL--22046

DE87 001891

Lambda Production in Electron-Positron Annihilation at 29 GeV

Andrew Robert Baden
(Ph.D. Thesis)

Lawrence Berkeley Laboratory
University of California
Berkeley, California 94720

August 1986

This work was supported by the Director, Office of Energy Research, Office of High Energy and Nuclear Physics, Division of High Energy Physics of the U.S. Department of Energy under Contract Number DE-AC03-76SF00098.

Lambda Production in Electron-Positron Annihilation at 29 GeV

Andrew Robert Baden

ABSTRACT

The inclusive cross-section for the production of the singly-strange baryons Λ and $\bar{\Lambda}$, along with the differential cross-sections in momentum and energy, are measured by e^+e^- annihilation at a center-of-mass energy of 29GeV. The charged decay mode $\Lambda \rightarrow p\pi$ is used in a search for polarization. Such a polarization may be used as a check of CP invariance in Λ production. The sample of events with two detected decays is analyzed for correlations in production angle. All results are summarized in the conclusion of this thesis.

Acknowledgments

Any acknowledgement must begin, as I did, with an expression of extreme gratitude to my mother Sandra and father Gary. I wish to thank them especially for giving me the love, support and wherewithal needed. I would also like to thank my siblings Nancy, Chris, Lawrence, Betsy, and Eric for their patience and interest, and especially Eric for sharing so many good meals at a certain North Beach restaurant. Warm thanks goes to my friends Barbara, Janet, and Aniko for seeing me through to the very end from the very beginning, and for sharing cappuccino on more than one occasion. As for Mike Gold, I cannot say how much I've appreciated his surviving an ordeal which makes the Ph.D. process at Berkeley seem like a trip to the candy store, as his friendship and enthusiasm for physics is highly valued. And, as such, I thank Meg Lieberman for her part in keeping Mike alive, not to mention her warm friendship and sense of humor. I thank Gerson Goldhaber for many things, including his guidance, warmth, and example of how one can merge physics with life. For his tremendous sense of humor and knowledge of grammar, not to mention understanding of physics and willingness to advise, a warm thanks is extended to George Trilling. I would also like to thank Jonathan Dorfan for his help, advice and good nature throughout. A sincere thank you to those professors at U. C. Berkeley and San Francisco State University (especially Roger Bland, Oliver Johns, and Jeff Royer) for the teaching of physics at the very highest level and for showing me just how beautiful physics can be. To my many fellow graduate students, especially John Carlstrom, Oren Cheyette, Mike Gold, Jack Miller, Les Rosenberg, Peter Rowson, Tycho Sleator, Mary Silber, Cathy Willis, and Darien Wood, my thanks for the sharing of many meals, conversations, and experiences which for the last five years made a great difference in the quality of my life as a graduate student. A

special acknowledgement goes to Jack Miller and Les Rosenberg for their role in making my pre-graduate school experience at San Francisco State unique. And finally, for her faith, help, intelligence, warmth and love, I wish to acknowledge Donna Duer as a very important part of this whole thing.

Table of Contents

List of Tables

List of Figures

1. Introduction

1.1 Quantum Electrodynamics

The quantum theory of the electromagnetic interactions between charged particles (Quantum Electrodynamics, or QED) is a quantum field theory describing the interaction of the quantum field with the charged particle. The dynamics of this interaction begins with the free-particle solution of a charged spinor with mass m, the Dirac equation [1]

$$p^\mu \gamma_\mu \psi - m\psi = 0$$

where p^μ is understood as the 4-momentum operator acting on the wave function ψ. Interactions (particles in the fields of other particles) are via the minimal addition $p^\mu \rightarrow p^\mu - eA^\mu$ giving

$$p^\mu \gamma_\mu \psi - m\psi = eA^\mu \gamma_\mu \psi$$

where e is the charge of the point particle. (I use the usual convention $\hbar = c = 1$.) It is straightforward to construct a Lagrangean density which gives the correct equations of motion:

$$L = \bar{\psi}(p^\mu \gamma_\mu - eA^\mu \gamma_\mu - m)\psi$$

The interaction term $e\bar{\psi}A^\mu \gamma_\mu \psi$ is the amplitude for the interaction of a spinor ψ with a photon A^μ. Since all physical quantities are built up from the square of amplitudes, the strength of the interaction is characterized by $e^2/4\pi = 1/137$. Since this is a small number, one can use perturbation theory to expand all interactions in powers of e^2 to required precision. R. P. Feynman developed a set of powerful graphical and computational techniques[2] to not only visualize QED processes but calculate quantities. We refer to these aids as Feynman diagrams and assume a familiarity with them.

In e^+e^- interactions, to first order, the interaction cross-section can be built up from 3 primary amplitudes: the exchange amplitude, the two-photon amplitude, and the annihilation amplitude (see Figure 1.1). Bhabha scattering ($e^+e^- \rightarrow e^+e^-$) occurs via the sum of the exchange amplitude and the annihilation amplitude, $e^+e^- \rightarrow \gamma\gamma$ is via the two-photon amplitude, and pair production ($e^+e^- \rightarrow \mu^+\mu^-$ or $\tau^+\tau^-$ or $q\bar{q}$) is via the annihilation amplitude. The cross-section for pair production (μ ,τ, and *quarks*) can be readily calculated and is given by Eqn. 1.1

$$\sigma_0(s) = \frac{4\pi\alpha^2 q^2}{3s}\beta(\frac{3-\beta^2}{2}) \tag{1.1}$$

where s is the square of the center of mass (c.m.) energy, β and q are the velocity and charge of the produced particles, and α is the fine structure constant $e^2/4\pi$ as mentioned above. The PEP energy, $s = (29\text{GeV})^2$, is above threshold for pair production of electrons, muons, taus, and up, down, charm, strange, and bottom quarks. Table 1.1 lists the possible pairs with the corresponding mass and charge. Note that for the u,d,s,c, and b quarks the mass is an effective mass.

1.2 Weak Interactions

Weak interactions add further complication. Since the initial state is e^+e^-, the important weak interaction coupling is to the neutral vector boson Z^0, and is of the form $\bar{\psi}Z^\mu\gamma_\mu\psi$ where ψ can be the wave function for $e, \mu, \tau, u, d, s, c, b$. Therefore, the annihilation amplitude must include not only the photon field A^μ but the weak neutral field Z^μ. Since at these energies the strength of the weak field relative to the electromagnetic field is determined mainly by the mass of the virtual Z^0, the addition of the Z^0 amplitude contributes little to the total cross-section, and then only in the interference term. However, the addition of the weak interaction in the cross-section allows for some parity violation. For $e^+e^- \rightarrow \mu^+\mu^-$, the forward-backward asymmetry due to the presence of the Z^0

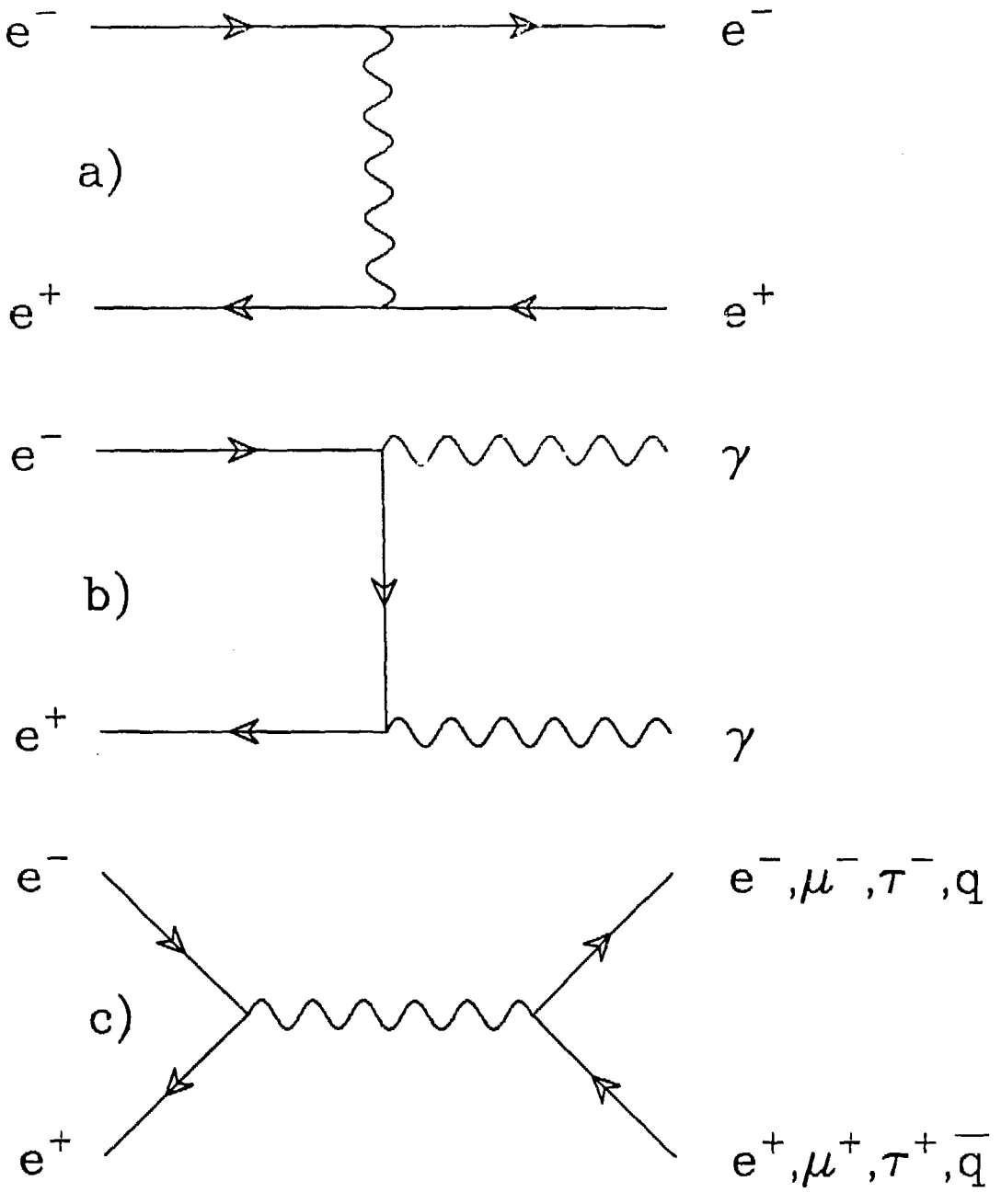

Figure 1.1. QED amplitudes to $O(\alpha^2)$. a) exchange amplitude, b) 2-photon production, and c) annihilation amplitude

Table 1.1. Primary fermions produced in e^+e^- annihilation at $\sqrt{s} = 29\text{GeV}$.

particle	mass	charge
e	.5 MeV $/c^2$	-1
μ	106 MeV $/c^2$	-1
τ	1.8 GeV $/c^2$	-1
up (u)	0.3 GeV $/c^2$	+2/3
down (d)	0.3 GeV $/c^2$	-1/3
strange (s)	0.5 GeV $/c^2$	-1/3
charm (c)	1.5 GeV $/c^2$	+2/3
bottom (b)	5.0 GeV $/c^2$	-1/3

amplitude is of order 6% [3].

1.3 HADRONIZATION

In the real world, what one observes is not $e^+e^- \rightarrow q\bar{q}$ but $ee \rightarrow HADRONS$. The process of hadronization (whereby a $q\bar{q}$ pair gives rise to hadrons) is a low energy process whereby quarks and gluons interact via the strong interaction to produce bound states (hadrons). Current understanding of the strong interaction is described by a gauge theory called Quantum Chromodynamics (QCD), a theory which at low energies is exceedingly hard to utilize for the purpose of calculations. We thus must rely on phenomenological models for hadronization. Monte Carlo techniques, in which we try to simulate this process, are thus forced to focus on characterizing the dynamics of hadronization. For instance, in the process $e^+e^- \rightarrow q\bar{q}$, the $q\bar{q}$ is produced back to back in the lab frame, each with an energy of 14.5GeV. Hadrons should then form along the quark directions giving jet-like event topologies. Also, the distribution of momentum perpendicular to the jet axis within each jet is characterized by a gaussian with some width. That width is a parameter which is measured in the data, and used by the Monte

Carlo program to ensure reliable simulation.

There are many different schemes employed to simulate hadronic events. What all have in common, however, is that they require parameters which must be input. What is lacking are the first principles from which to start. Since Monte Carlo simulation is an extremely important tool used in e^+e^- physics (used for example to determine detector efficiencies, characterize the effect of detector resolution on produced quantities, etc.), I will summarize two widely different and often used schemes in simulating the hadronization process: the Feynman-Field [4] (FF) independent fragmentation scheme and the Lund [5] (LUND) string fragmentation scheme (reference).

1.4 Feynman-Field Fragmentation

In the FF scheme, the primary quarks fragment independently of each other to produce the final state hadrons. For each primary quark, a $q\bar{q}$ pair is pulled from the vacuum, or sea. The primary quark is then combined with one of the vacuum quarks to make a meson. The meson has a momentum fraction governed by a fragmentation function $D(z)dz$, which is the probability that the meson has the momentum fraction between z and $z+dz$ of the parent quark. For the light quarks u, d, s

$$D(z) \propto (1-z)^r$$

where r is a parameter measured to be ~ 0.7. For the heavy quarks c, b, the fragmentation function is of the form[6]

$$D^Q(z) \propto [z(1-\frac{1}{z}-\frac{\epsilon_Q}{1-z})^2]^{-2}$$

where Q is the flavor of the heavy quark, $\epsilon_Q = (m_q/m_Q)^2$ ($\epsilon_c \sim 0.3, \epsilon_b \sim 0.03$), and q is the final unpaired quark. (see Figure 1.2 for fragmentation functions and the thesis of Heidi Schellman[7] for a detailed description.) Fragmentation of gluons

in $q\bar{q}g$ and $q\bar{q}gg$ are handled either by assigning a random quark flavor to the gluon and fragmenting as if the gluon had that quark flavor or by replacing the gluon by a $q\bar{q}$ pair and fragmenting as above. The momentum fraction of each quark from the gluon is given by the Altarelli Parisi [8] splitting function

$$P_{g\to q\bar{q}}(z) = \frac{z^2 + (1-z)^2}{2}$$

The formation of baryons is simply an extension to the formation of mesons. Instead of creating a $q\bar{q}$ pair from the vacuum, a $qq\bar{q}\bar{q}$ "di-quark" pair is created. One then combines one of each quark from a $q\bar{q}$ with two quarks from the di-quark system to form a color singlet 3-quark bound state. The ratio of di-quark pairs to quark pairs is via a parameter determined from the data. Best estimates are $P(qq)/P(q) = 10\%$.

1.5 Lund Fragmentation

In the LUND scheme, the produced quarks are connected by massless colorless string fields. The energy in the field is a linear function of the separation distance between the quarks characterized by a constant string energy density $k \sim 1\,\mathrm{GeV}/fm$. Gluons are considered kinks in the string with localized energy. As the quarks move apart, the energy in the string increases up to some limit, whereupon the string breaks to form a new $q\bar{q}$ pair. The primary quark combines with the $\bar{q}$ from the pair to form a color singlet meson, with momentum fraction z given by the Lund fragmentation function

$$f(z) = \frac{1}{z} z^{a_\alpha} \left(\frac{1-z}{z}\right)^{a_\beta} e^{-bm_\perp^2/z}$$

where α and β label quark flavors, b is some constant, and $m_\perp^2$ is the "transverse mass" of the resultant hadron ($m_\perp^2 = E^2 - p_\perp^2$). The usual values for the a_α (and

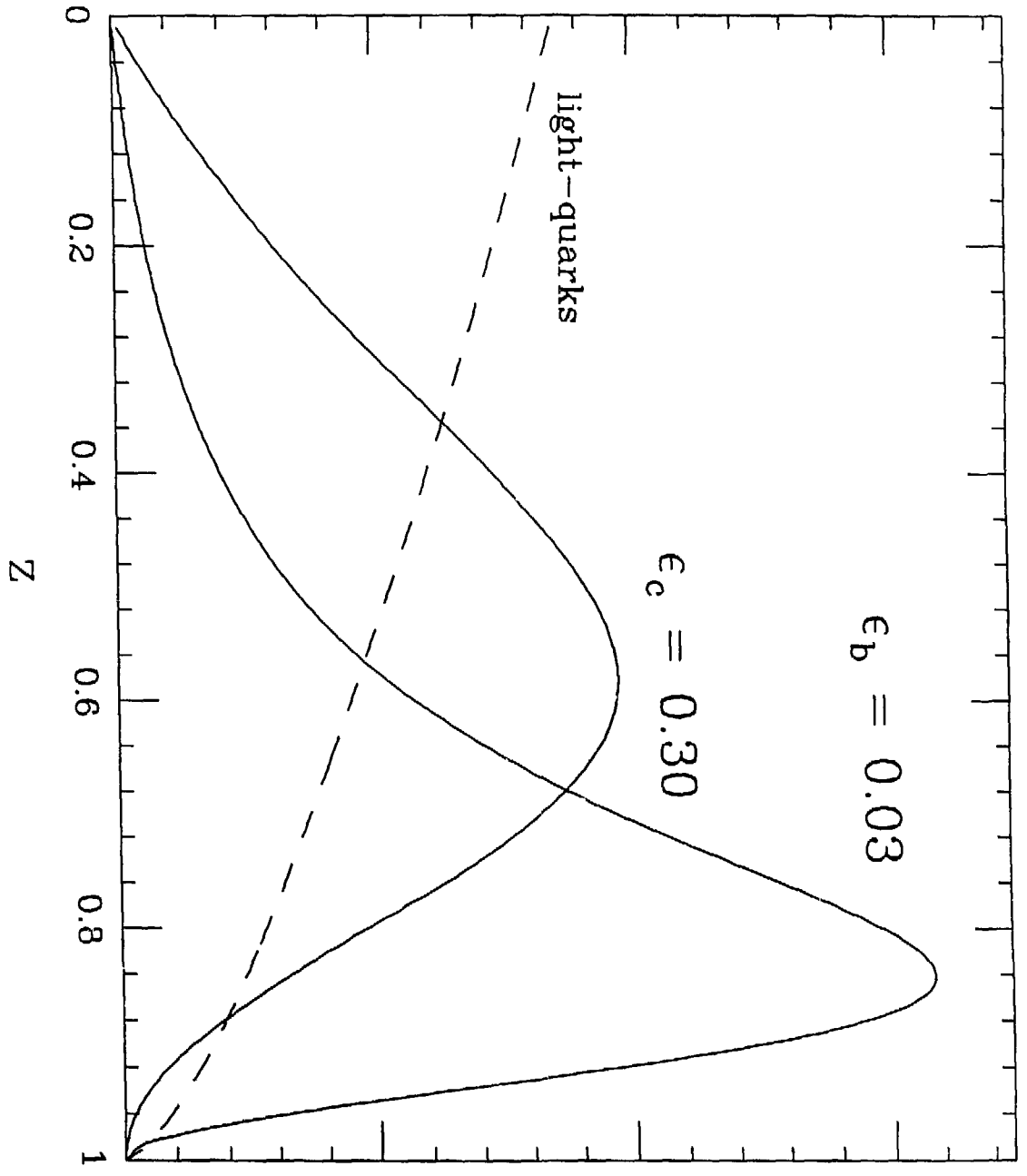

Figure 1.2. Fragmentation functions for light u, d, s quarks and heavy c, b quarks

thus for all flavors) and for b are 1.0 and 0.7 respectively, giving

$$f(z) = (\frac{1-z}{z})e^{-.7m_\perp^2/z}$$

This peculiar form of the fragmentation function is motivated by the problem of what to do with the last $q\bar{q}$ pair. If one uses some other simpler form for the fragmentation function and chooses the momentum of the final $q\bar{q}$ pair to force the corresponding hadron to be on-shell, then characteristics of an event will be dependent on which quark is fragmented first, and will result in an asymmetry in rapidity of final hadrons. The above fragmentation function ensures that all hadrons are automatically on-shell, and that rapidity distributions are symmetric (hence the so-called "Symmetric Lund Model")[5]. Baryons are included with an extension similar to that used in FF, characterized by the same di-quark to single quark probability ratio.

1.6 Baryon Production

The formation of baryons in e^+e^- annihilation is not well understood. The Monte Carlo schemes as noted above characterize baryons as being "special" hadrons included in the event with some probability. This probability, in the form of ratios of the probability of pulling a di-quark pair to a quark pair out of the sea, is assigned a value such that the hadronic rate $(\sigma(e^+e^- \rightarrow Baryon + X)/\sigma_{hadronic})$ in the Monte Carlo is in agreement with the data. The formation of massive partons from the vacuum state due to the presence of the color field is a quantum mechanical tunneling phenomena, and thus favors the low mass partons. For this reason, the quarks u and d are favored. The suppression of s quarks to isospin quarks is a parameter in Monte Carlo schemes of order $20-30\%$, with the heavier c and b quarks fully suppressed. The di-quark pair is thus usually comprised of the isospin partons u and d. The LUND scheme adds

the possibility that the di-quark pair contains s quarks, and recent measurements (HRS paper) have found the suppression $[P(us)/P(ud)]/[P(s)/P(d)]$ to be consistent with 1. (us means isospin plus strange.) The reader is referred to Appendix A for a naive prediction of the $\Lambda/\bar{\Lambda}$ hadronic rate.

In this thesis, we will present results of a search for the $\Lambda/\bar{\Lambda}$ in e^+e^- annihilation. Topics include the differential cross-sections $d\sigma/dp$ and $(s/\beta)\ d\sigma/dx$ where $x \equiv E_\Lambda/E_{beam}$, the hadronic rate for producing $\Lambda/\bar{\Lambda}$, possible $\Lambda/\bar{\Lambda}$ production polarization and CP violation, and correlations in events with Λ-$\bar{\Lambda}$, Λ-Λ, or $\bar{\Lambda}$-$\bar{\Lambda}$.

1.7 Radiative Corrections

The cross-section given in (1) can be calculated in a straight- forward fashion using the tree level diagram with a photon propagator (see Figure 1.1(c)). This cross-section is correct to $O(\alpha^2)$. To calculate the cross-section for $e^+e^- \to q\bar{q}$ to $O(\alpha^3)$ one must include vacuum polarization, vertex correction, and self-energy diagrams (see Figure 1.3). This introduces infra-red divergences. Now, if one calculates $e^+e^- \to q\bar{q}\gamma$, similar infrared divergences appear in the initial-state photon momentum. (For $q\bar{q}$ production initial-state radiation dominates over final-state radiation.) However, if we combine the two processes and calculate $e^+e^- \to q\bar{q}(\gamma)$ where (γ) means with or without a final state direct photon, we get a cancellation in the infra-red divergences. The cross-section for $e^+e^- \to q\bar{q}(\gamma)$ can then be written

$$\sigma(s) = \sigma_0(s) + \sigma_1(s, k_0) + \int_{k_0}^{E_{beam}} \frac{d\sigma_2(s')}{dk} dk$$

where σ_0 is the tree level $e^+e^- \to q\bar{q}$ cross-section, σ_1 is the finite part to $O(\alpha^3)$ of $e^+e^- \to q\bar{q}$, $s = (29\text{GeV})^2$ is the c.m. energy, σ_2 is the finite part of the $e^+e^- \to q\bar{q}\gamma$ cross-section, k_0 is the infra-red cutoff parameter, and $s' = s(1 - 2k_0/\sqrt{s})$ is the

reduced c.m. energy due to the radiative γ. One can then write

$$\sigma(s) = \sigma_{NORAD}(s, k_0) + \sigma_{RAD}(s', k_0)$$

where $\sigma_{NORAD} = \sigma_0(s) + \sigma_1(s, k_0)$ above and σ_{RAD} is the remaining term. σ_{NORAD} can then be written as Eqn. 1.2

$$\sigma_{NORAD}(s, k_0) = \sigma_0(s)[1 + \delta(s, k_0)] \tag{1.2}$$

The $\delta(s, k_0)$ can be calculated readily [9]. For $s = (29\text{GeV})^2$ and $k_0 = 1\% E_{beam}$, $1 + \delta = .7327$ (see Figure 1.4). In e^+e^- interactions, physics quantities are often dependent on whether there was initial-state radiation (e.g. the multiplicity in hadronic events goes roughly logarithmically with center of mass energy, which is lowered by initial-state radiation), and so it is important that the Monte Carlo matrix element generate events for $e^+e^- \rightarrow q\bar{q}(\gamma)$, and with the correct radiative and non-radiative normalizations.

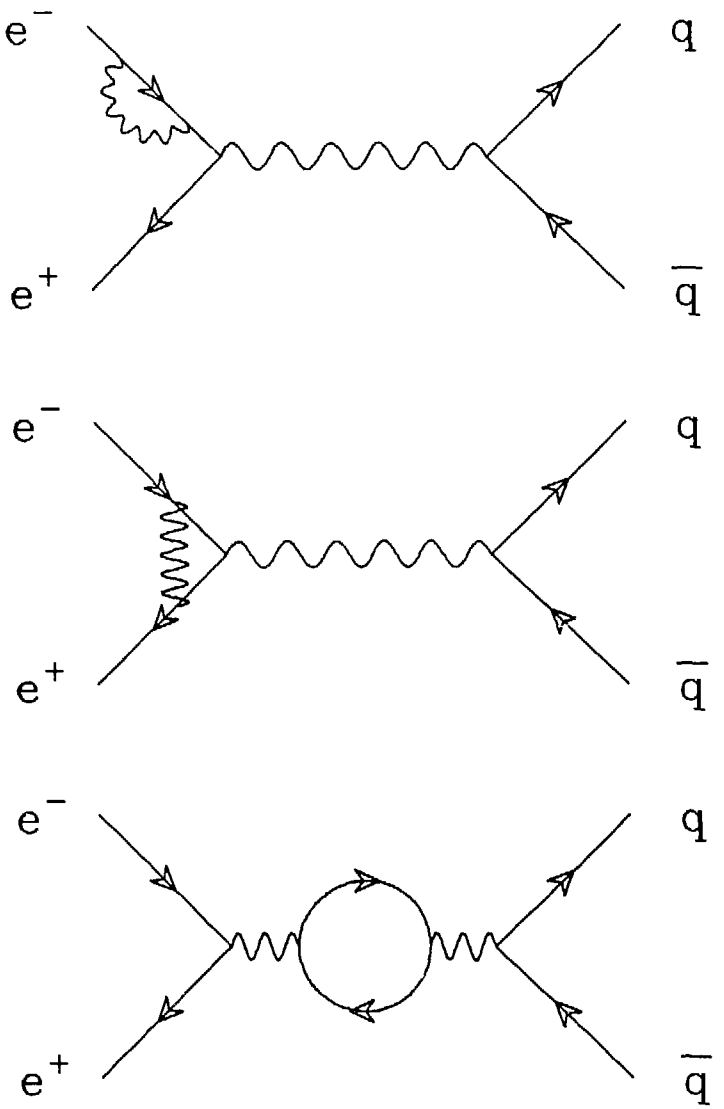

Figure 1.3. $O(\alpha^3)$ corrections to $e^+e^- \rightarrow q\bar{q}$ cross-section.

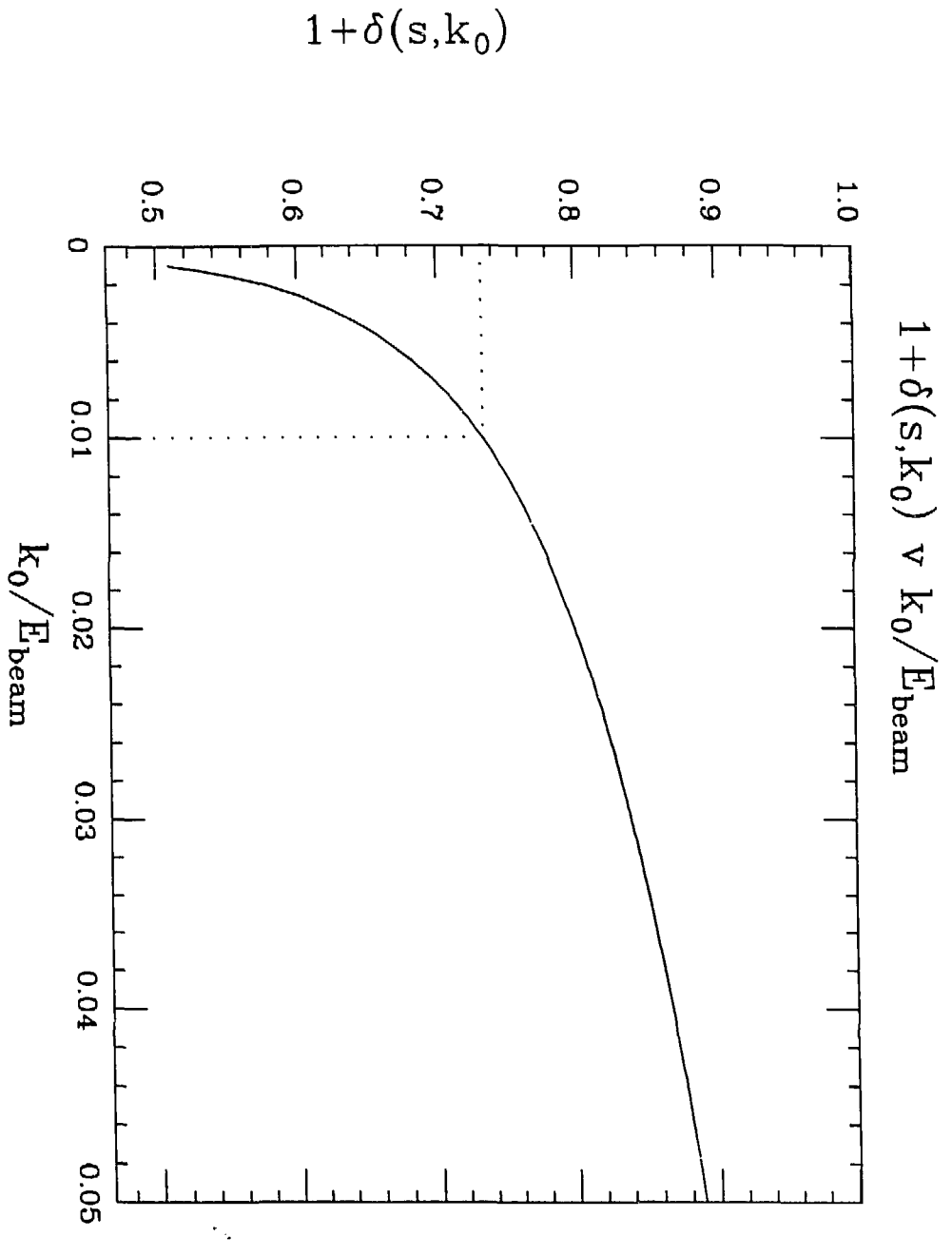

Figure 1.4. The quantity $1 + \delta(s, k_0)$ used in radiative corrections[9]. Dotted line gives coordinates $k_0 = 1\% E_{beam}$ and $1 + \delta(s, k_0) = .7327$.

2. The Apparatus

2.1 PEP

In April 1972, a Positron-Electron-Proton (PEP) colliding beam facility was jointly proposed[10] by the Stanford Linear Accelerator Center (SLAC) and the Lawrence Berkeley Laboratory (LBL). The proposal called for both a proton and electron-positron storage ring to study the physics of e^+p, e^-p, and e^+e^- collisions with a designed luminosity of $\sim 10^{32} cm^{-2} sec^{-1}$ using essentially existing technology. Further studies over the next few years resulted in dropping the proton storage ring proposal as the technological uncertainties grew. In April 1974, a proposal for the Positron-Electron-Project (PEP) with beam energies of 15GeV and design luminosity of $10^{32} cm^{-2} sec^{-1}$ was presented[11] to the U.S. Atomic Energy Commission. The cost was estimated to be \$61.8 million in FY84 dollars. In the fall of 1979, the PEP facility was completed with successful e^+e^- collisions, on schedule and at the estimated cost.

Each beam at PEP consist of 3 "buckets" of electrons or positrons with about $N = 2.8 \times 10^{11}$ particles per bucket and an orbital frequency of $\nu \sim 136 kHz$. The current in each beam is given by the formula $I = N\nu q \sim 6mA$. The "instantaneous luminosity", defined as the reaction rate per unit cross-section, is given by

$$L = \frac{N_+ N_- N_b \nu}{A} \sim 2.0 \times 10^{31} cm^{-2} sec^{-1}$$

where N_+ (N_-) is the number of particles per bunch in the e^+ (e^-) beam, N_b is the number of bunches, ν is the orbital frequency, and A is the cross-sectional area of the intersecting beams. The "total integrated luminosity", defined as the number of events produced per unit cross-section, is a function of the live-time fraction of the detector. The MarkII detector, running from the fall of 1979 through the spring of 1984, achieved a total integrated luminosity of $\sim 220 pb^{-1}$.

The MarkII detector has a cylindrical geometry with colliding beams along

the axis (see Figure 2.1). The major components of the detector include: two drift chambers (a high resolution drift chamber built for tracking close to the origin and a drift chamber for general tracking purposes); cylindrically arranged scintillator strips with photo-tubes for time-of-flight (TOF) measurements; a solenoidal magnet to aid in charged particle tracking; a lead-liquid argon calorimeter to detect electromagnetic energy; and a muon system consisting of layers of iron and proportional tubes. Each end of the cylindrical detector has an "endcap" (EC) calorimeter (with limited coverage) and a "small-angle-tagger" (SAT) system (which also serves as a luminosity monitor). These systems will be described in more detail in the following sections.

2.2 Vertex Chamber and Beam Pipe

In the summer of 1981, a high resolution drift chamber (called the "vertex chamber" (VC) since one of it's primary roles would be to aid in finding the vertices from decays of order $\tilde{>} 10^{-13}$sec) was installed in the MarkII. This device replaced a more primitive device consisting of a cylindrical band of scintillators ("pipe counter") and a low-resolution drift chamber with 4 layers ("trigger chamber"). Since most of the data collected by the MarkII at PEP, and all the data covered in this thesis, were taken with the vertex chamber, we will omit discussion of the pipe counter and trigger chamber.

The inside radius of the vertex chamber ($7.8cm$) is made of beryllium ($1.42mm$, or .6% of a radiation length X_0, thick) and serves as the beam pipe for the detector. The outside layer is at $\sim 40cm$ and the whole device has a length of $1.2m$. The chamber consists of 7 layers of drift cells (4 close to the inner radius and 3 close to the outer radius) in a common gas volume of 50% argon 50% ethane at $\sim 1atm$. Each cell consists of field-shaping wires (cathode at $\sim -2100V$) and sense wires at ground. (See Fig. 2.2 for a side view of the chamber and the cell

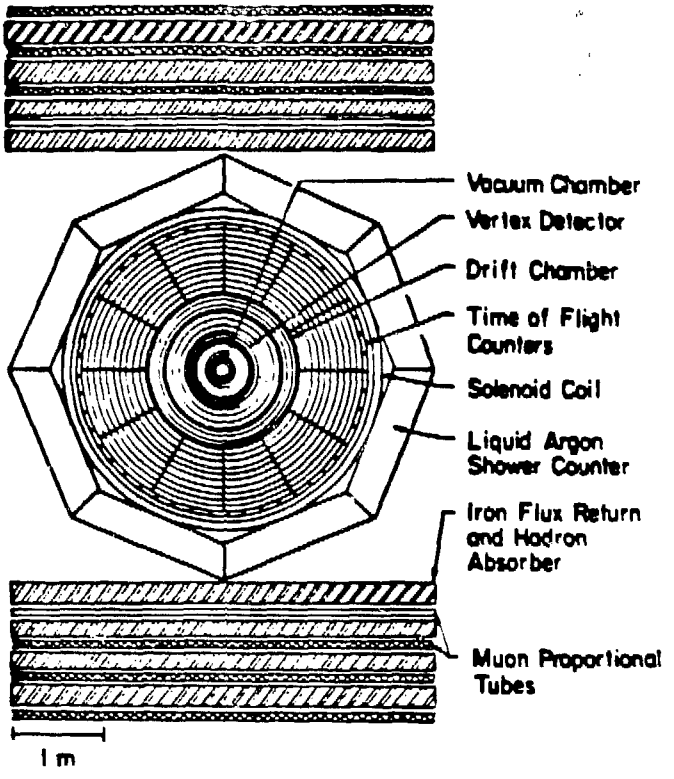

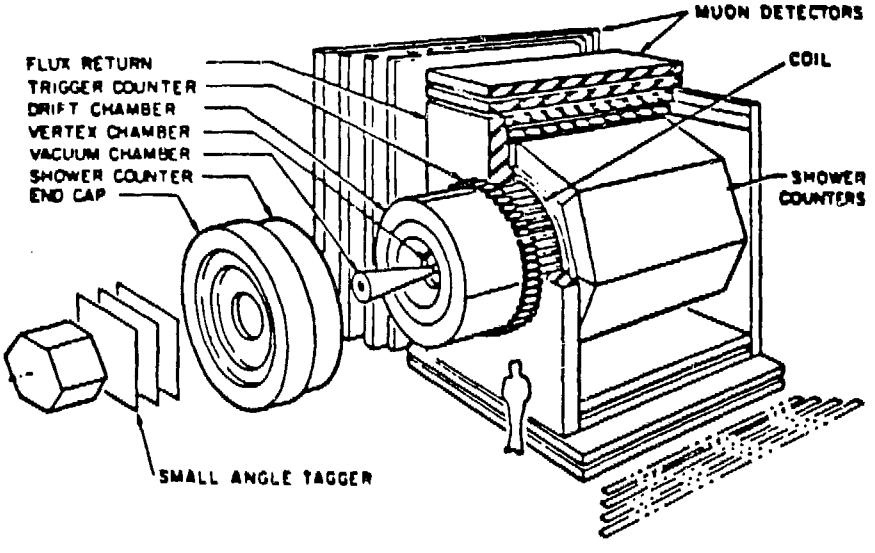

Figure 2.1. MarkII detector at PEP.

layout.) Table 2.1 lists the radius and number of sense wires in each layer. The single-hit resolution has been measured to be $\sim 110\mu$. The total extrapolation resolution, defined as the total error in extrapolating tracks back to the origin, is given by

$$\sigma^2_{miss} = \sigma^2_{mcs} + \sigma^2_{ex}$$
$$= (95\mu/p)^2 + (85\mu)^2$$

where p is the momentum in GeV/c, σ^2_{mcs} is the error from multiple Coulomb scattering, and σ^2_{ex} is the error in extrapolating the track back go the origin from the fit through the 7 layers[12].

2.3 Main Drift Chamber

The MarkII main drift chamber[13] (DC) provides charged particle tracking and charge identification over $\sim 85\%$ of the solid angle. The cylindrical chamber is immersed in a $2.32 kgauss$ magnetic field with a common gas volume of 50% argon and 50% ethane. The 16 layers (with the inner layer at a radial distance of $41cm$ and the outer at $145cm$) operate at voltages of between $-2950V$ and $-3500V$. Six of the layers consist of sense wires parallel to the beam (or $\hat{z}$) direction with 10 layers at a $\pm 3^o$ pitch to measure the z-coordinate of the track. Single hit resolution has been measured to be $\sim 200\mu$. The momentum of charged tracks in the xy-plane is determined by this chamber, and has a resolution given by

$$\left(\frac{\delta p_\perp}{p_\perp}\right)^2 = (0.025)^2 + (0.011 p_\perp)^2$$

with $p_\perp$ in GeV/c. The first term is the contribution from multiple scattering (the DC and VC are separated by a layer of polycarbonate plastic (LEXAN) with a thickness of $3.2mm$, or 1.0% of a radiation length (X_0) and $1.8mm$, or $\sim 2.0\% X_0$ of aluminum). The second term comes from the error in performing a χ^2 fit of a set of points to a circle. As the momentum increases, the curvature decreases and the uncertainty in the sagitta increases.

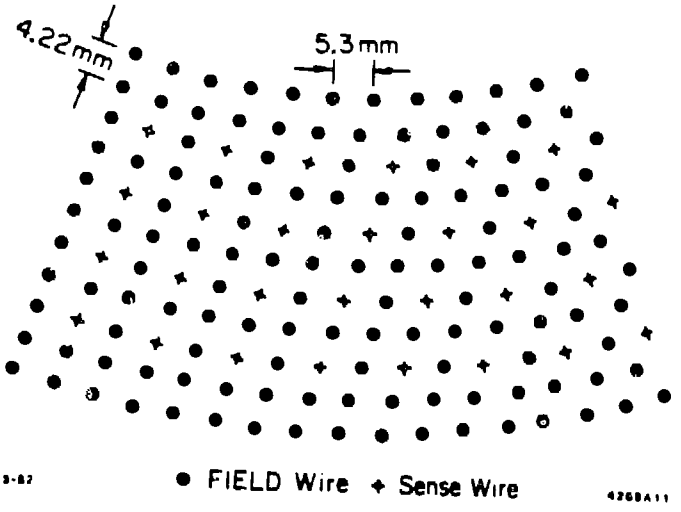

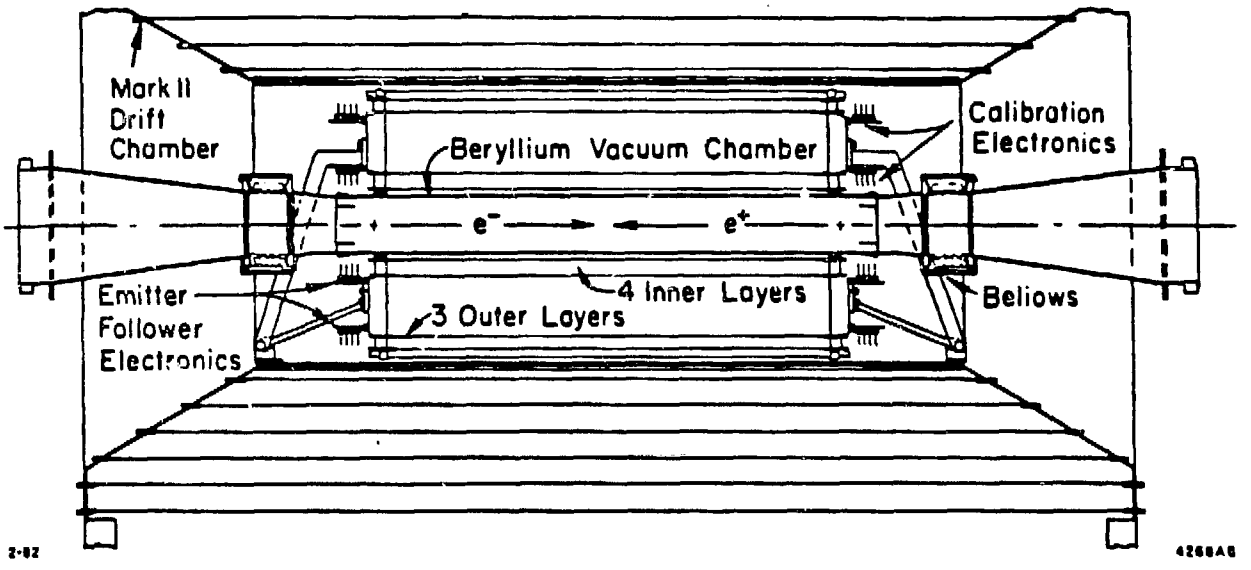

Figure 2.2. MarkII vertex chamber (side view) and cell layout.

Table 2.1. VC layer radius and number of wires.

Layer	Radius (cm)	Number of wires
1	10.1223	60
2	10.3658	65
3	11.8093	70
4	12.6528	75
5	30.3668	180
6	31.2103	185
7	32.0538	190

2.4 Time of Flight System

Outside of the DC at a constant radius of $1.51m$ are 48 plastic scintillator strips (Pilot F) each $3.4m$ long and parallel to the beam direction. A photo-tube at each end of the each strip provides information on timing and pulse height (the pulse height is used for a slewing correction to the timing information). The TOF system is also used in the primary and secondary trigger (see below) and in cosmic ray rejection. Calibration is through fiber optics attached to the center of each strip, coupled to a N_2 laser. Overall timing resolution (using Bhabha events) is measured to be $\sim 350ps$ at PEP. TOF and momentum information can be used for particle identification, but only at low momentum (p,K, and π separation up to $\sim 1\,\mathrm{GeV}/c$). In this thesis, proton identification using TOF was not attempted for this reason.

2.5 Magnetic Coil

At a radius of $1.6m$ is an electromagnetic solenoid providing a designed $4.64kgauss$ magnetic field. The solenoid consists of 2 layers of water cooled aluminum coils. A short between the coils in the winter of 1981-82 forced the elimination of the current in the inner coil, bringing the magnetic field down to

$2.32 kgauss$. All of the data reported on in this thesis is for this configuration.

The field was mapped by a Hall probe before the coil was installed at PEP, is monitored by NMR probes and is known to $\sim 1\%$ in the tracking volume. The coil has a thickness of 1.4 radiation lengths. Flux return is via 2 steel doors which close over the ends of the coil and are connected by steel slabs running over the top and bottom of the detector.

2.6 Liquid Argon Calorimeter

Eight lead-liquid argon (LA) calorimeter modules, octagonally arranged around the magnetic coil, covering $\sim 69\%$ of the solid angle, provide information on the electromagnetic energy in each event. Each module is $3.8m$ in length, $1.8m$ wide, and $30cm$ deep and is made up of 18 layers. Each layer is a "sandwich" consisting of a lead plane at ground ($2mm$ thick), a liquid argon gap ($3mm$ thick), a lead readout plane at $3500V$ ($2mm$ thick), and another liquid argon gap ($3mm$ thick). The total thickness of each module is about 14.5 radiation lengths at normal incidence. About 20% of the energy deposited in the module is deposited in the liquid argon gap. The energy resolution of the module has been measured to be

$$\frac{\sigma(E)}{E} \sim \frac{14\%}{\sqrt{E}}$$

with E in GeV. Each of the 18 readout layers are segmented into strips: 9 layers have 40 strips ($3.49cm$ thick) running parallel to $\hat{z}$ (F strips), 6 layers of 100 strips ($3.49cm$ thick) perpendicular to $\hat{z}$ (T strips), and 3 layers of 66 strips ($4.94cm$ thick) at 45° (U strips) providing spatial information. Between each strip is a $3mm$ gap. To reduce the number of readout channels needed, a ganging scheme is employed to reduce the number of channels to 3 F channels, 2 T channels, and 1 U channel. (see Fig. 2.3). In addition, at the front of each module are 3 aluminum planes separated by $8mm$ liquid argon gaps with the middle plane

longitudinally segmented into 3.8cm wide strips. This "trigger gap" is used to sample showers originating in the magnetic coil.

2.7 Muon System

The MarkII muon system consists of four walls located above, below, and on each side of the detector. Each wall consists of 4 layers each of alternating iron hadron absorber and extruded aluminum proportional tubes. The tubes in the inner layer run perpendicular to the beam direction providing information on the polar angle θ. All other tubes run along the beam direction. (See Fig. 2.4 for a cross-sectional view of the proportional tube layer.) The outermost layer covers $\sim$ 45% of the total solid angle. The total thickness of the LA calorimeter and muon system combined is 7.4 interaction lengths, which means a muon must have a momentum of about 2.0 GeV /c in order to traverse to the last layer.

2.8 Endcap Calorimeter

At each end of the detector, covering polar angles of $15^\circ \leq \theta \leq 40^\circ$ are the endcap (EC) calorimeters. Each endcap consists of 2.3 radiation lengths of lead followed by 2 layers of proportional chambers with an energy resolution given by

$$\frac{\sigma(E)}{E} \sim \frac{50\%}{\sqrt{E}}$$

with E in GeV. The EC provides trigger information and limited tagging of small angle events.

2.9 Small Angle Tagging System

Covering the polar angles of $21mr \leq \theta \leq 82mr$ at each end of the detector and behind the endcaps is the MarkII small angle tagging (or SAT) system. Each SAT consists of 3 layers of planar drift chambers with a spatial resolution of $\sim 300\mu$ followed by 3 layers of acceptance defining scintillator and a shower

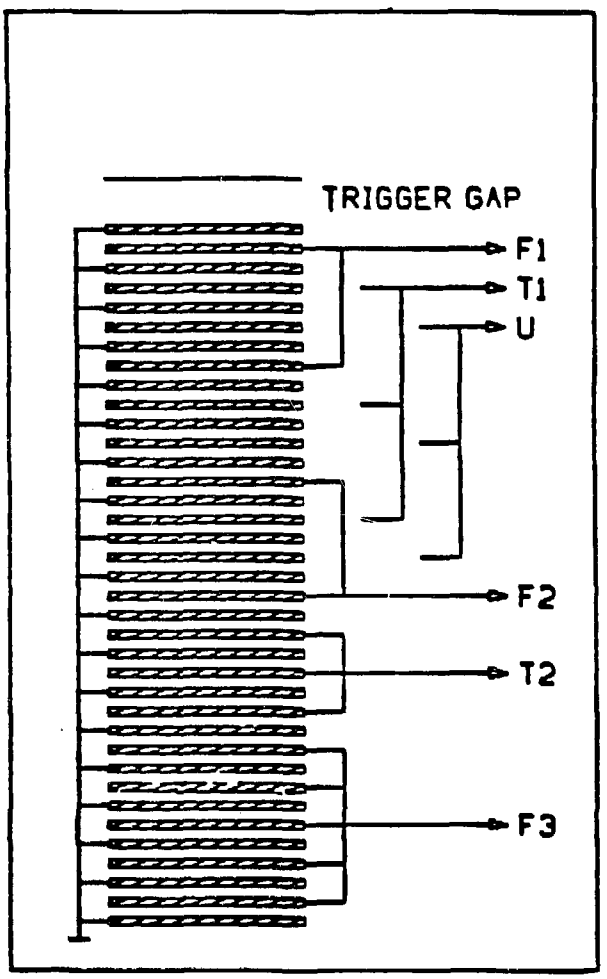

Figure 2.3. Liquid argon calorimeter ganging scheme. Particles enter through the trigger gap.

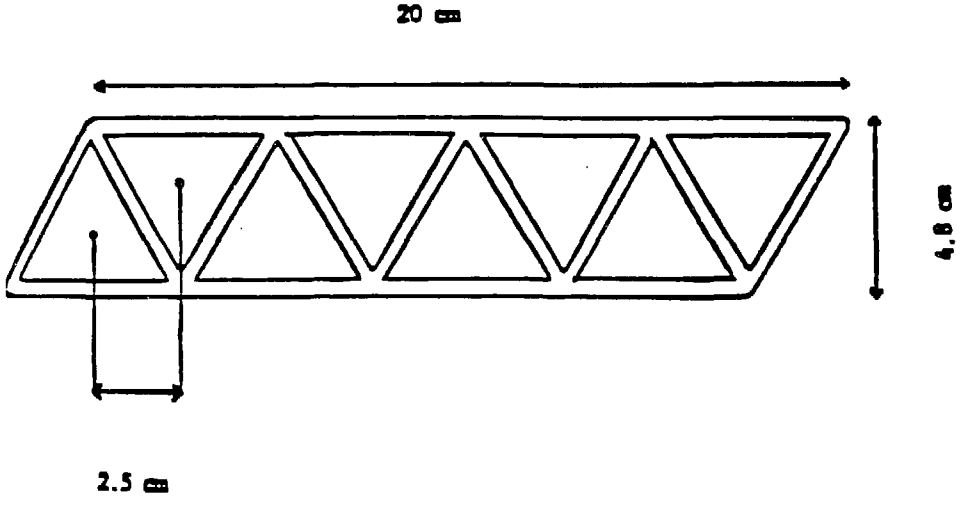

Figure 2.4. Cross-sectional view of muon proportional tube layer.

counter. The shower counter consists of 18 layers of $1/4in$ thick lead and $1/2in$ thick plastic scintillator with an energy resolution given by

$$\frac{\sigma(E)}{E} \sim \frac{16\%}{\sqrt{E}}$$

with E in measured in GeV. The system was designed to tag small momentum transfer 2-photon events as well as the low angle Bhabha events which determine the luminosity to ±5%.

2.10 Trigger System

The MarkII trigger is a two-level system designed for the $\sim 2.4\mu sec$ beam crossing period at PEP. The primary trigger determination, completed in $\sim 1\mu sec$, requires a beam crossing (BX) signal from PEP in coincidence with one of the following:

- *Charged Trigger:* typically at least 2 out of 4 (2/4) inner VC layers AND 1/3 outer VC layers AND 2/4 inner DC layers AND 1/3 mid-inner DC layers AND 1/3 mid-outer DC layers AND 2/4 outer DC layers AND 1 TOF signal.
- *Neutral Trigger:* typically at least 2 LA modules with energy $\tilde{>}$ 1GeV deposited in the front half OR at least $\tilde{>}$ 4GeV deposited in the EC OR at least 4GeV deposited in the front half of all eight LA modules together and in both endcaps summed together.
- *Bhabha Trigger:* a collinear electron-positron candidate in the SAT system.

Primary trigger rates are $\sim 1kHz$. If the event passes the primary trigger requirement, a microprocessor-controlled secondary trigger requirement[14,15] would be (typically) satisfaction of at least one of the following:

- at least 2 tracks found by a hardware track processor[14] where each track had a momentum of $\tilde{>}$ $100 - 200MeV/c$ (depending on running conditions) and is within the central $\sim 65\%$ of the detector

- a neutral energy trigger which is the same one employed by the primary trigger
- small angle bhabha event (where only 1 of every 16 were kept to keep the event logging rate down to acceptable levels).

The secondary trigger determination takes up to $30\mu sec$ resulting in a dead time of $\sim 3\%$ per kHz of primary rate, or $\sim 3\%$ with a primary rate of $\sim 1kHz$. Typical secondary trigger rates at PEP were $1-2Hz$, rarely exceeding $4Hz$.

2.11 Data Sets

The MarkII, running in the half-field ($2.32kgauss$) configuration with the vertex chamber, collected about 208pb of data. During this period, many of the detector systems experienced problems degrading the resolution and efficiency of the detector. Such problems were dealt with as soon as was feasible, however the data retains some degree of non-uniformity as a result. Since this thesis uses the VC and DC systems most heavily, we will be concerned more with the degradation in those systems.

In 1983, the DC system experienced problems with "glow" and began to draw unacceptably high currents. This necessitated lowering the operating voltages for a time by about $500V$. This caused a drop in tracking efficiency for the affected data sets. In the spring of 1983, oxygen was added (in the ratio of 0.7%) to the 50-50 argon-ethane mixture and voltages were raised close to the nominal level. In the fall of 1983 through the spring of 1984, the voltages were raised back to the normal level.

This drop in efficiency, determined to be independent of momentum, was measured by P.C. Rowson[16] by unfolding the multiplicity distribution in hadronic events (using the Monte Carlo simulation) and normalizing the different data sets to the data collected before the problem surfaced. Table 2.2 is from this

study where the errors in the correction factors are $\sim \pm 5\%$. These numbers reflect the drop in the single-track efficiency. The drop in efficiency for the analysis concerning this thesis is more complicated, and is dealt with in later sections. However, since the POOR and SPRING data sets were found to have a particularly low yield of $\Lambda/\bar{\Lambda}$ per unit cross-section (and therefore a lower detection efficiency), and since together they comprise only $\sim$ 13% of the total data, they will be left out of the analysis that follows.

Table 2.2. DC efficiency normalized to VCSUM[16].

Data Set	Luminosity (pb^{-1})	% of Total	Correction	Remarks
VCSUM	19.2	9.2	1.0	Pre-glow
POOR	15.5	7.5	0.8960	DC glow
SPRING	11.4	5.5	0.9075	same
SPRING2	57.9	27.8	0.9355	Inner volts up slightly
OXYGEN	24.2	11.6	0.9965	O_2 added - close to normal volts
NEWDAT	79.8	38.4	1.0000	All volts normal

3. The Data

3.1 Hadronic Events

In order to find $\Lambda/\bar{\Lambda}$ events in the data (I will refer to $\Lambda/\bar{\Lambda}$ as meaning both Λs and $\bar{\Lambda}$s unless otherwise stated), one must first apply a set of hadronic event cuts to all events. The particular choice of cuts is optimized to reduce backgrounds from: beam-gas interactions (interactions between the e^+/e^- beam with residual atoms in the beam pipe); 2-γ events (see Figure 3.1 (a)); lepton pair events (see Figure 3.1(b)); and τ pair events (see Figure 1.1(c)). The balance searched for is one between maximizing statistics without compromising purity. Also, one has to keep in mind that the Monte Carlo simulation, a good but imperfect one, will not be able to duplicate entire distributions exactly, and so we tailor cuts so as to cut out parts of distributions relevant to this analysis not reliably simulated (these are usually the non-gaussian tails and etc.).

Keeping all this in mind, the following cuts are chosen:

- require ≥ 5 good charged tracks, where a "good" track is one with momentum $p > 100MeV/c$ and whose distance of closest approach (DCA) to the interaction point (IP) is: $< 4cm$ in the xy-plane and $< 8cm$ in z. The rms beam size is $\sigma_x \sim 450\mu, \sigma_y \sim 80\mu$, and $\sigma_z \sim 1.5cm$. Also, electrons and positrons from γ-conversions are not included as a "good" hadronic track.
- require "good" neutral track as one with $E > 200MeV$ in the calorimeter with no charged track extrapolated into the calorimeter closer than 7cm, and have less than 50% of its energy shared by any other neutral track
- require total visible energy $E_{vis} > .25E_{cm}$ where $E_{vis} = \sum E_{ch} + \sum E_{neu}$ and $E_{ch}(E_{neu})$ is the energy of "good" charged (neutral) tracks as defined above. This cut is most effective in eliminating the 2-γ events.
- require the reconstructed primary vertex to be within 4cm of the IP in the xy-plane and 7cm of the IP in z

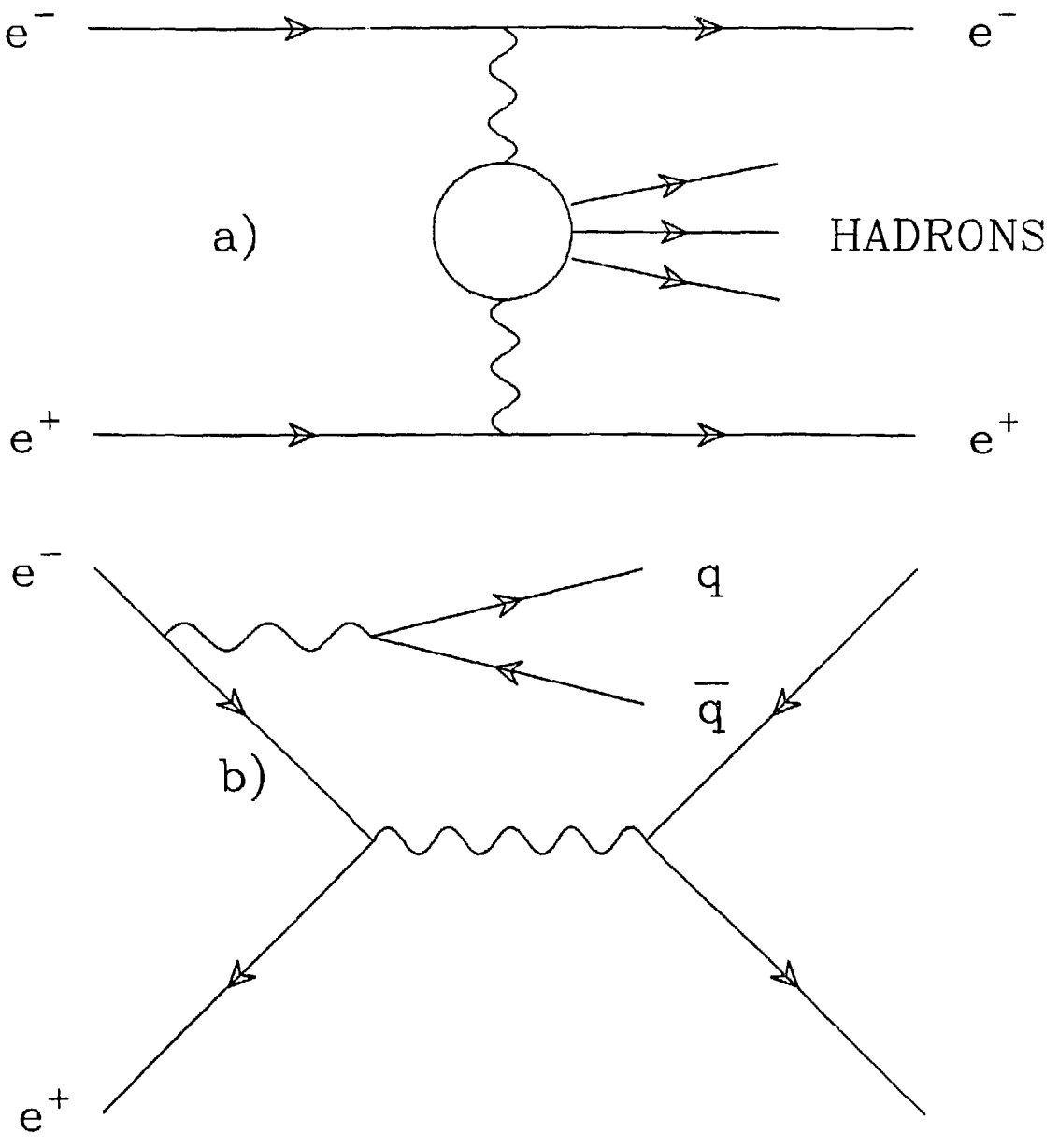

Figure 3.1. Sources of hadronic background from a) $2-\gamma$ events [this is not to be confused with the process $e^+e^- \rightarrow \gamma\gamma$ (see Figure 1.1(b))] and b) lepton-pair events.

- construct the sphericity axis[17]from the "good" charged tracks and require that $\mid cos\Theta_{sphericity} \mid < 0.7$. This cut is referred to as the fiducial volume cut, as it eliminates events where the jet axis points into a region of the detector with small acceptance.

The backgrounds for hadronic events using cuts very similar to these was measured in detail by J. Patrick [18, 19]. From that work and other considerations [7], we estimate the backgrounds to be 1.5±1.0% for beam-gas and 2γ events and 2.0±1.0% for τ-pair events. The lepton-pair contamination is estimated from kinematic considerations to be negligible.

In order to measure the efficiency for these cuts, we use both the Feynman-Field (FF, referred to as BQCD) and the LUND string Monte Carlos (see sections 1.4 through 1.6). Since the efficiency is a detector-related quantity (as opposed to a physics-related quantity), the two should agree. We find that $\epsilon_H = .593$ from BQCD and .588 from LUND, and so determine the systematic error to be $\sim 1\%$. In this thesis, we use the BQCD Monte Carlo to calculate efficiencies. Using the value $\epsilon_H = .593$ and the luminosity as determined from bhabha events, we can measure the quantity $R = \sigma(e^+e^- \rightarrow q\bar{q})/\sigma(e^+e^- \rightarrow \mu^+\mu^-)$. We find $R = 3.94\pm \sim 4\%$ (±4% is a conservative estimate due to uncertainty in luminosity [19]), well in agreement with the world average of ~ 4 at 29GeV [20] .

3.2 $\Lambda/\bar{\Lambda}$ Selection

In searching for $\Lambda \rightarrow p\pi^-$ and $\bar{\Lambda} \rightarrow \bar{p}\pi^+$ decays, one would like to be able to identify the proton. Using the TOF, however, one is only sensitive to the low momentum protons, since at sufficiently high momentum all final state charged tracks (p, K, π, μ, e) travel at $\beta \sim c$ and thus take the same time in reaching the TOF system. Table 3.1 shows the TOF for a 2GeV particle traversing a distance $d \sim 1.5m$. Since the resolution of the MarkII TOF system is $350-375ps$ (see section

2.4 on TOF above), one can not do $p-K$ separation or $p-\pi$ separation to better than 2σ. We thus abandon proton identification in finding $\Lambda/\bar{\Lambda}$ and rely more heavily on the kinematics of the decay $\Lambda \rightarrow p\pi^-$ (and $\bar{\Lambda} \rightarrow \bar{p}\pi^+$) and the long lifetime of the decay in finding these particles.

Table 3.1. TOF for different particles with $p = 2\,\mathrm{GeV}/c$

particle	TOF for $p = 2\,\mathrm{GeV}/c$
p	5.5*ns*
K	5.2*ns*
π	5.0*ns*
μ	5.0*ns*
e	5.0*ns*

Due to the comparable mass and lifetime of the Λ and K_s (see Table 3.2) and since this lifetime is so much greater than that of the majority of the produced hadrons which decay within the detector fiducial volume, we would expect that any algorithm which in order to find $\Lambda \rightarrow p\pi^-$ and $\bar{\Lambda} \rightarrow \bar{p}\pi^+$ decays simply takes invariant mass combinations of pairs of oppositely charged tracks with well displaced decay vertices will find many $K_s \rightarrow \pi^+\pi^-$ decays as well. We therefore search for $\Lambda \rightarrow p\pi^-$, $\bar{\Lambda} \rightarrow \bar{p}\pi^+$, and $K_s \rightarrow \pi^+\pi^-$ simultaneously and employ some criteria to resolve any ambiguities.

Table 3.2. Mass and lifetime for $\Lambda/\bar{\Lambda}$ and K_s

	M (GeV/c^2)	ct (cm)
Λ	1.1156	7.89
K_s	.4977	2.68

3.2.1 Vee Finding

To find $\Lambda \to p\pi^-$ and $\bar{\Lambda} \to \bar{p}\pi^+$ decays, we employ a vee finding algorithm which searches for the decay of a neutral particle into two charged particles[21]. First, we remove poorly measured tracks by requiring all charged tracks in the hadronic event (except e^+e^- from γ conversions) be subjected to a cut on the distance of closest approach (DCA) to the interaction point (IP) in the xy-plane and in z. Table 3.3) lists the values used. Note Λ and K_s decay products will in general not point back to the IP. Cuts are purposely looser for the $\Lambda \to p\pi^-$ hypothesis in order to eliminate the obvious $K_s \to \pi^+\pi^-$ candidates with minimum bias against the $\Lambda \to p\pi^-$ candidates. If both tracks pass the track cuts, we find the two points of intersection of the pair (the intersection of the two circles) in the xy-plane, If both choices for the intersection point are within the detector fiducial volume, we choose the one which has the smallest difference in z of the two charged tracks ($\Delta z \equiv \mid z^+ - z^- \mid$). Using the momentum of the two tracks at the selected intersection, we calculate and cut on the following quantities:

Table 3.3. Cuts on single tracks used in $\Lambda \to p\pi^-$ search.

	$\Lambda \to p\pi^-$	$K_s \to \pi^+\pi^-$
DCA(xy)	$> .1mm$	$> 1mm$
DCA(z)	$< 15cm$	$< 10cm$

- DCA of the reconstructed candidate in the xy-plane (using the vector sum of the two momenta) to be $< 5mm$ for the K_s hypothesis and $< 5cm$ for the Λ hypothesis.
- $ct > 1mm$ for the K_s and $> 4mm$ for the Λ hypothesis where ct is measured in the rest frame of the decaying $\Lambda/\bar{\Lambda}$
- $\Delta z < 5cm$ for the K_s and Λ hypothesis (Δz as defined above)

See Table 3.4 for a summary of these cuts. We retained Λ and $\bar{\Lambda}$ "candidates" with mass between 1.0 and 1.2 GeV $/c^2$ and K_s "candidates" with mass between .375 and .625 GeV $/c^2$. These regions contain both signal and background. This enabled us to have a large sample of events for the background subtraction.

Table 3.4. Cuts on the reconstructed V^0.

	$\Lambda \rightarrow p\pi^-$	$K_s \rightarrow \pi^+\pi^-$
DCA(xy)	$< 5cm$	$< 5mm$
Δz	$< 5cm$	$< 5cm$
$c\tau$	$> 4mm$	$> 1mm$

Candidates passing the above cuts are then subjected to the following:

- momentum correction of the secondaries due to energy losses accrued passing thru the detector,
- multiple coulomb scattering corrections added to the error matrix for each track,
- a vertex-constrained fit in 3 dimensions, with a χ^2 of the fit required to be < 10 for 3 degrees of freedom. The invariant mass is then recalculated using the momentum of the secondaries at the new vertex position (this changes the previous calculation by $\sim 3MeV$ on average).

If the candidate vee passes both the $\Lambda \rightarrow p\pi^-$ (or $\bar{\Lambda} \rightarrow \bar{p}\pi^+$) and the $K_s \rightarrow \pi^+\pi^-$ hypotheses, the ambiguity is resolved based on the absolute value of the difference between the calculated mass and the known mass for the hypothesis. Using the Monte Carlo calculations we have found that whenever the candidate was from a real Λ (or $\bar{\Lambda}$) decay (and thus the ambiguity was between Λ and K_s or $\bar{\Lambda}$ and K_s), the correct choice was picked 77% of the time. (Note that if the choice of proton and pion for the two tracks from the Λ decay are switched, the invariant

mass changes by such an amount as to be outside the above mentioned mass window. This ensures that ambiguities between Λ and $\bar{\Lambda}$ would never occur.)

An added problem is one of arbitrating between cases where two successful candidates share a track. Such arbitration is decided on the basis of the projection of the momentum of the reconstructed vee back to the IP. Choosing the vee with the smallest Θ_v (as defined in Figure 3.2) proved successful in 83% of the cases.

The $m(p\pi)$ distribution for all $\Lambda/\bar{\Lambda}$ candidates (plus background), using the NEWDAT data set (see Table 2.2), can be seen in Figure 3.3. The $m(\pi\pi)$ distribution for all K_s candidates can be seen in Figure 3.4. The large background in the $\Lambda/\bar{\Lambda}$ sample relative to the K_s sample is due partly to the fact that there is no proton identification, and partly to the fact that the cuts were looser for the $\Lambda/\bar{\Lambda}$ hypothesis (see Table 3.3 and Table 3.4 above). This was done deliberately to minimize the accidental misidentification of a $\Lambda/\bar{\Lambda}$ as a K_s. Figure 3.5 shows the $m(\pi\pi)$ distribution for the $\Lambda/\bar{\Lambda}$ candidates. The K_s contamination in this distribution is $11.6 \pm 2.2\%$ (statistical uncertainty) for $\Lambda/\bar{\Lambda}$ candidates and background with $1.106\,\mathrm{GeV}/c^2 \leq m(p\pi) < 1.126\,\mathrm{GeV}/c^2$.

3.2.2 Detector Resolution

It is important that the Monte Carlo simulation reproduce the resolution of the detector. To check that the simulation of the mass resolution of the $\Lambda/\bar{\Lambda}$ is accurate we look at the relatively pure K_s signal as a function of momentum (see Figure 3.6) in the Monte Carlo and compare with data. We use the K_s candidates since there are more of them than there are $\Lambda/\bar{\Lambda}$. Also, the efficiencies for the processes $\Lambda \rightarrow p\pi^-$ and $K_s \rightarrow \pi^+\pi^-$ are similar (both are $\sim$ 10%). The agreement between data and Monte Carlo is quite good. Figure 3.7 shows the comparison between data and Monte Carlo for the $\Lambda/\bar{\Lambda}$ candidates. The shape

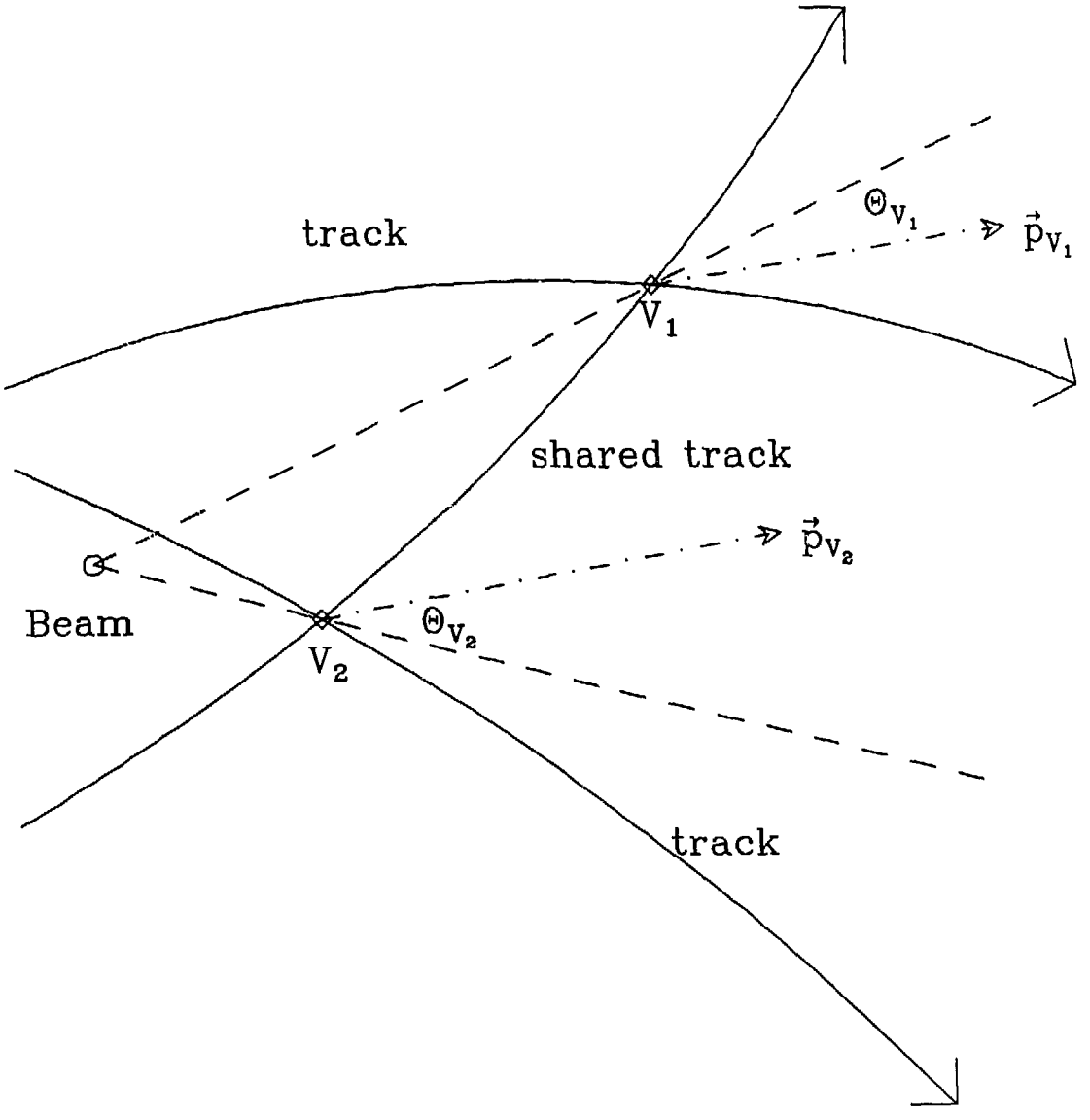

Figure 3.2. Arbitration decided as to smallest Θ_v

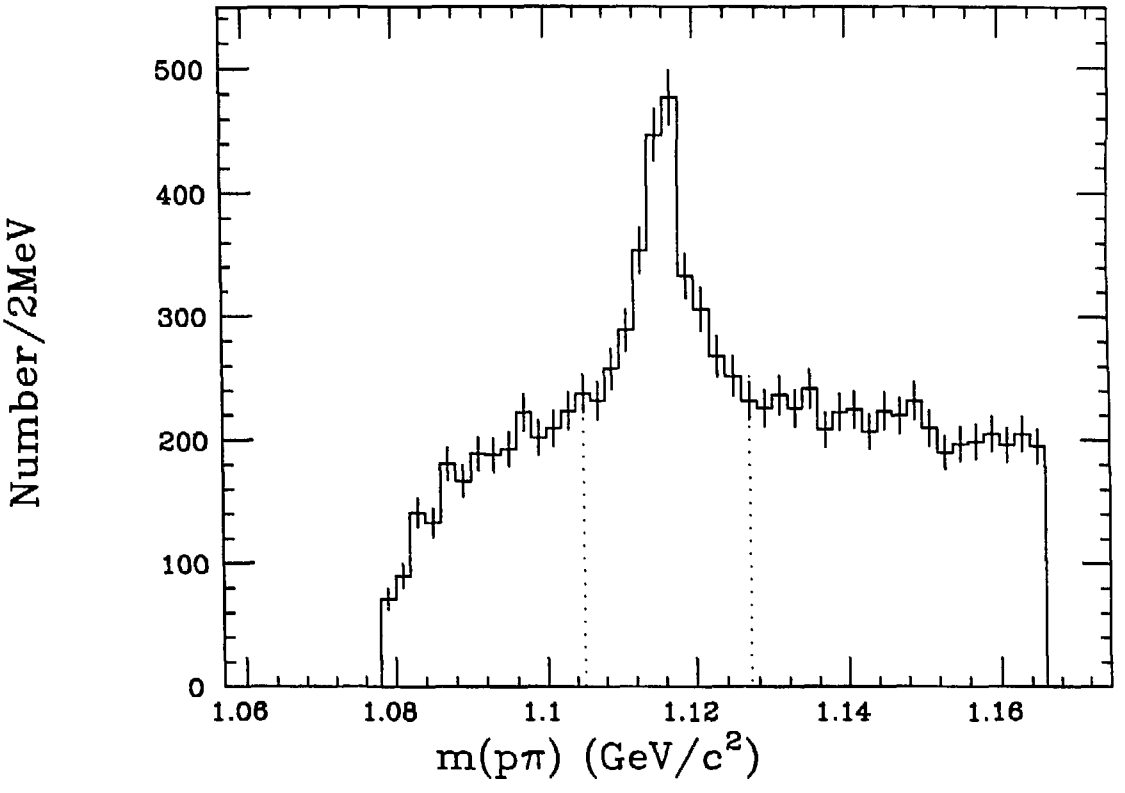

Figure 3.3. $m(p\pi)$ distribution for all $\Lambda/\bar{\Lambda}$ candidates and background. Total number of events within dotted lines ($1.106\text{GeV} \leq m(p\pi) < 1.126\text{GeV}$) is 3216. The background (using adjacent bins) is estimated to be 2274, leaving 942 events in the peak.

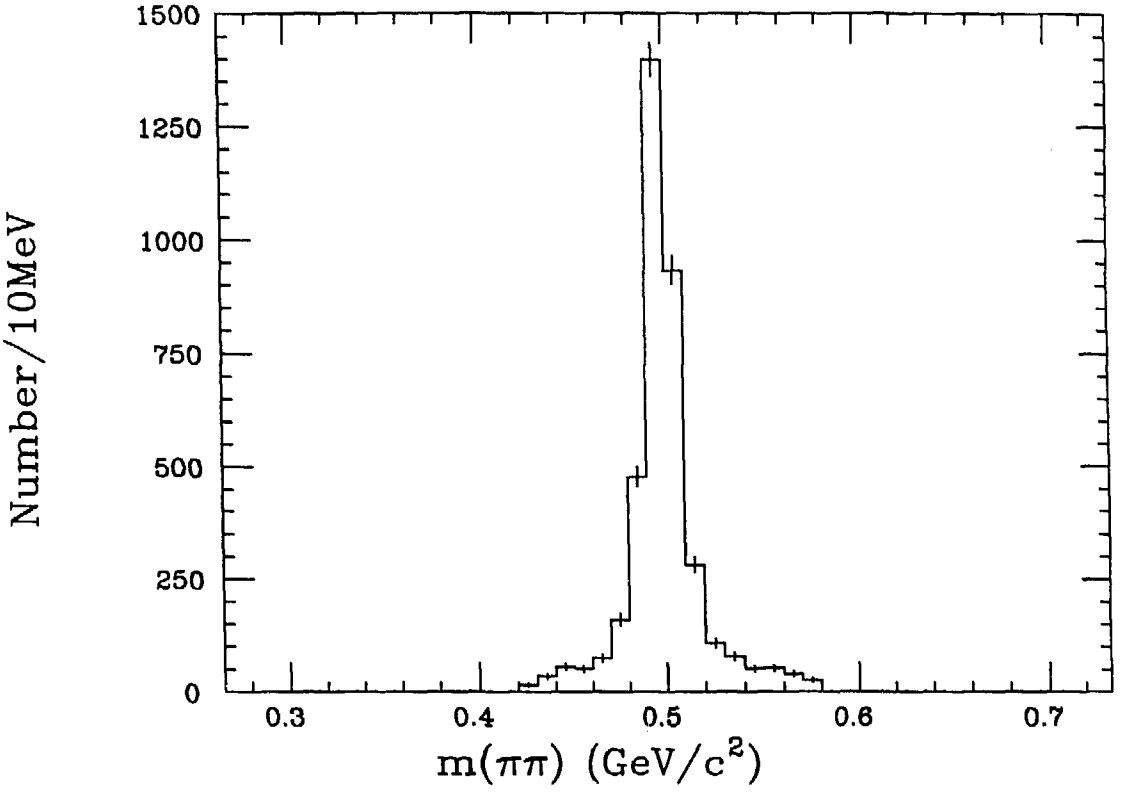

Figure 3.4. $m(\pi\pi)$ distribution all K_s candidates. Total number of points: 3831

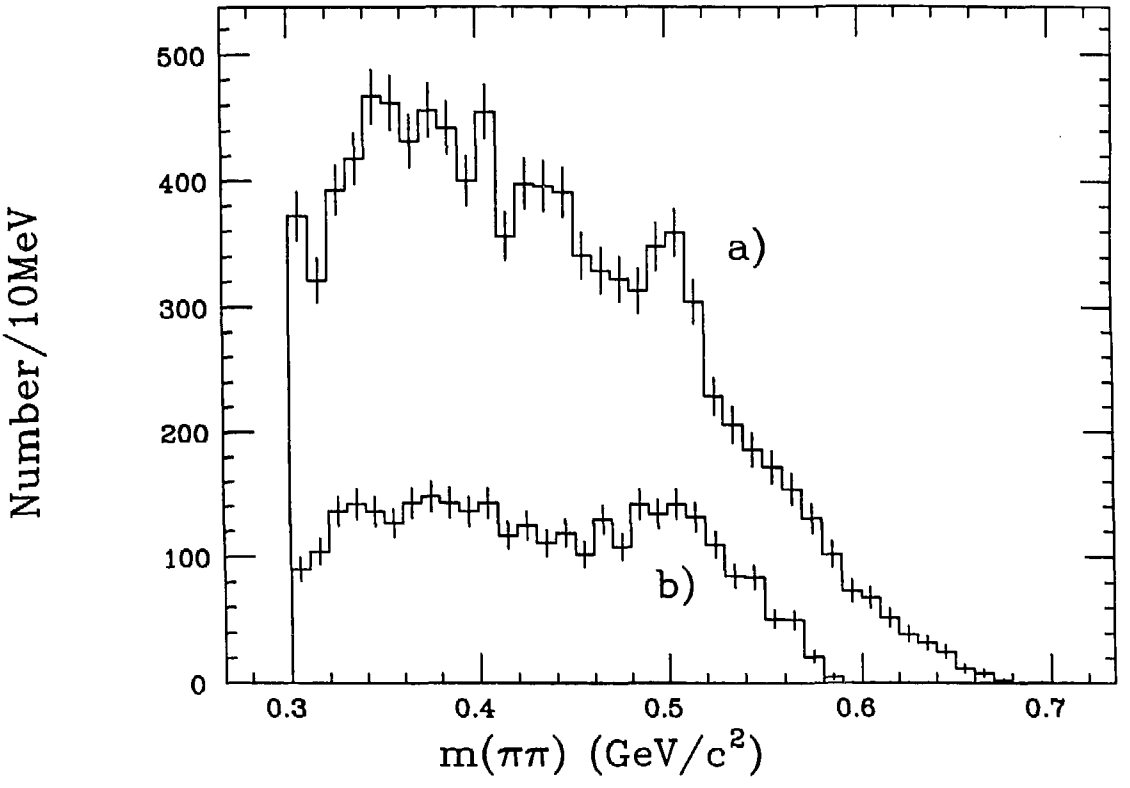

Figure 3.5. $m(\pi\pi)$ distribution for a) all $\Lambda/\bar{\Lambda}$ candidates (including background) and b) only $\Lambda/\bar{\Lambda}$ candidates with 1.106 GeV $/c^2 \leq m(p\pi) <$ 1.126 GeV $/c^2$ (3216 events in this region).

of the backgrounds agree well. The Monte Carlo BQCD (FF scheme) has an artificially high rate for producing $\Lambda/\bar{\Lambda}$ particles, and hence does not match in the peak region.

3.2.3 *Background Components*

Figure 3.8 shows the Monte Carlo simulation of the breakdown of components contributing to the $\Lambda/\bar{\Lambda}$ candidates. Note the peak in the K_s background. This is due to the fact that in order to resolve ambiguities between the $\Lambda/\bar{\Lambda}$ and K_s hypothesis we choose based on the smaller of $\mid m(p\pi) - 1.1156\,\mathrm{GeV}/c^2 \mid$ and $\mid m(\pi\pi) - 0.4977\,\mathrm{GeV}/c^2 \mid$. Thus, any real K_s's which have $\mid m(p\pi) - 1.1156\,\mathrm{GeV}/c^2 \mid < \mid m(\pi\pi) - 0.4977\,\mathrm{GeV}/c^2 \mid$ will become background for the $\Lambda/\bar{\Lambda}$'s. Since the distribution of the invariant mass (both $m(p\pi)$ and $m(\pi\pi)$) is a function of the resolution of the detector, such confusion is unavoidable.

3.2.4 *Efficiency*

To measure the efficiency for finding $\Lambda \to p\pi^-$ and the conjugate decay $\bar{\Lambda} \to \bar{p}\pi^+$, we use the Feynman-Field (FF) Monte Carlo (referred to as BQCD). This efficiency for finding $\Lambda/\bar{\Lambda}$ decays is measured to be $19.0 \pm .3\%$. This efficiency can be broken up into the product of the efficiency for finding a hadronic event (ϵ_H) times the acceptance for $\Lambda \to p\pi^-$ ($\epsilon_{Acc} = 64.0 \pm .4\%$) times the efficiency of the algorithm as just described ($\epsilon_{Detec} = 46.5 \pm .5\%$) to give $\epsilon_{Total} = \epsilon_H \epsilon_{Acc} \epsilon_{Detec}$. Solving for ϵ_H gives $\epsilon_H = 63.8 \pm 1.1\%$, the hadronic efficiency when a $\Lambda/\bar{\Lambda}$ was present. This value is higher than the total hadronic efficiency of $59.3 \pm .1\%$, and so we assign a systematic error of $\pm 4\%$ to the efficiency for $\Lambda \to p\pi^-$.

3.2.5 *Kinematics of $\Lambda/\bar{\Lambda}$-K_s Ambiguity*

A characteristic of the decay $\Lambda \to p\pi^-$ is the asymmetry in the difference in momentum between the p and π in the lab frame. The proton has most of the

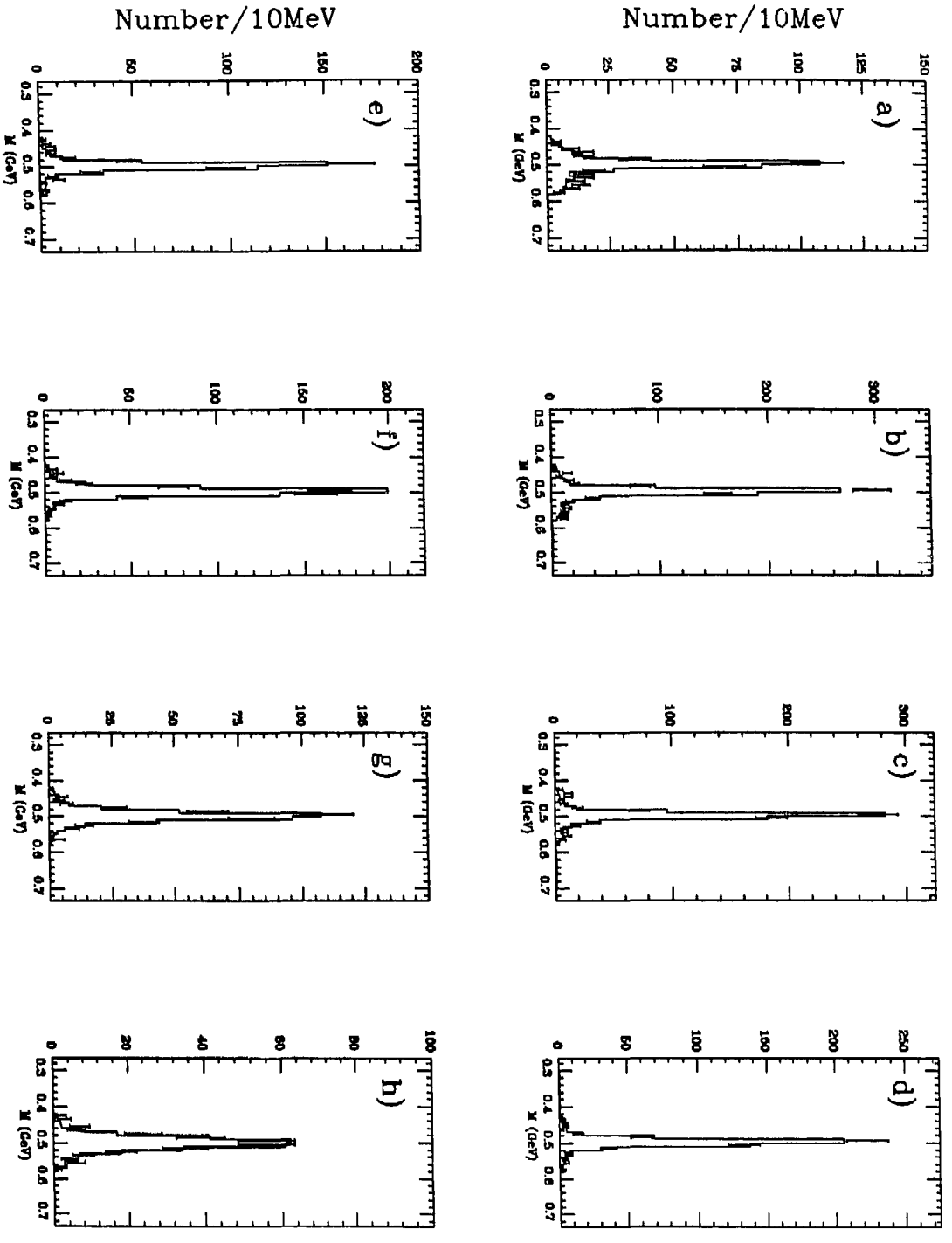

Figure 3.6. $m(\pi\pi)$ for K_s candidates for a) $p < .5$ GeV /c, b) $.5 \leq p < 1$ GeV /c, c) $1.5 \leq p < 1.5$ GeV /c, d) $1.5 \leq p < 2$ GeV /c, e) $2 \leq p < 2.5$ GeV /c, e) $2.5 \leq p < 3.5$ GeV /c, f) $3.5 \leq p < 5$ GeV /c, and f) $5 \leq p < 14.5$ GeV /c. Histogram is from Monte Carlo and points are from data.

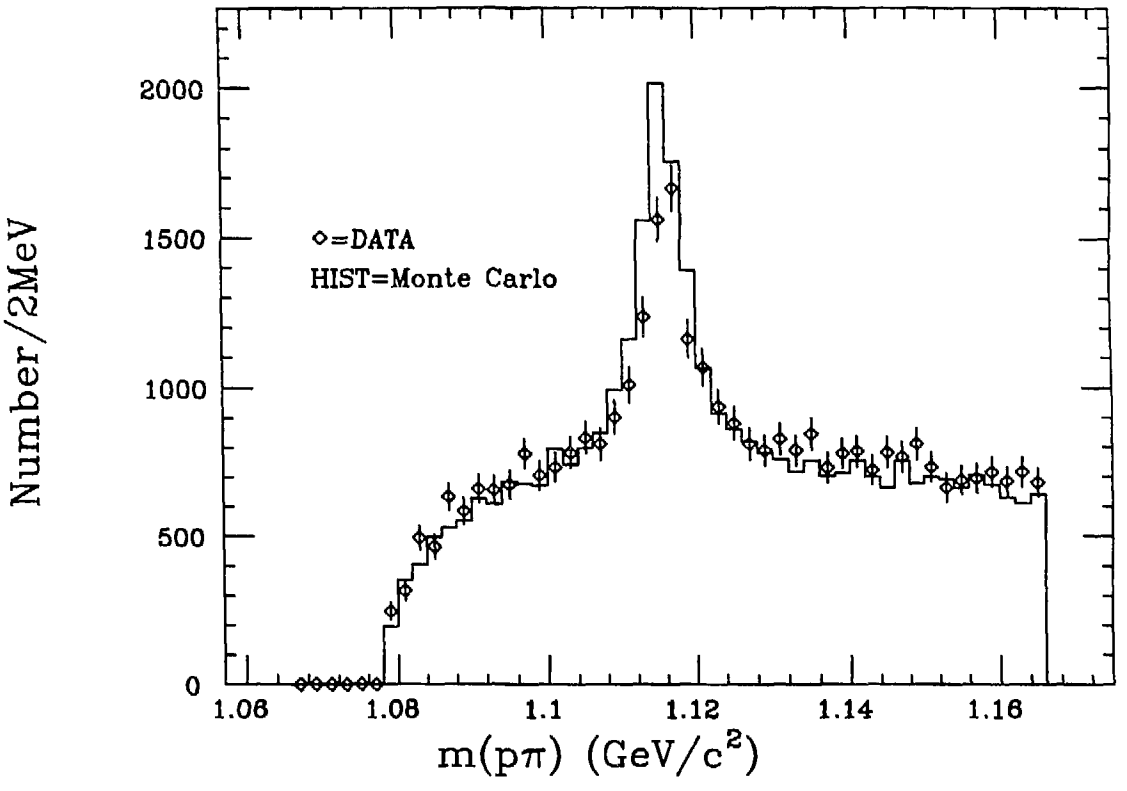

Figure 3.7. Comparison of $m(p\pi)$ distribution in data with BQCD Monte Carlo

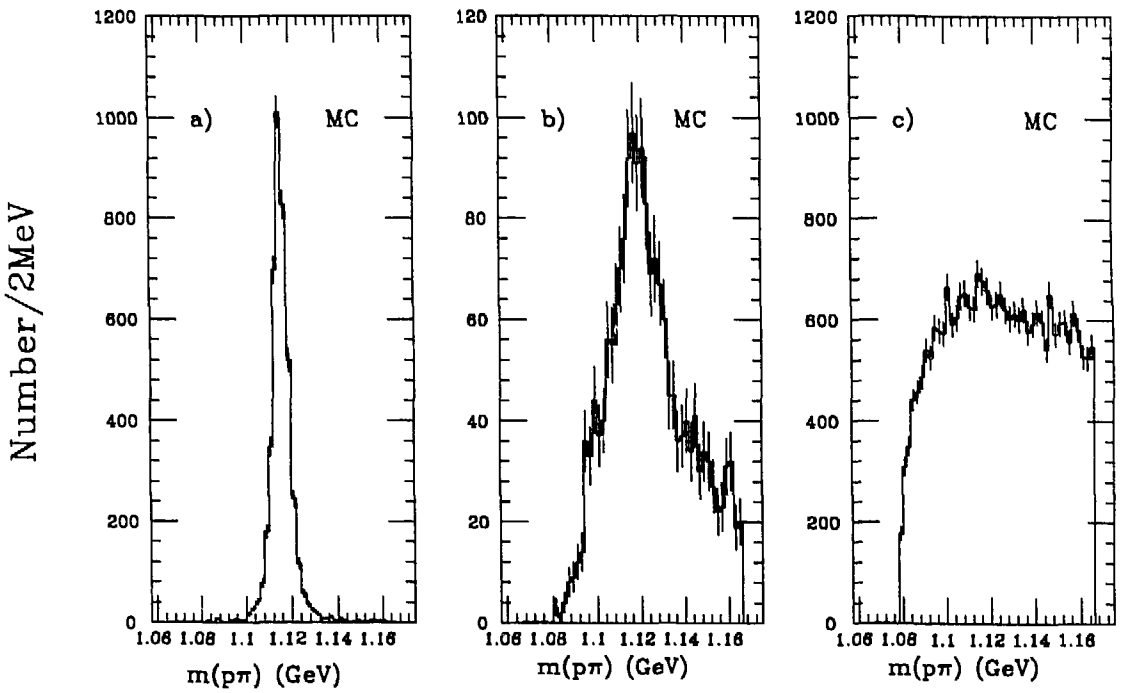

Figure 3.8. The three components in the $m(p\pi)$ spectrum for Monte Carlo data are a) real $\Lambda/\bar{\Lambda}$s, b) K_s contamination (note different scale), and c) combinatoric contamination.

momentum. This is due to the fact that the Λ momentum spectrum is peaked at $\sim 1-2\,\mathrm{GeV}/c$, and that for backwards decays (backwards in the c.m. of the Λ relative to the boost direction), the efficiency for detecting the decay is low (the momentum in the Λ c.m. of the p and π is about $100 Mev/c$). Any background due to $K_s \rightarrow \pi^+\pi^-$ decays comes from the forward-backward decaying K_s particles. To see this we form the quantity

$$\alpha \equiv \frac{p_{\parallel}^{+} - p_{\parallel}^{-}}{p_{\parallel}^{+} + p_{\parallel}^{-}}$$

where $p_{\parallel}^{\pm}$ refers to the momentum of the $\pm$ particle from the decay relative to the direction of the decaying particle, and plot vs $p_{\perp}$ (see Figure 3.9). Figure 3.10 shows what such a plot should look like for $\Lambda/\bar{\Lambda}$ and K_s decays where the boost momentum is taken to be $1.5\,\mathrm{GeV}/c$ and where three values for the mass of the $\Lambda/\bar{\Lambda}$ are given. Figure 3.11 shows the distribution for $\Lambda/\bar{\Lambda}$ candidates in the data, Figure 3.12 shows the K_s candidates, and Figure 3.13 shows both. One can see that given the presence of both $\Lambda/\bar{\Lambda}$ and K_s without p-π separation there is no kinematic variable that can be used to distinguish between the forward-backward K_s and real $\Lambda/\bar{\Lambda}$.

3.2.6 Further Reduction of the Background

We can now further reduce the combinatoric background by requiring

- $\Delta z < 3cm$, and
- the distance of closest approach of the reconstructed candidate in the xy-plane be less than $5mm$, and
- the distance of closest approach of the proton and pion in the xy-plane be greater than $1mm$, and
- the distance from the interaction point to the decay vertex in the xy-plane be greater than $1cm$, and

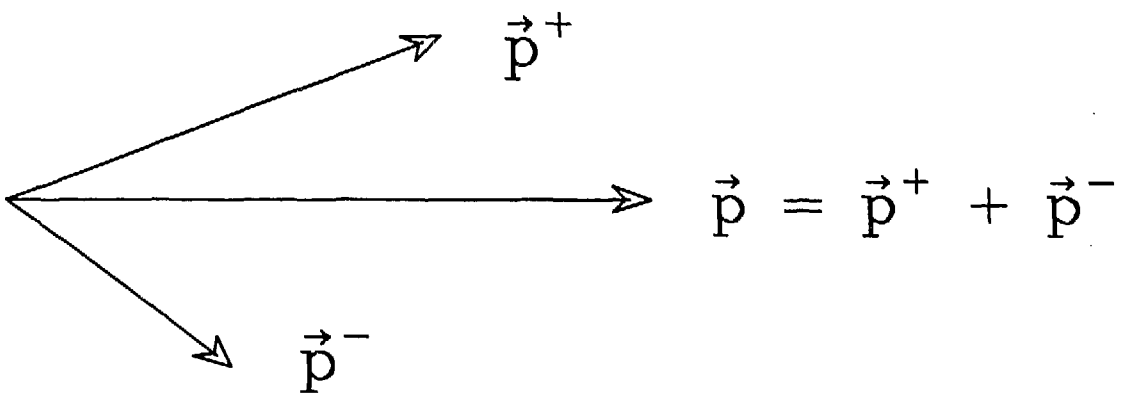

Figure 3.9. Kinematics of V^0 decays.

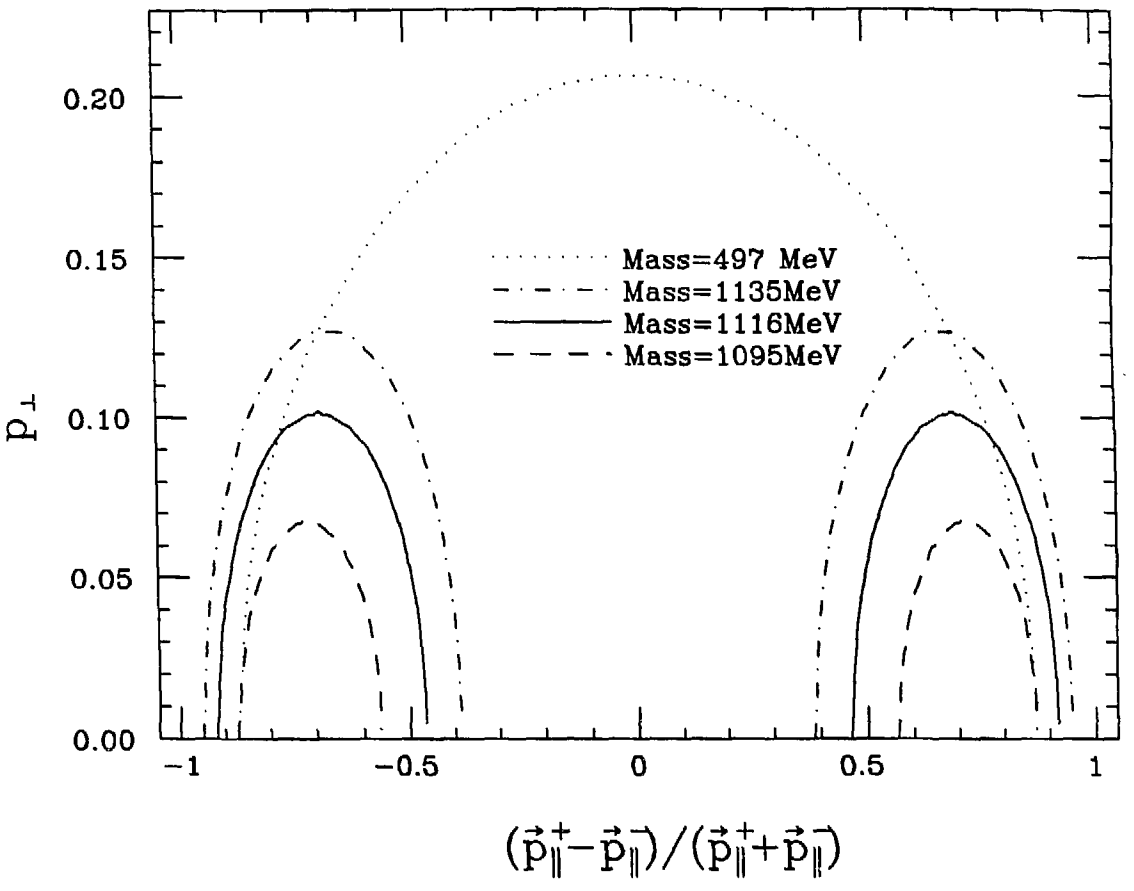

Figure 3.10. Dotted line is for decay $K_s \rightarrow \pi^+\pi^-$ with $m_{K_s} = 497\ MeV/c^2$. Dotdashed line is for decay $\Lambda \rightarrow p\pi^-$ with $m_\Lambda = 1135\ MeV/c^2$, solid line is decay with $m_\Lambda = 1116\ MeV/c^2$, and dotdashed line is decay with $m_\Lambda = 1095\ MeV/c^2$

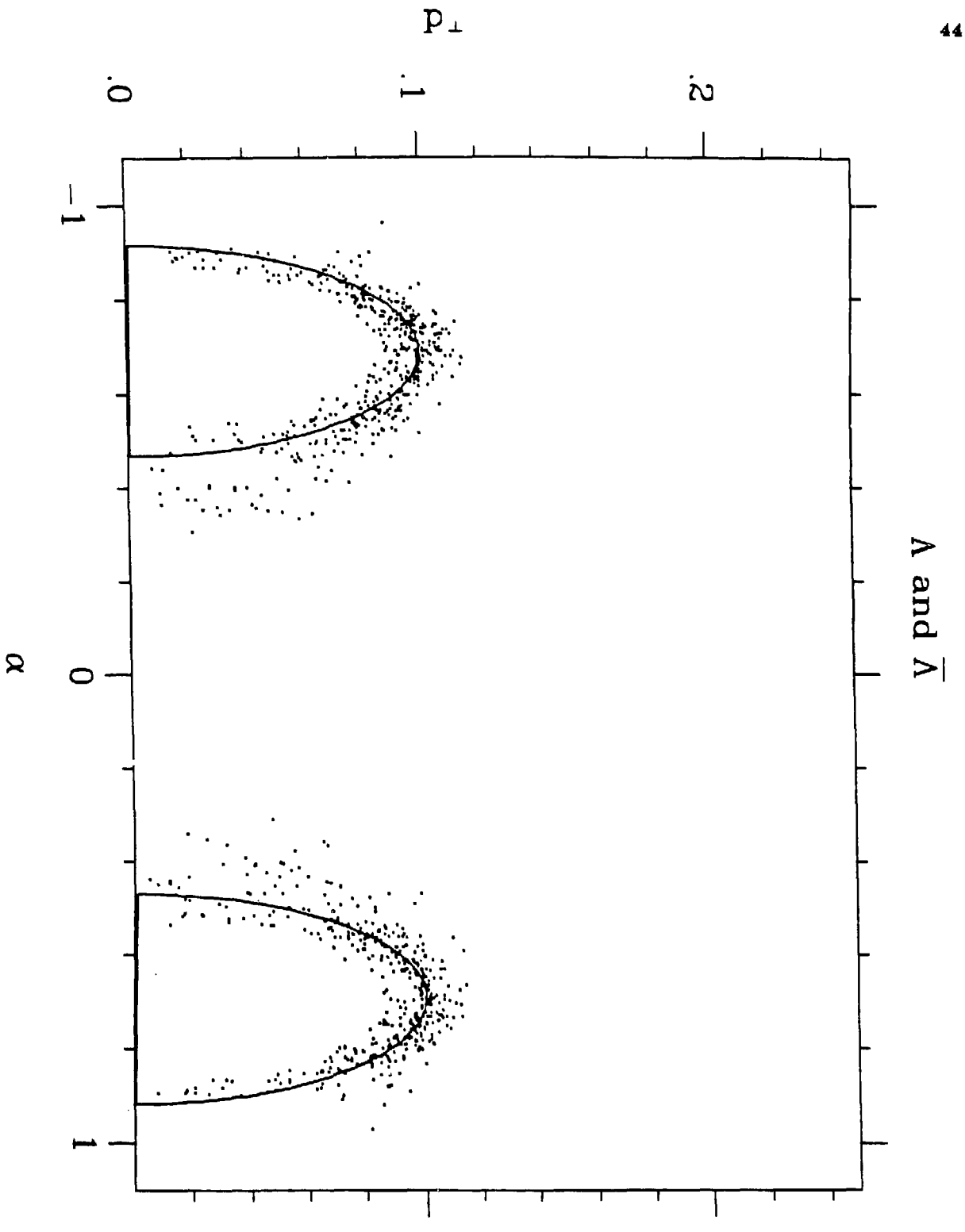

Figure 3.11. "α" vs. $p_\perp$ for $\Lambda/\bar{\Lambda}$ candidates (Data).

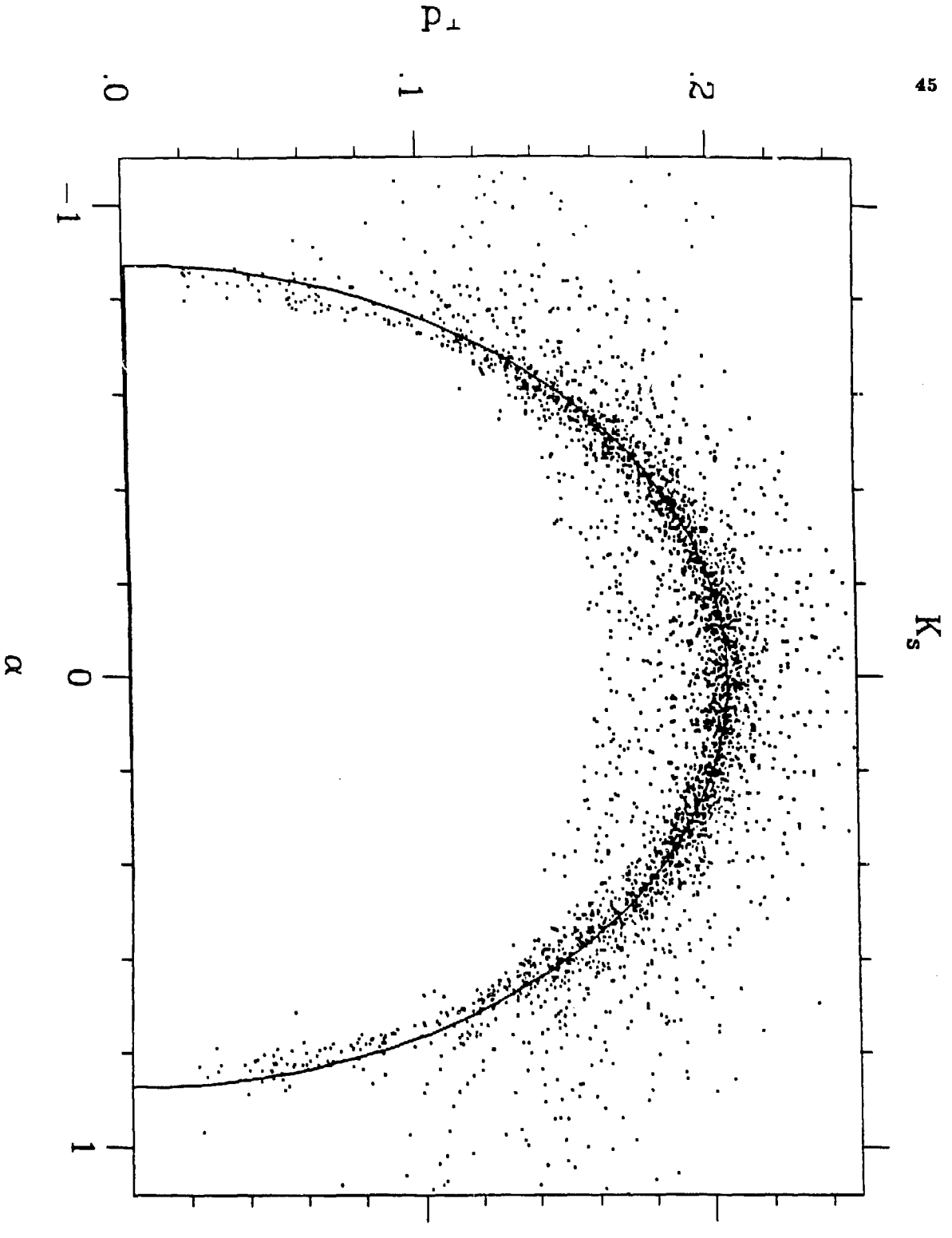

Figure 3.12. "α" vs. $p_\perp$ for K_s candidates (Data).

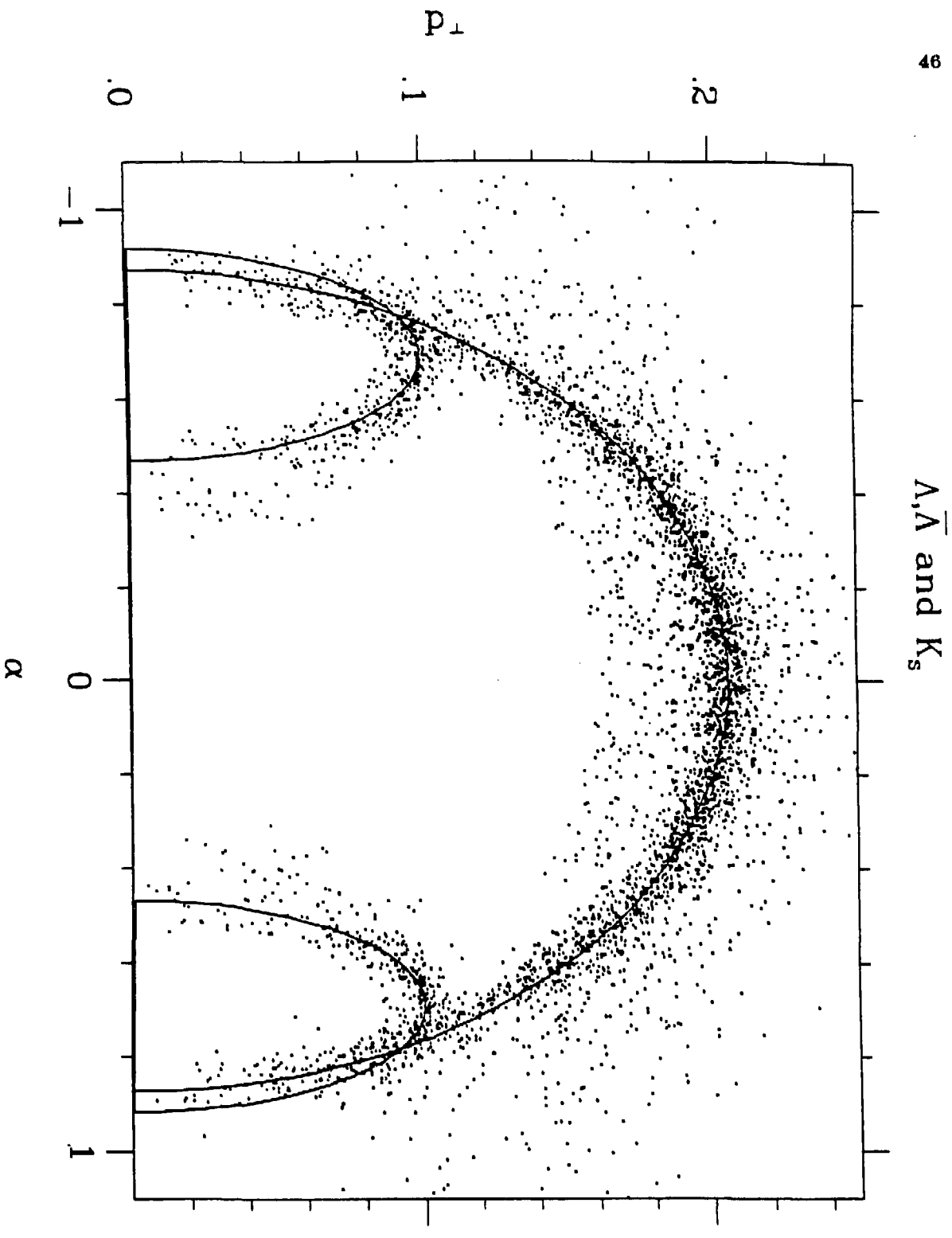

Figure 3.13. "α" vs. $p_\perp$ for K_s and $\Lambda/\bar{\Lambda}$ candidates (Data).

- the momentum of the Λ candidate be $> .5$ GeV $/c$.

This last cut on momentum is made to cut out the low efficiency region for finding $\Lambda/\bar{\Lambda}$. Figure 3.14 shows the $m(p\pi)$ spectrum before and after these cuts. The signal-to-noise is increased from $\sim 942 : 2274$ (or 0.4) to $\sim 715 : 306$ (or 2.3) with a loss of $\sim 24\%$ in signal. The number of $\Lambda/\bar{\Lambda}$ candidates with mass between $1.106 - 1.126$ GeV $/c^2$ is ~ 715 above background. In Figure 3.15 we see the $m(p\pi)$ distribution components in the Monte Carlo after cuts. Note the huge reduction in the combinatoric background.

3.3 Systematic Uncertainties

From work done by Heidi Schellman [22], the efficiency of the tracking through the drift chamber was found to be independent of momentum. However, the Monte Carlo efficiency for tracking was found to be $1.5 \pm 1.5\%$ too high relative to the good quality data with a total systematic uncertainty of $\pm 3.0\%$ due to discrepancies in the simulation with respect to very poorly measured tracks. Since the decay mode $\Lambda \rightarrow p\pi^-$ involves two tracks, we reduce the total detection efficiency by a factor of $(1 - 1.5\%)^2 = 97.0\%$ with an uncertainty of $\sim \pm 6.0\%$.

As stated above, the $\Lambda \rightarrow p\pi^-$ efficiency has an additional uncertainty due to dependency of the hadronic efficiency on whether or not a $\Lambda \rightarrow p\pi^-$ (and/or $\bar{\Lambda} \rightarrow \bar{p}\pi^+$) decay was present. This uncertainty is estimated to be $\pm 4.0\%$.

Using the LUND Monte Carlo programs, we find a total efficiency for $\Lambda \rightarrow p\pi^-$ to be $21.6 \pm .3\%$. This efficiency is 2.6% higher than that obtained using the BQCD Monte Carlo. We therefore assign an additional conservative uncertainty of $\pm 5.0\%$ to the $\Lambda \rightarrow p\pi^-$ efficiency.

An additional uncertainty to consider is one due to the systematics of the algorithm as described above. Higher momentum $\Lambda/\bar{\Lambda}$ particles decay relatively far away from the interaction point, and the two tracks from the decay are

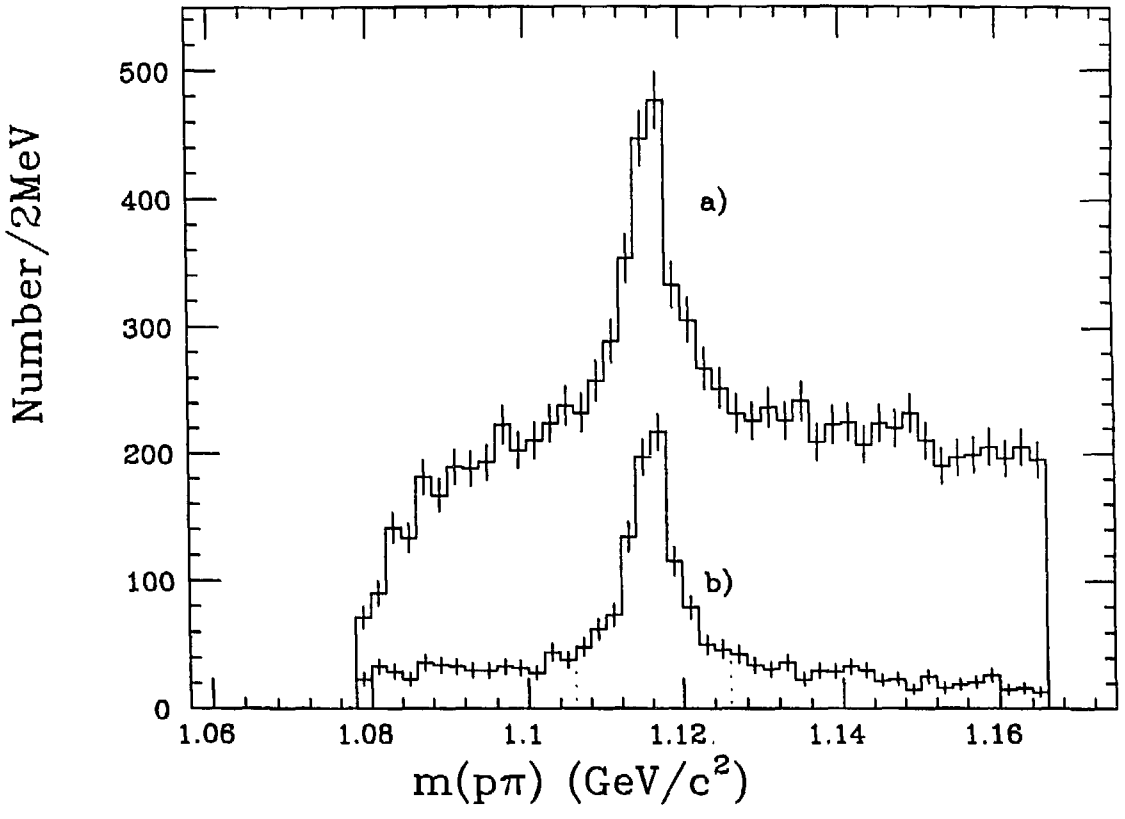

Figure 3.14. $m(p\pi)$ distributions a) before cuts and b) after cuts. For the number of events in figure a) see Figure 3.3. For figure b), the number of events within dotted lines (1.106GeV $\leq$ $m(p\pi)$ $<$ 1.126GeV) is 1021. The background (using adjacent bins) is estimated to be 306, leaving 715 events in the peak.

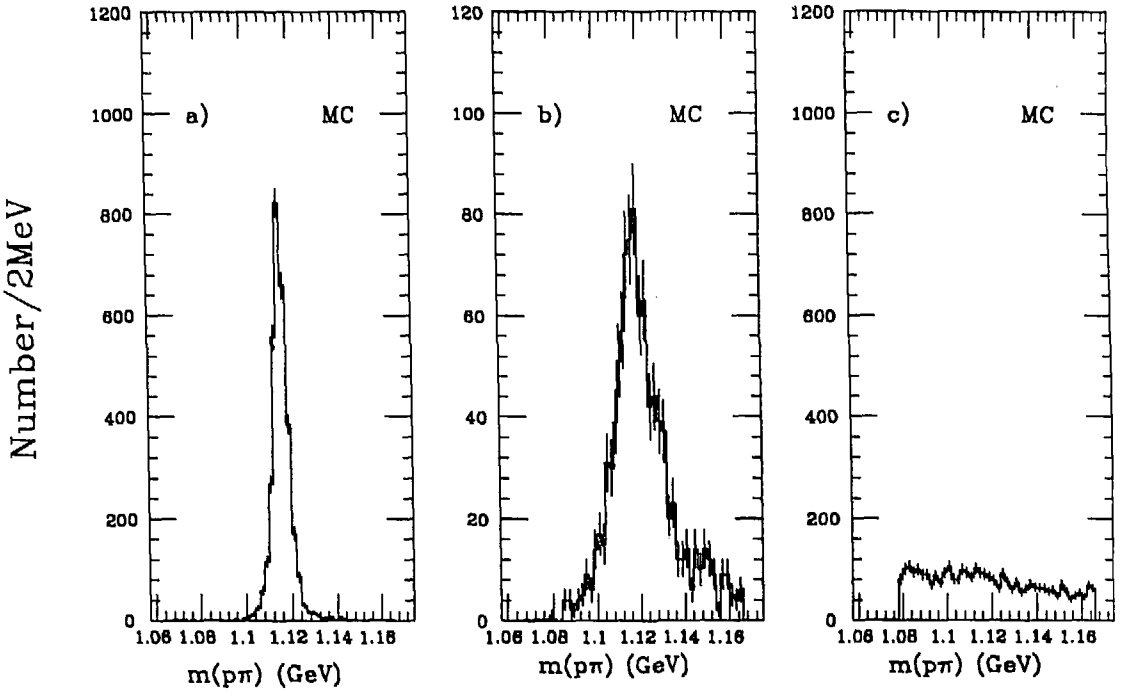

Figure 3.15. The three components in the $m(p\pi)$ spectrum after cuts are a) real $\Lambda/\bar{\Lambda}$s, b) K_s contamination (note scale), and c) combinatoric contamination.

difficult to resolve. Those that were resolved as two tracks would have the two tracks close together. The error in vertexing such a pair of tracks will be large, since any small change in the perpendicular position of the track(s) would introduce a large change in the vertex position in the radial direction. Also, the uncertainty in Δz as described above would also increase since the z position of each track is determined at the point of the vertex. We therefore assign an uncertainty of $\pm 7.0\%$ due to the systematics of vertexing.

The systematic uncertainty in the hadronic efficiency is estimated to be $\pm 4.0\%$ (see Jim Patrick thesis [19]).

The total luminosity from the luminosity monitors was found to be systematically high by a factor of $5.0 - 8.0\%$ for different data sets [23]. Cross-sections are therefore corrected by the respective amounts, with a luminosity uncertainty of $\sim 5.0\%$.

4. Results

4.1 Cross-Section and Hadronic Rate Measurement

4.1.1 Radiative Corrections

It is common for the results of cross-section measurements to be quoted assuming all processes occur thru the $O(\alpha^2)$ tree-level cross-section $\sigma_0(s)$ (see Eqn. 1.1 and Figure 1.1(c)). This is accomplished through renormalizing the efficiency for the process as calculated using Monte Carlo simulation. The total efficiency ϵ_{Total} for some process to occur is given by

$$\epsilon_{Total} = \frac{N(detected)}{N_{Total}(produced)} = \frac{\sigma(detected)}{\sigma(produced)}$$

where $N(detected)$ ($N_{Total}(produced)$) refer to the number of events detected (produced) by the Monte Carlo program given a cross-section $\sigma(produced)$. In order to quote the results for a radiative corrected cross-section, one substitutes $N_0(produced)$ for $N(produced)$ with the subscript 0 referring to the tree-level process. The radiative corrected efficiency is then given by

$$\epsilon_0 = \frac{N(detected)}{N_0(produced)} = \frac{\sigma(detected)}{\sigma_0(produced)}.$$

Using Eqn. 1.2 we can rewrite $\sigma_0(produced)$ as $\sigma_{NORAD}/(1+\delta)$, giving the radiative corrected efficiency

$$\epsilon_0 = \frac{\sigma(detected)}{\sigma_{NORAD}(produced)}(1+\delta) = \frac{N(detected)}{N_{NORAD}(produced)}(1+\delta) = \epsilon_{NORAD}(1+\delta)$$

where $\delta = \delta(s, k_0)$. When presenting the results of a measurement of the hadronic rate ($R_{\Lambda/\bar{\Lambda}} = \sigma(e^+e^- \to \Lambda/\bar{\Lambda} + X)/\sigma(e^+e^- \to HADRONS)$ for producing $\Lambda/\bar{\Lambda}$ particles, notice that the radiative corrections tend to cancel. To see this, we write $R_{\Lambda/\bar{\Lambda}}$

as

$$R_{\Lambda/\bar{\Lambda}} = \frac{N_{\Lambda/\bar{\Lambda}}(detected)}{N_{HADRON}(detected)} \frac{\epsilon_0(HADRON)}{\epsilon_0(\Lambda/\bar{\Lambda})}$$

$$= \frac{N_{\Lambda/\bar{\Lambda}}(detected)}{N_{HADRON}(detected)} \frac{\epsilon_{NORAD}(HADRON)/(1+\delta)}{\epsilon_{NORAD}(\Lambda/\bar{\Lambda})/(1+\delta)}$$

$$= \frac{N_{\Lambda/\bar{\Lambda}}(detected)}{N_{HADRON}(detected)} \frac{\epsilon_{NORAD}(HADRON)}{\epsilon_{NORAD}(\Lambda/\bar{\Lambda})}$$

where now $N_{\Lambda/\bar{\Lambda}}$ and N_{HADRON} refer to the number detected in the data. If the ratios $\epsilon_{Total}(HADRON)/\epsilon_{Total}(\Lambda/\bar{\Lambda})$ and $\epsilon_{NORAD}(HADRON)/\epsilon_{NORAD}(\Lambda/\bar{\Lambda})$ are equal, then the rate is independent of whether or not radiative corrections have been included. To check this, we use the BQCD Monte Carlo, and find $\epsilon_{Total}(\Lambda/\bar{\Lambda}) = 0.190 \pm 0.002$, $\epsilon_{NORAD}(\Lambda/\bar{\Lambda}) = 0.280 \pm 0.003$, $\epsilon_{Total}(HADRON) = 0.593 \pm 0.001$, and $\epsilon_{NORAD}(HADRON) = 0.950 \pm 0.001$ to find

$$\frac{\epsilon_{Total}(\Lambda/\bar{\Lambda})}{\epsilon_{Total}(HADRON)} = 0.295 \pm 0.003$$

and

$$\frac{\epsilon_{NORAD}(\Lambda/\bar{\Lambda})}{\epsilon_{NORAD}(HADRON)} = 0.320 \pm 0.003$$

where we have not included the $Br(\Lambda \rightarrow p\pi^-)$ since we are concerned only with the actual efficiency for detecting decays. This $\sim 3\%$ difference in the $\Lambda/\bar{\Lambda}$-to-HADRONIC efficiency due to radiation will be considered a systematic uncertainty in the radiative corrected cross-section and rate measurements in following sections. We shall present results from measurements of the inclusive cross-section $\sigma(e^+e^- \rightarrow \Lambda/\bar{\Lambda}\ X)$ along with the differential cross-sections $d\sigma/dp$ and $(s/\beta)\ d\sigma/dx$. For what follows, the $Br(\Lambda \rightarrow p\pi^-)$ is implicitly included.

4.2 Background Subtraction

As seen in Figure 3.15, the $m(p\pi)$ distribution has a background due to misidentified K_s particles and to random combinations of positive and negative

charged tracks (hereafter referred to as the combinatorial background). The K_s background will be subtracted statistically based on the $m(\pi\pi)$ distribution as will the combinatorial background based on the $m(p\pi)$ distribution.

4.2.1 K_s Subtraction

To subtract the K_s background, we look at the $m(\pi\pi)$ distribution and choose a signal and wing region. Figure 4.1 shows the $m(\pi\pi)$ distribution with the signal and wing region delineated for all $\Lambda/\bar{\Lambda}$ candidates plus background and Figure 4.2. shows the same distribution for those $\Lambda/\bar{\Lambda}$ candidates plus background which satisfy $1.106\,\mathrm{GeV}/c^2 \leq m(p\pi)) < 1.126\,\mathrm{GeV}/c^2$ (this criterion is important and will be detailed further in the following section). The K_s subtraction is done by assigning a weight according to the region into which the $\pi\pi$ mass falls. If $477MeV < m(\pi\pi) < 517MeV$ (signal region), the weight is 0. If $426MeV < m(\pi\pi) < 460MeV$ (wing region), the weight is 2. All other values for $m(\pi\pi)$ have a weight 1. This weight is then used in the histogramming of the $m(p\pi)$ mass and of other distributions of interest (momentum, etc.). Figure 4.3 shows the resulting $m(p\pi)$ distribution in the data after all cuts and after the K_s background subtraction. Figure 4.4 shows the three components (real $\Lambda/\bar{\Lambda}$, K_s's misidentified, and all other sources) of the resulting $m(p\pi)$ distributions using events generated by Monte Carlo simulation, or "MC events" for short. The K_s contamination is considerably reduced from that in Figure 3.15.

4.2.2 Subtraction of Combinatorial Background

To subtract the background from the combination of two random oppositely charged tracks, we use the wing region in the $m(p\pi)$ distribution to tell us how much background there is under the $\Lambda/\bar{\Lambda}$ peak, and the shape of the distribution of quantities of interest and subtract it. Figure 4.3 shows the $m(p\pi)$ distribution after all cuts and after the K_s subtraction, along with the

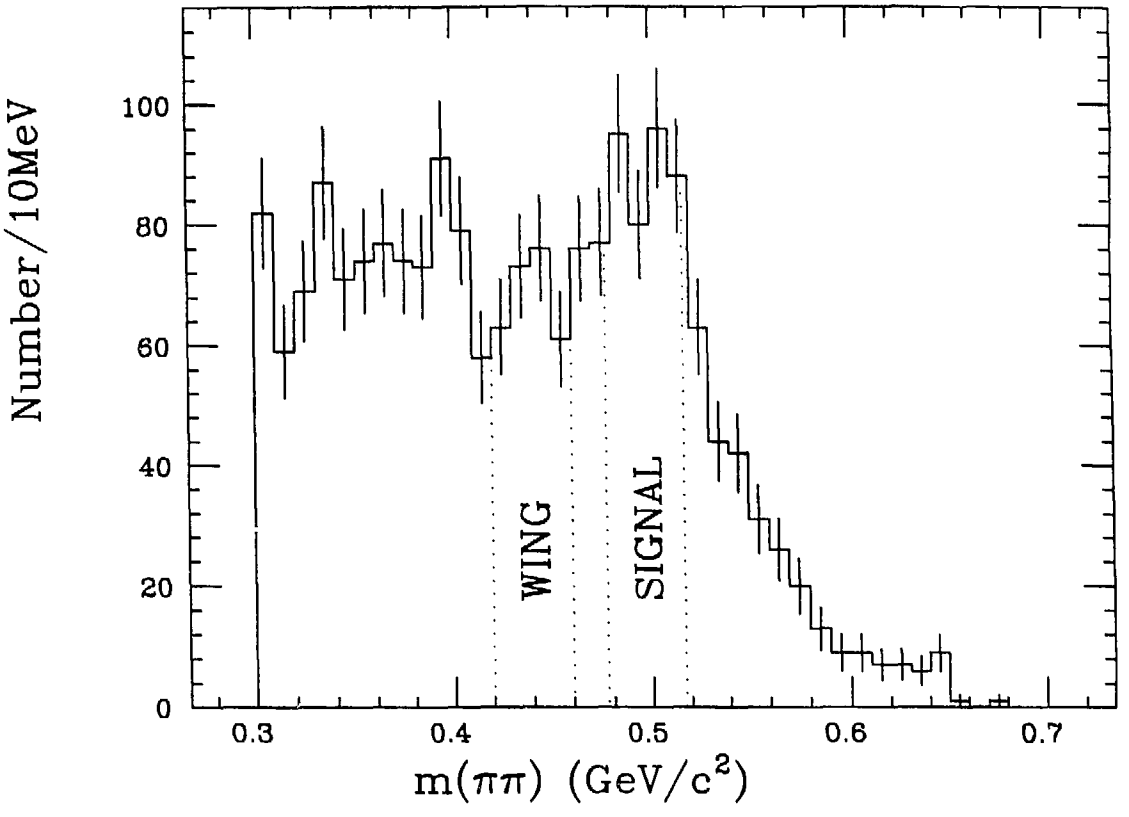

Figure 4.1. $m(\pi\pi)$ for all $\Lambda/\bar{\Lambda}$ candidates plus background after all cuts. Dotted lines delineate the signal ($477MeV < m(\pi\pi) < 517MeV$) and wing ($426MeV < m(\pi\pi) < 460MeV$) regions for the K_s subtraction. Total number of points: 1967

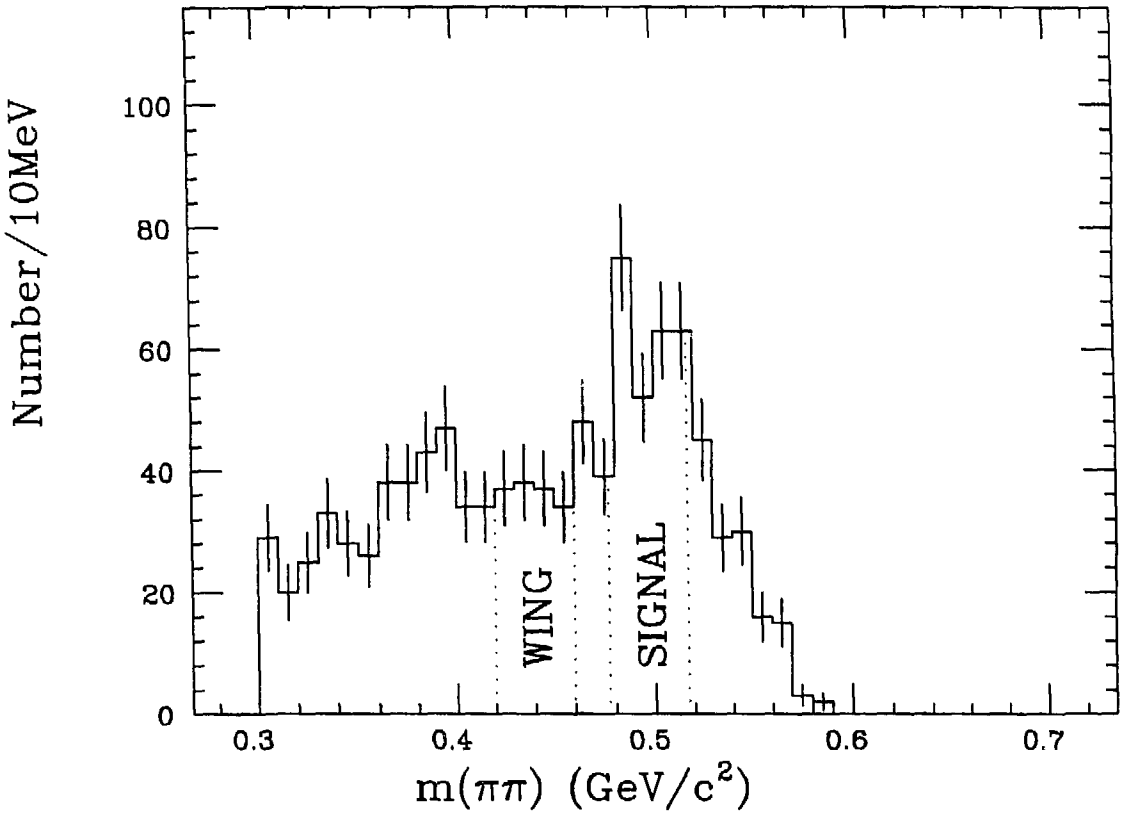

Figure 4.2. $m(\pi\pi)$ for $\Lambda/\bar{\Lambda}$ candidates in the peak region after all cuts. Dotted lines delineate the signal ($477MeV < m(\pi\pi) < 517MeV$) and wing ($426MeV < m(\pi\pi) < 460MeV$) regions for the K_s subtraction. Total number of points: 1021

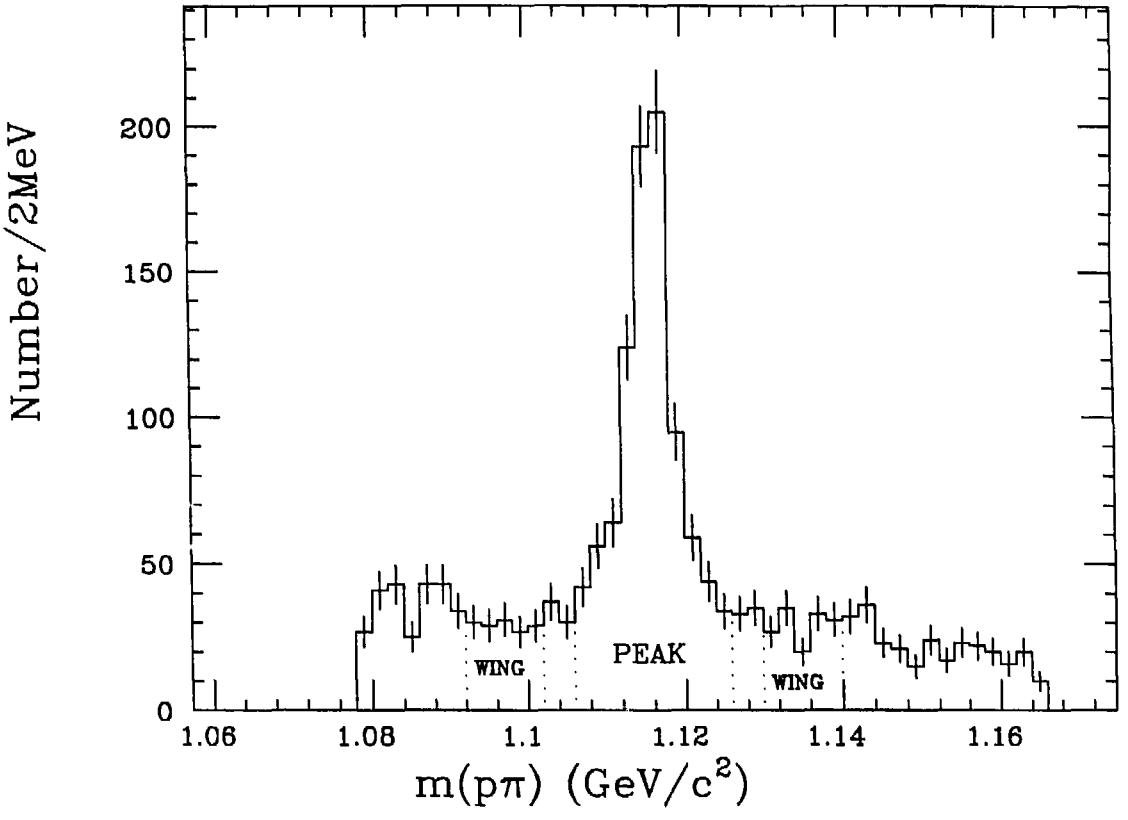

Figure 4.3. $m(p\pi)$ distribution after all cuts and after K_s's are subtracted. Wing regions are 1.092GeV $\leq m(p\pi) <$ 1.102GeV and 1.130GeV $\leq m(p\pi) <$ 1.140GeV. Peak region is 1.106GeV $\leq m(p\pi) <$ 1.126GeV. Total number of points: 146 in left wing, 146 in right wing (summed to 292), and 916 in peak leaving 624 after subtraction.

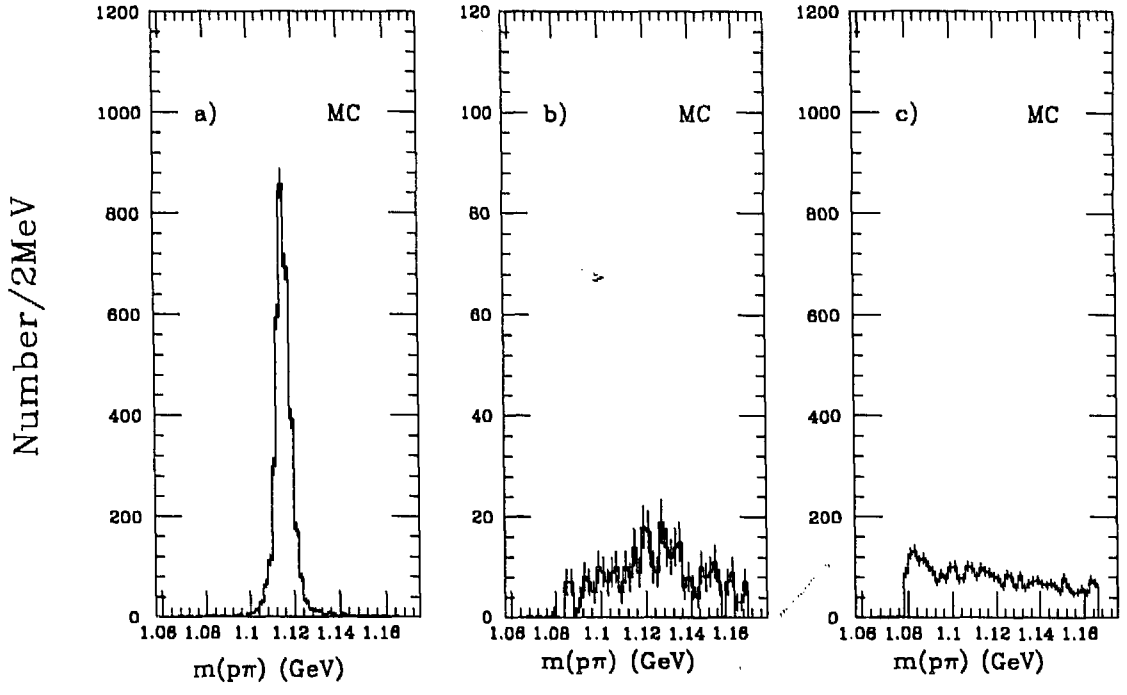

Figure 4.4. The three components in the $m(p\pi)$ spectrum after cuts and after K_s subtraction: a) real $\Lambda/\bar{\Lambda}$s, b) K_s contamination (note scale), and c) combinatoric contamination.

peak ($1.106\text{GeV} \leq m(p\pi) < 1.126\text{GeV}$) and wing ($1.092\text{GeV} \leq m(p\pi) < 1.102\text{GeV}$ and $1.130\text{GeV} \leq m(p\pi) < 1.140\text{GeV}$) regions used in subtracting the combinatoric background. In Figure 4.5 we see results for the momentum distribution and in Figure 4.6 the $p_\perp$ (relative to the sphericity axis) distribution after the K_s subtraction and after the "peak-wing" subtraction. The poor agreement between Monte Carlo and data shown in Figure 4.5 (attributed to poor modeling of the produced distribution by the BQCD Monte Carlo simulation) necessitates constructing a momentum dependent efficiency. The $p_\perp$ distribution in Figure 4.6, on the other hand, shows good agreement between the Monte Carlo and the data. This agreement is important, since if the Monte Carlo were to produce $\Lambda/\bar{\Lambda}$ particles with an artificially high (low) $p_\perp$ distribution relative to the jet axis, the resulting efficiency would be artificially high (low) due to the fact that efficiency is a function of the track density.

4.3 $\sigma(e^+e^- \to \Lambda/\bar{\Lambda} + X)$ FOR $p_{\Lambda/\bar{\Lambda}} > .5\,\text{GeV}/c$

To measure the total inclusive cross-section we first measure the differential cross-section $d\sigma/dp$ with $p > .5\,\text{GeV}/c$ for each data set (see section 2.11) and integrate over momentum bins. Table 4.1 summarizes the "cross-sections" (measured number of events per luminosity) for the different data sets along with the normalizations. Errors are statistical only. We then normalize the different distributions to the value 72±4.5 pb for the cross-section obtained for the NEWDAT data set (with a total integrated luminosity of $79.8pb^{-1}$) and sum together to get the inclusive cross-section $\sigma(e^+e^- \to \Lambda/\bar{\Lambda} + X)$ for $p_{\Lambda/\bar{\Lambda}} > .5\,\text{GeV}/c$.

Figure 4.7 shows the efficiency for detecting $\Lambda/\bar{\Lambda}$ particles. In this figure and the remainder of this section, radiative corrections and $Br(\Lambda \to p\pi^-)$ are included. The slight rise at high momentum is not very significant due to the very small cross-section and low statistics there. Figure 4.8 shows the inclusive

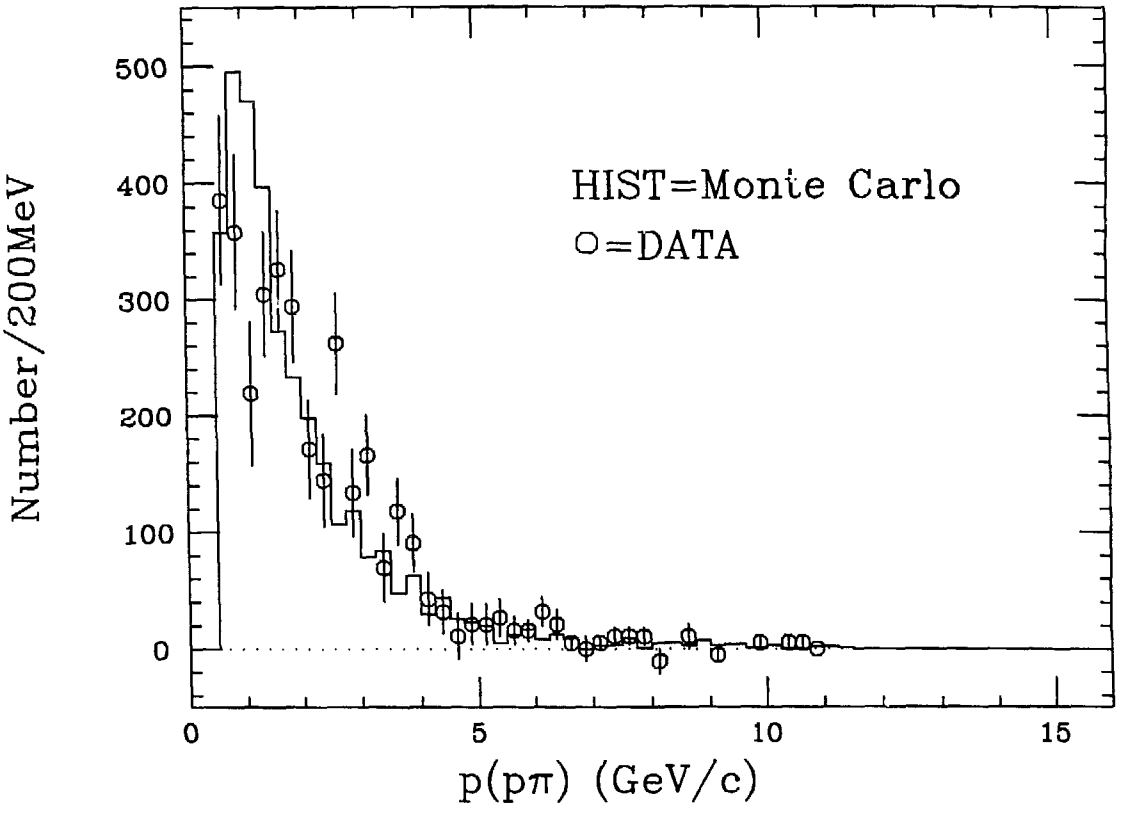

Figure 4.5. Momentum distribution after K_s subtraction and after "peak-wing" subtraction using the NEWDAT data set (points) before efficiency corrections. The histogram is from the BQCD Monte Carlo. Sum over all data points: 624

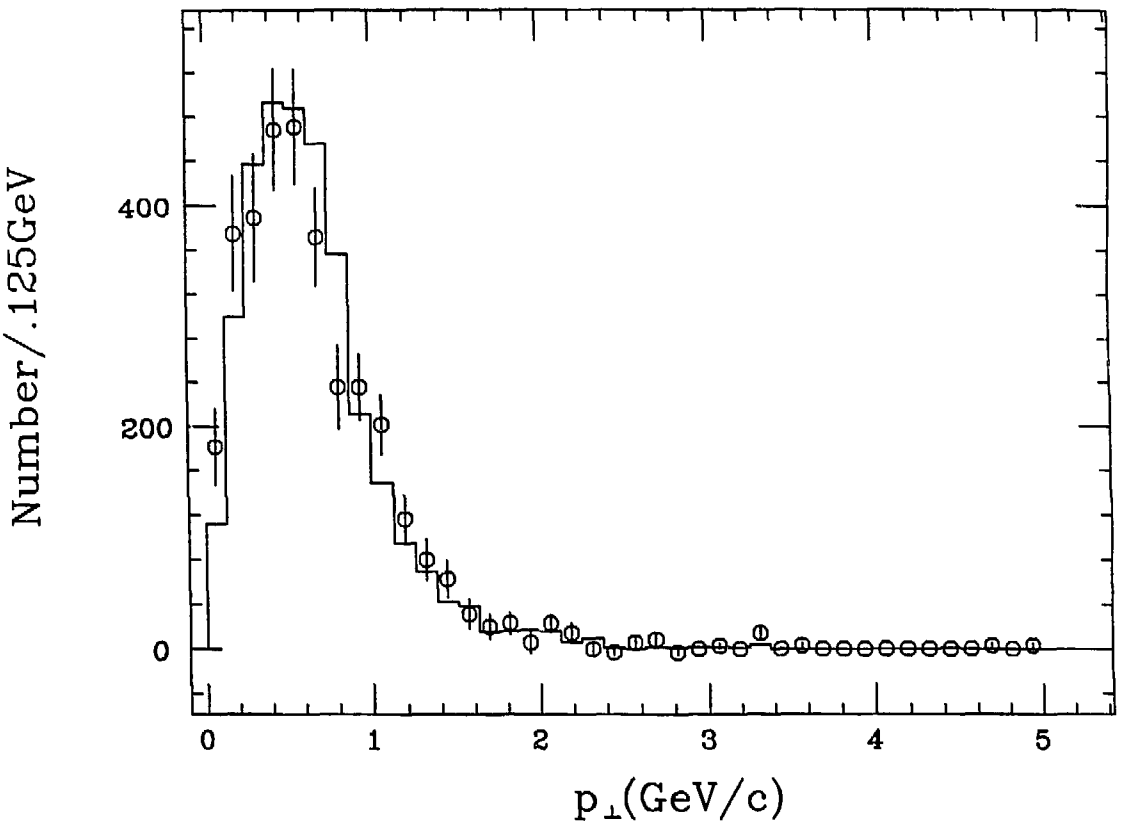

Figure 4.6. $p_\perp$ relative to sphericity axis after K_s subtraction and after "peak-wing" subtraction using the NEWDAT data set. Sum over all data points: 624

Table 4.1. Result of measured number of events per luminosity for the different data sets, normalized to the NEWDAT value.

Data Set	Luminosity	$\sigma_{\Lambda/\bar{\Lambda}}(p > .5\text{GeV})$ (pb)	Normalization
VCSUM	17.2	63.2 ± 11.8	$1.140 \pm .224$
SPRING2	57.9	44.4 ± 4.6	$1.622 \pm .195$
OXYGEN	24.2	59.1 ± 7.9	$1.219 \pm .179$
NEWDAT	79.8	72.1 ± 4.5	1.00

differential cross-section $d\sigma/dp$ and Figure 4.9 shows the inclusive differential cross-section $(s/\beta)\ d\sigma/dx$ where $x \equiv E_\Lambda/E_{beam}$ using the data sets in Table 4.1 normalized to the result obtained from the NEWDAT data set. The data for these two distributions are given in Table 4.2. Figure 4.10 shows a comparison of results from this thesis with results from other experiments. Errors in results from this thesis are statistical only.

4.4 Total Cross-section

To correct the inclusive cross-section for the production of $\Lambda/\bar{\Lambda}$ with momentum $p < .5\,\text{GeV}/c$, we presume a functional form for the matrix element and fit to the measured differential cross-section. The form of the function chosen is

$$\frac{d\sigma}{dp} = \frac{4\pi p^2}{E}[a_1 e^{-b_1 p} + a_2 e^{-b_2 p}] \qquad (4-1)$$

where E and p are the energy and momentum of the $\Lambda/\bar{\Lambda}$ and a_1, a_2, b_1, and b_2 are parameters to be determined from the fit. The first part $(4\pi p^2/E)$ is from phase space considerations. This is multiplied by the sum of the two exponentials, a form chosen to fit the shape of $d\sigma/dp$ with the requirement that $d\sigma/dp \to 0$ as $p \to 0$ (see Figure 4.8). The fit results in a χ^2 of 7.2 for $14 - 4 = 10$ degrees of

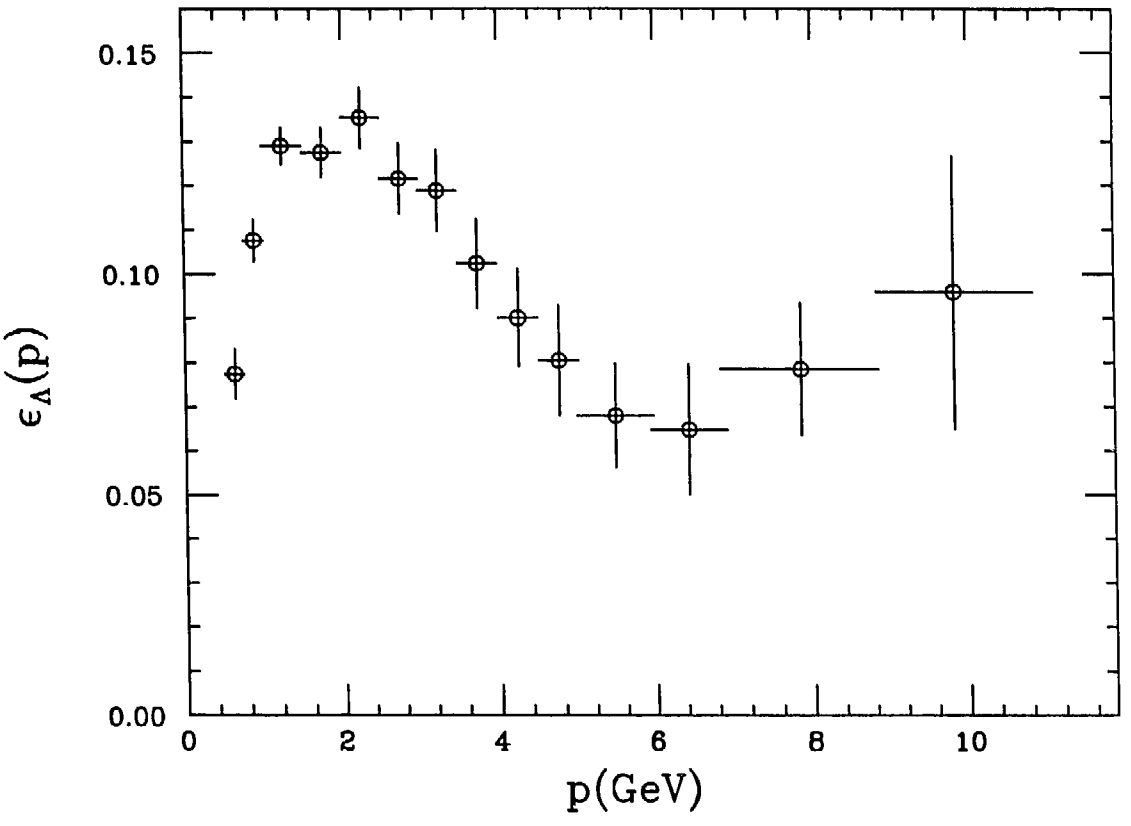

Figure 4.7. Efficiency with radiative corrections and $Br(\Lambda \rightarrow p\pi^-)$ included.

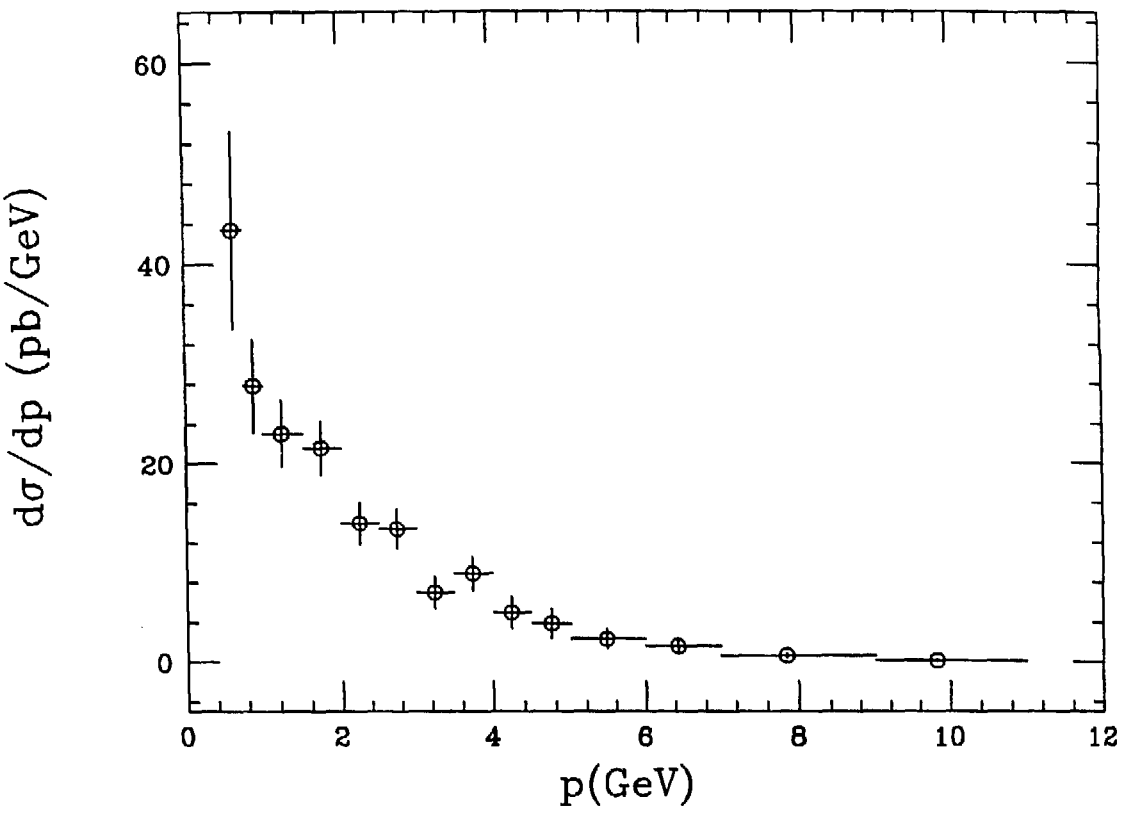

Figure 4.8. $d\sigma/dp$ using 179.1pb sample normalized as to Table 4.1. Radiative corrections and $Br(\Lambda \to p\pi^-)$ included.

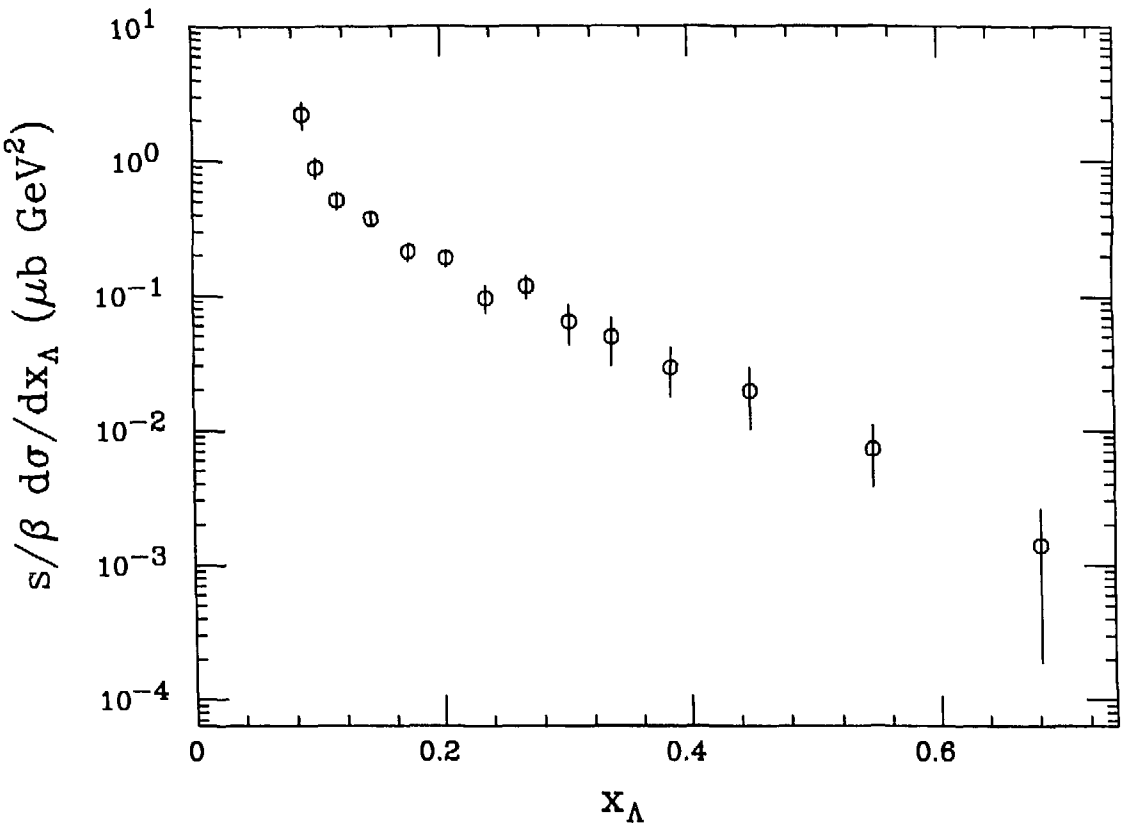

Figure 4.9. $(s/\beta)\ d\sigma/dx$ using 179.1pb sample normalized at to Table 4.1. The variable "x" is the $\Lambda/\bar{\Lambda}$ energy normalized to the beam energy. Radiative corrections and $Br(\Lambda \rightarrow p\pi^-)$ are included.

Table 4.2. $d\sigma/dp$ and $(s/\beta)d\sigma/dx$ for $p > .5$GeV.

p(GeV)	$d\sigma/dp$(pb/GeV)	x	$(s/\beta)d\sigma/dx$(nbGeV^2)
0.625	43.352 ± 9.822	0.088	2213.0 ± 501.4
0.875	27.814 ± 4.673	0.098	890.5 ± 149.6
1.234	23.000 ± 3.374	0.115	509.7 ± 74.8
1.735	21.548 ± 2.705	0.142	371.4 ± 46.6
2.243	13.931 ± 2.120	0.173	211.9 ± 32.3
2.740	13.346 ± 1.991	0.204	189.7 ± 28.3
3.235	6.965 ± 1.588	0.236	95.0 ± 21.7
3.739	8.823 ± 1.682	0.269	117.2 ± 22.3
4.241	4.894 ± 1.610	0.302	63.8 ± 21.0
4.747	3.829 ± 1.490	0.336	49.3 ± 19.2
5.476	2.310 ± 0.936	0.385	29.3 ± 11.9
6.431	1.561 ± 0.740	0.450	19.6 ± 9.3
7.844	0.586 ± 0.280	0.546	7.3 ± 3.5
9.823	0.113 ± 0.098	0.682	1.4 ± 1.2

freedom and yield the values

$$a_1 = 94.65 \pm 17.64 \text{ pb/GeV}^2$$

$$a_2 = 4.08 \pm 0.26 \text{ pb/GeV}^2$$

$$b_1 = 4.10 \pm 0.06 \text{ GeV}^{-1}$$

$$b_2 = 0.86 \pm 0.02 \text{ GeV}^{-1}$$

The normalized covariance matrix for a_1, a_2, b_1, and b_2 is found to be

$$\begin{pmatrix} 1 & - & - & - \\ -.061 & 1 & - & - \\ .166 & -.015 & 1 & - \\ .215 & .346 & -.087 & 1 \end{pmatrix}.$$

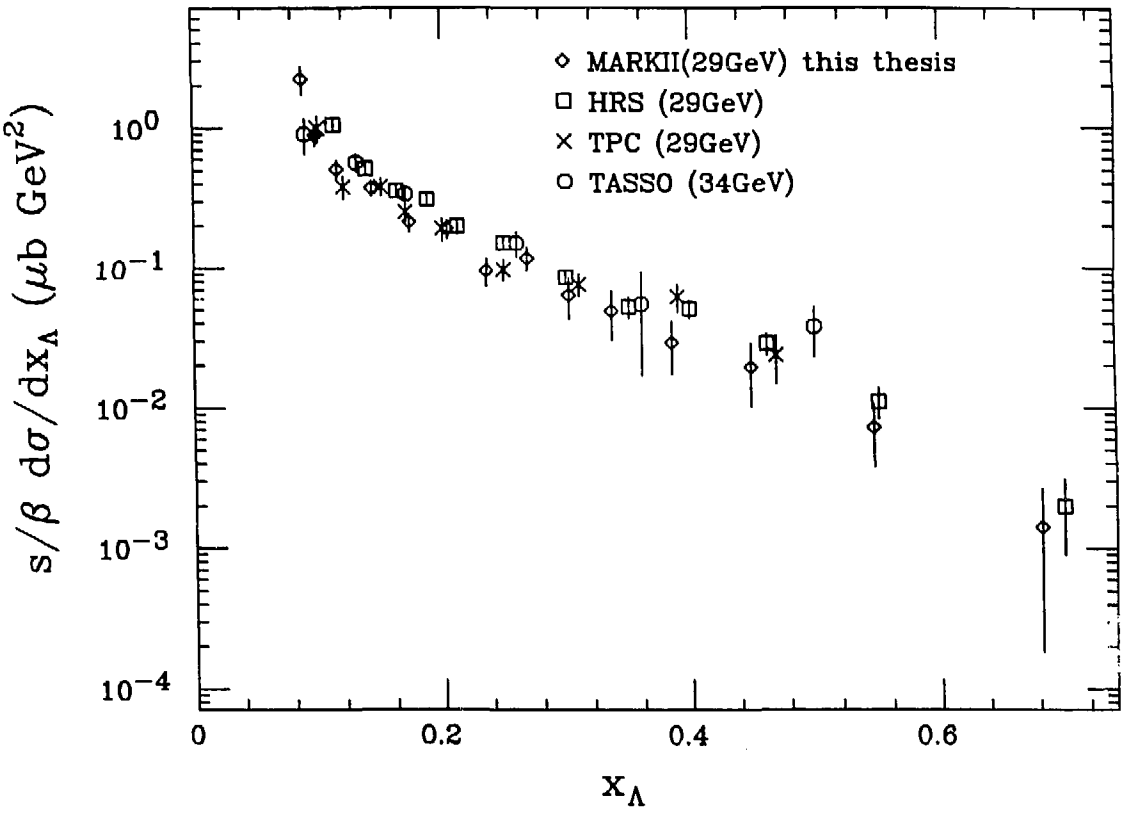

Figure 4.10. Comparison of $(s/\beta)\ d\sigma/dx$ with other experiments.

Figure 4.11 shows the data along with resulting fit. The two exponentials are plotted separately as smooth curves. The cross-section using this fit was found to be 69.1 pb for $p \geq .5\,\mathrm{GeV}/c$ (compared to the measured value of 72.1 pb) and 11.3 pb for $p < .5\,\mathrm{GeV}/c$. Based on these results we add a systematic uncertainty of ± 5 pb to the total cross-section uncertainty. We summarize all estimates of systematic uncertainties (see section 3.3), in Table 4.3 and arrive at a total cross-section

$$\sigma(e^+e^- \rightarrow \Lambda/\bar{\Lambda} + X) = 83.4 \pm 5.1 \pm 9.8\mathrm{pb}$$

where the first uncertainty is statistical and the second systematic. Again, radiative corrections and $Br(\Lambda \rightarrow p\pi^-)$ are included.

4.5 Hadronic Rate

Using the value for $R \equiv \sigma(HADRONIC)/\sigma(\mu\mu) = 4.0$ and the muon cross-section $\sigma(\mu\mu) = 103.3\mathrm{pb}$ we calculate the $\Lambda/\bar{\Lambda}$ hadronic rate to be

$$\begin{aligned} R_{\Lambda/\bar{\Lambda}} &= \frac{\sigma(e^+e^- \rightarrow \Lambda/\bar{\Lambda}X)}{\sigma(e^+e^- \rightarrow HADRONS)} \\ &= .202 \pm .011 \pm .024 \end{aligned}$$

where again the first (second) error describes the statistical (systematic) uncertainty. Table 4.4 compares this to the values quoted by other experiments.

4.6 Polarization and CP Violation

In the decay $\Lambda \rightarrow p\pi^-$, the parity-violating weak interaction allows the angular momentum of the $p\pi$ final state to be either s-wave or p-wave [28]. If we start with a collection of Λ's (but not $\bar{\Lambda}$) fully polarized, the decay angular distribution of the protons from the decay in the Λ c.m. has the form

$$\frac{1}{N}\frac{dN}{d\cos\theta_n} = \frac{1 + \alpha_\Lambda \cos\theta_n}{2}$$

where θ_n is the angle between the proton in the c.m. of the decay and the spin $\vec{\sigma}$ of the Λ. The coefficient α_Λ is proportional to the product of the s-wave and

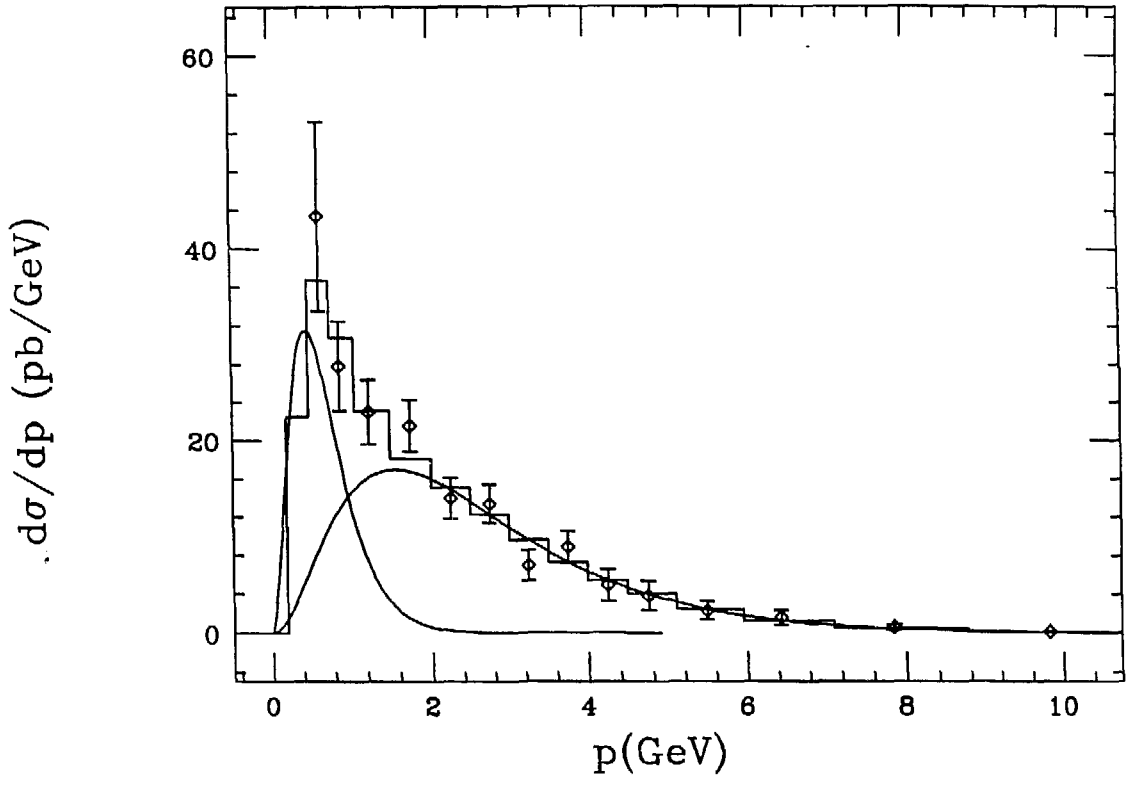

Figure 4.11. Fit of $d\sigma/dp$ to equation (4-1). Data are plotted. Histogram shows the result of the fit. The smooth curves show the two curves $(p^2/4\pi E)a_1e^{-b_1p}$ and $(p^2/4\pi E)a_2e^{-b_2p}$.

Table 4.3. Summary of systematic uncertainties.

Hadronic efficiency	±1.0%
Hadronic background	±1.5%
$\epsilon(\Lambda \to p\pi^-)$ MC dependency	±5.0%
Drift Chamber tracking efficiency	±6.0%
$\epsilon(\Lambda \to p\pi^-)$ dependency on hadronic cuts	±4.0%
Luminosity	±5.0%
Extrapolation of $d\sigma/dp$ to $p = 0.0\,\mathrm{GeV}/c$	±5.0pb

Table 4.4. Hadronic rate $R_{\Lambda/\bar{\Lambda}} = \sigma(\Lambda + \bar{\Lambda})/\sigma(HADRONS)$.

Collaboration	$R_{\Lambda/\bar{\Lambda}}$
MarkII (this thesis)	.202±.011±.024
MarkII (previous)[24,25]	.213±.012±.018
HRS[26]	.220±.007±.020
TPC[27]	.197±.012±.017

p-wave amplitudes for the decay and is measured[29] to be 0.642 ± 0.013. For Λ's with polarization P, the angular distribution is given by Eqn. 4.1

$$\frac{1}{N}\frac{dN}{d\cos\theta_n} = \frac{1 + P\alpha_\Lambda \cos\theta_n}{2}. \tag{4.1}$$

For $\bar{\Lambda} \to \bar{p}\pi^+$, the distribution has the same form with α_Λ replaced by $\alpha_{\bar{\Lambda}}$. CP invariance [30] requires $\alpha_\Lambda = -\alpha_{\bar{\Lambda}}$. (The R608 Collaboration[31], using Λ's produced in $pp \to \Lambda X$ and $\bar{\Lambda}$'s produced in $\bar{p}p \to \bar{\Lambda} X$ at the CERN ISR with center-of-mass energy $\sqrt{s} = 30.8\mathrm{GeV}$ finds $\alpha_\Lambda/\alpha_{\bar{\Lambda}} = -1.04 \pm 0.29$.) We therefore see that, as well known, the parity-violating weak decay of the Λ makes a measurement of the polarization possible. If the Λ (and $\bar{\Lambda}$) exhibits a polarization, we can then test

the production CP invariance.

The polarization of Λ and $\bar{\Lambda}$ baryons in hadronic fixed target experiments with incident beam momentum from 14 to 400 GeV [32,33,31,34,35] ($pp \to \Lambda X$, $p\bar{p} \to \bar{\Lambda} X$, $K^- p \to \Lambda X$, *nucleus* + *nucleus* $\to \Lambda X$, and others) is well established. Such polarization appears to be linear in $p_\perp$ (momentum of the $\Lambda/\bar{\Lambda}$ with respect to the incident beam direction) and a weakly increasing function of the $\Lambda/\bar{\Lambda}$ energy. QCD calculations[36] predict at most a very small polarization and thus fail to describe this phenomenon adequately. Other more phenomenological models[37,38] fit some of the data but not all[32,33].

It is interesting that the polarization of Λ's produced from proton beams on stationary targets is the same as that of $\bar{\Lambda}$'s produced from anti-proton beams and is non-zero. In the recombination picture where high energy hadronic production is via combinations of valence quarks (*uud* for proton and *udd* for neutron) and "sea" quarks ($u\bar{u}, d\bar{d}, s\bar{s}, etc$), one can theorize that polarization is a result of strong interaction spin-dependent forces among the valence quarks in the beam and target hadrons. The lack of polarization[39] in $pp \to \bar{\Lambda} X$ bears this out, since $\bar{\Lambda}$ production would proceed entirely from the recombination of "sea" quarks in this picture. In Figure 4.12 we present results for $p \to \Lambda$ and $\bar{p} \to \bar{\Lambda}$ (which shows polarization linearly dependent on $p_\perp$), $p \to \bar{\Lambda}$ (which shows no polarization), and $K^- \to \Lambda$ (which shows a polarization with the opposite sign) from selected hadronic fixed target experiments.

The search for polarization in $e^+e^- \to q\bar{q}$ is more complex. The flavor ($u, d, s, c,$ or b) and charge-conjugate state (q or $\bar{q}$) in jets are difficult to determine from the hadronic final state constituents. Such an exact knowledge of the hadronic event appears to be important in regards to $\Lambda/\bar{\Lambda}$ polarization since the above mentioned data (from fixed target experiments) indicate that it is the baryons

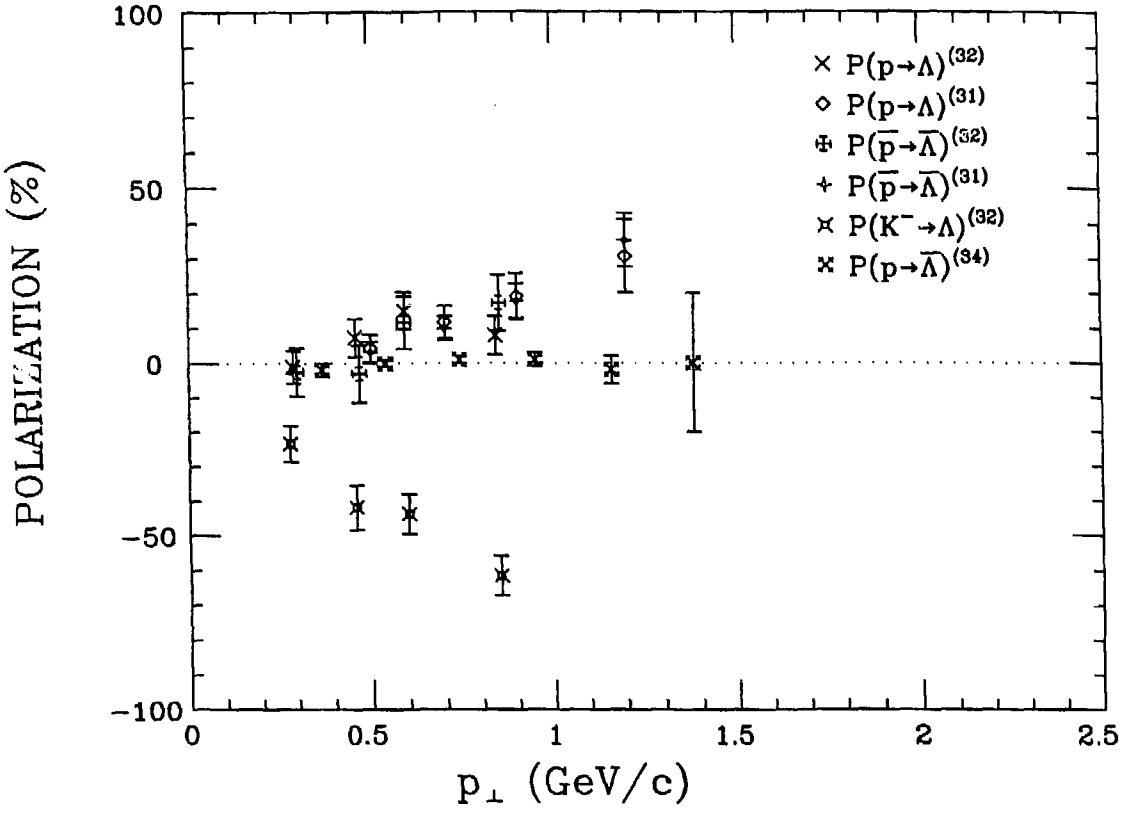

Figure 4.12. Polarization P from fixed target hadronic experiments. The dotted line is along $P = 0.0$.

from the quark state and the anti-baryons from the anti-quark state that exhibit polarization. Another way to say this is that the polarization of the baryon is a result of the hadronization process and is a function of the direction of the color field. Such a direction is known exactly in pp and $p\bar{p}$ collisions and poorly in $e^+e^- \rightarrow q\bar{q}$ annihilation. The fact that there appears to be an increase in polarization with $p_\perp$ as mentioned above indicates the dominance of the spin-dependent forces at short range. In $e^+e^- \rightarrow q\bar{q}$, hadronization is generally thought to be a more long-range phenomenon[40], and so we expect that the polarization is not introduced or affected in the hadronization process. In light of these comparisons of hadronic nucleon-nucleon physics with $e^+e^- \rightarrow q\bar{q}$, we present results of a search for polarization.

Parity conservation in strong interaction production dictates that any polarization must occur in the direction perpendicular to the production plane defined by the primary quark and decaying $\Lambda/\bar{\Lambda}$ momentum. The polarization of the spin $\vec{\sigma}$ is searched for by first estimating the quark direction using the sphericity axis[17] $\hat{u}_{sph}$ (with the requirement that $\hat{u}_{sph} \cdot \vec{p}_{\Lambda/\bar{\Lambda}} > 0$) and then forming the unit vector $\hat{n}$ out of the production plane given by

$$\hat{n} = \frac{\hat{u}_{sph} \times \vec{p}_{\Lambda/\bar{\Lambda}}}{|\hat{u}_{sph} \times \vec{p}_{\Lambda/\bar{\Lambda}}|}.$$

We then search for polarization in the $\hat{n}$ direction as a function of the momentum $p_\perp$ of the $\Lambda/\bar{\Lambda}$ perpendicular to the sphericity axis $\hat{u}_{sph}$.

We anticipate a large systematic uncertainty due to the use of the sphericity axis in determining the direction of the primary quark. Using the Monte Carlo simulation, we measure the distribution of $\langle \hat{u}_q \cdot \hat{u}_{sph} \rangle$ to have a width of $\sim \pm 10^o$. Thus the uncertainty in the direction of $\hat{n}$ (up or down in the production plane) will be larger in the region of small $p_\perp$. To estimate the systematic uncertainty,

we form the unit vector $\hat{t}$ in the production plane from $\vec{p}_{\Lambda/\bar{\Lambda}}$ and $\hat{n}$ defined by

$$\hat{t} = \frac{\vec{p}_{\Lambda/\bar{\Lambda}} \times \hat{n}}{|\vec{p}_{\Lambda/\bar{\Lambda}} \times \hat{n}|}.$$

Since parity conservation in strong interaction production prohibits polarization along the $\hat{t}$ direction, we measure the polarization there and use the results as an estimate of the systematic uncertainty. Another possible check on the systematics would be in a measurement of the polarization along the $\Lambda/\bar{\Lambda}$ momentum direction. However, the detection efficiency as a function of the decay angle along the boost direction is a strong function of the angle and the boost. Forward-backward decays (relative to the boost direction) where the proton is in the forward direction results in a pion which is boosted to an energy too low to be detected. We therefore use the decay angle in the plane perpendicular to the boost direction (along $\hat{t}$) to check systematics.

In order to extract the polarization, we fit the Λ and $\bar{\Lambda}$ $\cos\theta_n$ distributions separately and combined (as a function of $p_\perp$) to a straight line and solve for the polarization using Eqn. 4.1. If we combine the Λ and $\bar{\Lambda}$ $\cos\theta_n$ distributions with opposite signs ($\cos\theta_n \rightarrow -\cos\theta_n$ for the $\bar{\Lambda}$ candidates) and fit to a straight line, we can extract the polarization again using Eqn. 4.1. If we assume CP invariance holds ($\alpha_{\bar{\Lambda}} = -\alpha_\Lambda$), then the sum of the Λ and $\bar{\Lambda}$ distributions should have zero slope, but the measurement has meaning only if there is a polarization. We also calculate a polarization from the $K_s \rightarrow \pi^+\pi^-$ decays using the angular distribution of the π^+. This measurement serves as a check on the analysis as we expect no polarization from the decay $K_s \rightarrow \pi^+\pi^-$. For the $\Lambda/\bar{\Lambda}$ data, the polarization P is presented, and for the K_s decays, the slope of the distribution is presented in Table 4.5 using all 179.1pb of data (see Table 4.1). Both statistical (from the fit) and systematic (from measuring the polarization along $\hat{t}$) uncertainties are included. The "(-)" symbol indicates the above mentioned transformation

$\cos\theta_n \rightarrow -\cos\theta_n$ for the $\bar{\Lambda}$ candidates. To compare with the fixed target hadronic experiments mentioned above, we fit the $p \rightarrow \Lambda$ and $\bar{p} \rightarrow \bar{\Lambda}$ data (combined) from Figure 4.12 to a straight line as a function of $p_\perp$ and plot our results for the $\Lambda+\bar{\Lambda}$ and $\Lambda(-)\bar{\Lambda}$ data. Figure 4.13 shows the comparison. The combined statistical and systematic uncertainties are quite large. We conclude that in the $\Lambda(-)\bar{\Lambda}$ sample, the polarization as a function of $p_\perp$ is consistent with zero. We can make no statement on a check of CP invariance since we can only test CP invariance if the polarization is non-zero.

Table 4.5. Polarization along $\hat{n}$ (out of the production plane) from fit to $\cos\theta_n$ distributions for Λ, $\bar{\Lambda}$, and the combined distributions $\Lambda+\bar{\Lambda}$ and $\Lambda(-)\bar{\Lambda}$. The "(-)" symbol means we add the positive bins in $\cos\theta_n$ for Λ's to the negative bins in $\cos\theta_n$ for $\bar{\Lambda}$'s to account for the CP invariance requirement $\alpha_\Lambda = -\alpha_{\bar{\Lambda}}$. If polarization exists, it would be exhibited in the $P(\Lambda(-)\bar{\Lambda})$ distribution. If that distribution showed any deviation from zero, CP invariance could be tested by looking for any deviation from zero in the $P(\Lambda+\bar{\Lambda})$ distribution. Since the K_s is a scalar particle, we include the $P\alpha(K_s)$ distribution for a check on the analysis. For all distributions, the first uncertainty is statistical (from the fit) and the second deduced from the measurement of the polarization in the production plane (along $\hat{t}$), which (from parity conservation) is expected to be zero.

	all $p_\perp$	$p_\perp < 0.5$ GeV /c	0.5 GeV /$c \leq p_\perp < 1.0$ GeV /c	$p_\perp > 1.0$ GeV /c
$P(\Lambda)$	$0.188 \pm 0.170 \pm 0.100$	$0.269 \pm 0.276 \pm 0.178$	$0.117 \pm 0.268 \pm 0.187$	$0.139 \pm 0.369 \pm 0.275$
$P(\bar{\Lambda})$	$0.067 \pm 0.162 \pm 0.187$	$0.480 \pm 0.298 \pm 0.275$	$-.307 \pm 0.232 \pm 0.184$	$0.000 \pm 0.336 \pm 0.103$
$P(\Lambda+\bar{\Lambda})$	$0.136 \pm 0.117 \pm 0.151$	$0.361 \pm 0.199 \pm 0.241$	$-.087 \pm 0.176 \pm 0.068$	$0.022 \pm 0.246 \pm 0.356$
$P(\Lambda(-)\bar{\Lambda})$	$0.073 \pm 0.117 \pm 0.029$	$-.047 \pm 0.198 \pm 0.049$	$0.187 \pm 0.174 \pm 0.128$	$0.044 \pm 0.245 \pm 0.191$
$P\alpha(K_s)$	$0.004 \pm 0.024 \pm 0.016$	$0.020 \pm 0.033 \pm 0.049$	$-.028 \pm 0.040 \pm 0.065$	$0.033 \pm 0.065 \pm 0.106$

4.7 Correlations

Certain details of fragmentation can be studied using events with two $\Lambda/\bar{\Lambda}$ decays (unlike-type ($\Lambda\bar{\Lambda}$) and like-type ($\Lambda\Lambda$ and $\bar{\Lambda}\bar{\Lambda}$)). The question of baryon

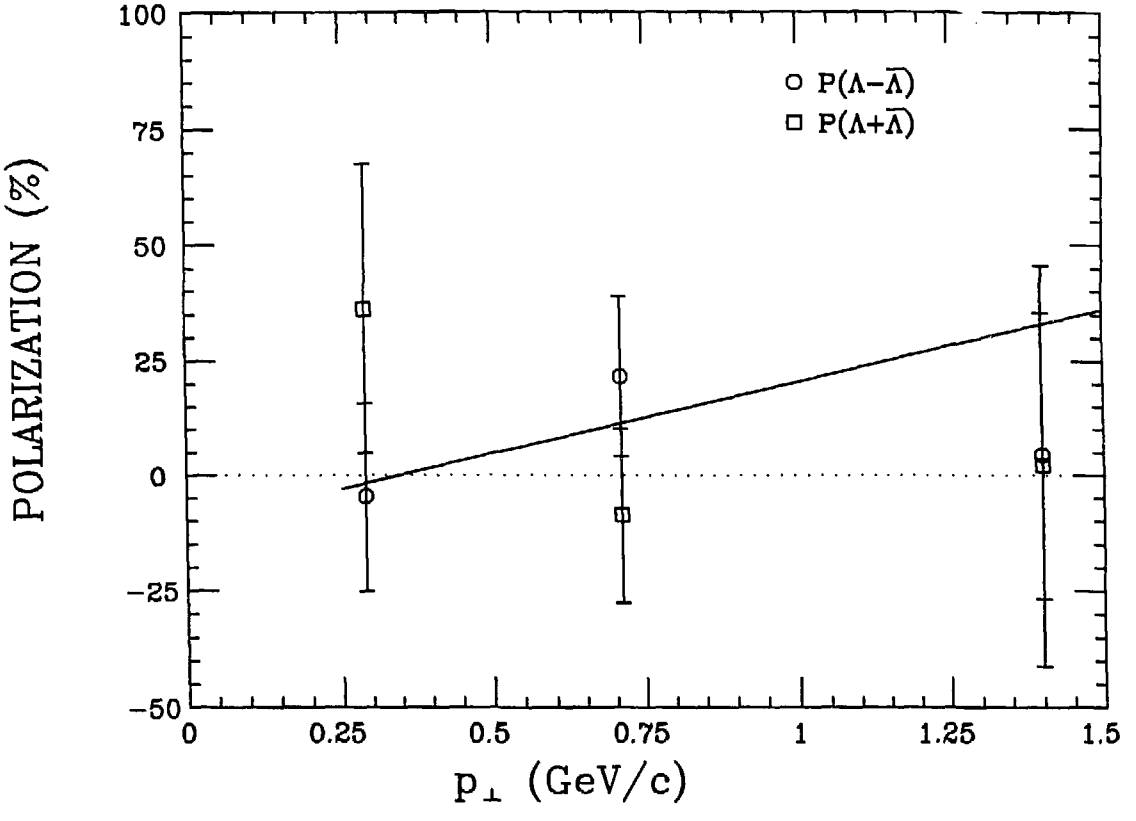

Figure 4.13. Polarization P for the $\Lambda+\bar{\Lambda}$ and $\Lambda(-)\bar{\Lambda}$ data. The straight line is a fit to the $p \rightarrow \Lambda$ and $\bar{p} \rightarrow \bar{\Lambda}$ data (combined) from Figure 4.12. Error are from the combination of statistical and systematic uncertainties (see Table 4.5) added in quadrature.

conservation locally in jets and possible correlations in production angle will be addressed using the data described above (see Table 4.1).

To determine the background from one or two fake $\Lambda/\bar{\Lambda}$ candidates, we first look at the $p\pi$ invariant mass distributions. Figure 4.14 shows a scatter plot of $m(p\pi)_1$ vs $m(p\pi)_2$ for like-type events (the choice of the axis to plot $m(p\pi)_1$ and $m(p\pi)_2$ along is random) and Figure 4.15 shows the unlike-type events (m_Λ is plotted along the x-axis and $m_{\bar{\Lambda}}$ along the y-axis). We will look at correlations for those events where both candidates are within the dotted lines ($1.106\,\mathrm{GeV}/c^2 \leq m(p\pi) \leq 1.126\,\mathrm{GeV}/c^2$) and within the dot-dashed lines ($1.111\,\mathrm{GeV}/c^2 \leq m(p\pi) \leq 1.121\,\mathrm{GeV}/c^2$).

To calculate the background to Figure 4.14 (like-type events) inside dotted lines we look at the absolute value of the difference between $m(p\pi)$ and the known Λ mass of $1.1156\,\mathrm{GeV}/c^2$ for both candidates (Δm_1 and Δm_2). Figure 4.16 shows the scatter plot of Δm_x versus Δm_y where the choice of which candidate (Δm_1 or Δm_2) gets plotted along which axis is random. The histograms show the projection onto the x-axis for $\Delta m_y \leq 10MeV$ and onto the y-axis for $\Delta m_x \leq 10MeV$. The background in the region $\Delta m_x \leq 10MeV$ and $\Delta m_y \leq 10MeV$ is due to either a real like-type event ($N_{like}(real, real)$), an event with one real $\Lambda/\bar{\Lambda}$ and one fake, ($N_{like}(real, fake)$), or an event with two fakes ($N_{like}(fake, fake)$). We estimate the number of $N_{like}(real, fake)$ events by averaging over the intervals $[\Delta m_y \leq 10MeV$, $10MeV \leq \Delta m_x \leq 50MeV]$ and $[\Delta m_x \leq 10MeV$, $10MeV \leq \Delta m_y \leq 50MeV]$ to get $N_{like}(real, fake) = (42 \pm \sqrt{42})/8 = 5 \pm 1$ for the 8 bins of width $10MeV$. The number of $N_{like}(fake, fake)$ events is estimated by counting the number of events in the interval $[10MeV \leq \Delta m_x \leq 50MeV$, $10MeV \leq \Delta m_y \leq 50MeV]$ and dividing by 16 to get $N_{like}(fake, fake) = 1 \pm 1$. Subtracting this background leaves $N_{like}(real, real) = (12 \pm \sqrt{12}) - (5 \pm 1) - (1 \pm 1) = 6 \pm 4$ events. We estimate the systematic uncertainty

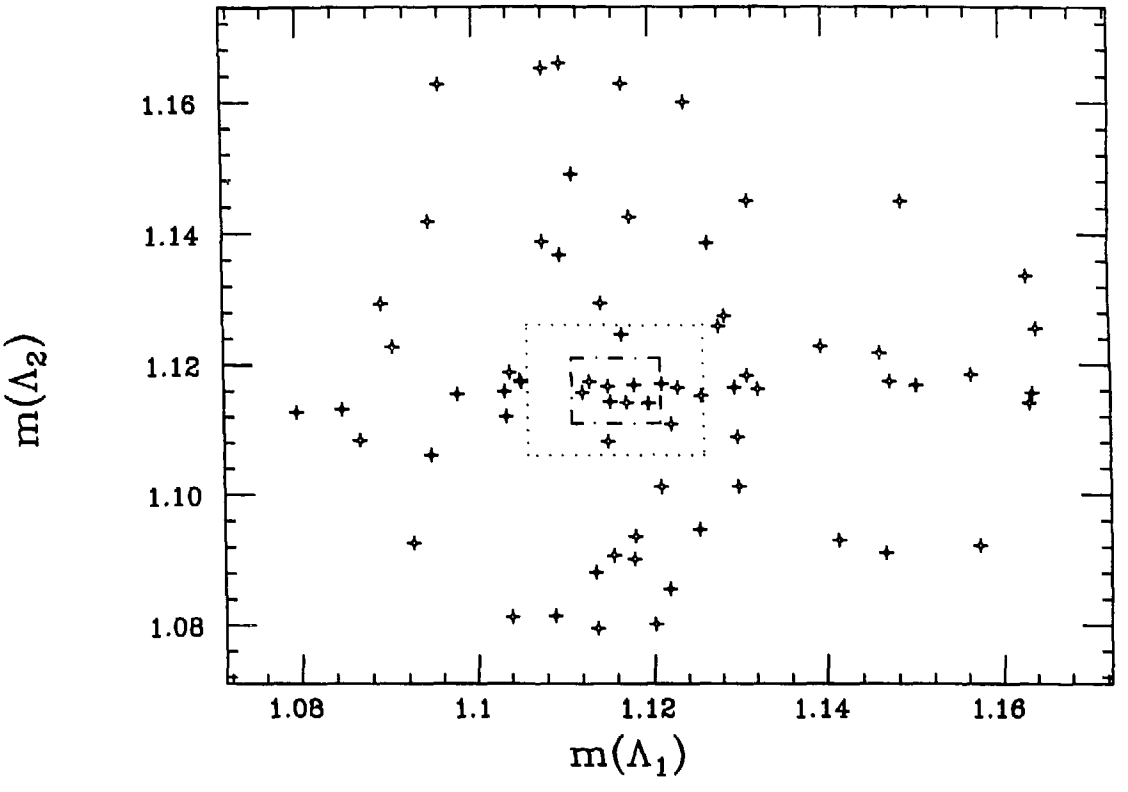

Figure 4.14. Correlations in $m(p\pi)$ for events with two candidates of the same type ($\Lambda\Lambda$ and $\bar{\Lambda}\bar{\Lambda}$). Points inside the dotted line have 1.106 GeV $/c^2 \leq m(p\pi) \leq$ 1.126 GeV $/c^2$ and points inside the dot-dashed line have 1.111 GeV $/c^2 \leq m(p\pi) \leq$ 1.121 GeV $/c^2$.

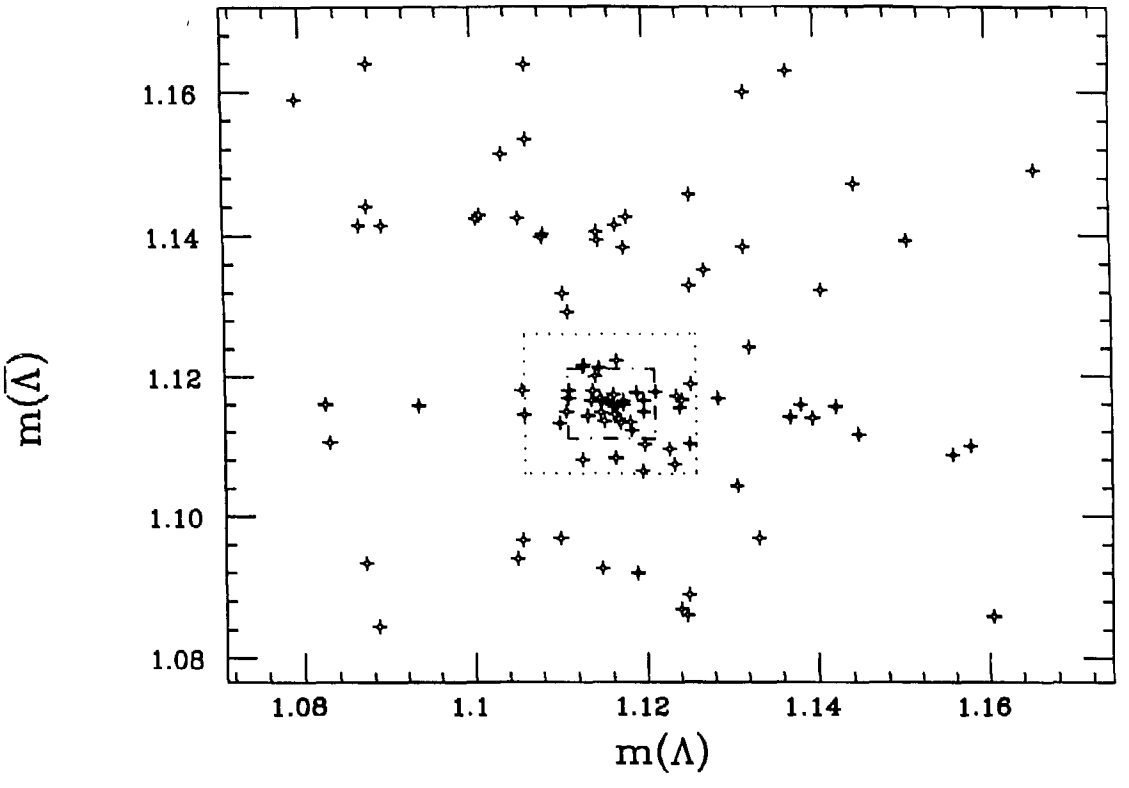

Figure 4.15. Correlations in $m(p\pi)$ for events with two candidates of a different type ($\Lambda\bar{\Lambda}$). Points inside the dotted line have $1.106\,\mathrm{GeV}/c^2 \leq m(p\pi) \leq 1.126\,\mathrm{GeV}/c^2$ and points inside the dot-dashed line have $1.111\,\mathrm{GeV}/c^2 \leq m(p\pi) \leq 1.121\,\mathrm{GeV}/c^2$. $m(\bar{\Lambda})$ is plotted along the y-axis and $m(\Lambda)$ along the x-axis.

to be of the same order as the statistical uncertainty to arrive at the value of $N_{like}(real, real) = 6 \pm 4 \pm 4$.

To calculate the background in Figure 4.15 (unlike-type events) we employ the same method (see Figure 4.17) as in the like-type events. We find $N_{unlike}(real, fake) = 4 \pm 1$ and $N_{unlike}(fake, fake) = 2 \pm 1$. Thus, for the unlike-type events $N_{unlike}(real, real) = (45 \pm \sqrt{45}) - (4 \pm 1) - (2 \pm 1) = 39 \pm 7$. We assume the same systematic uncertainty of ± 4 as in the like-type case and get $N_{unlike}(real, real) = 39 \pm 7 \pm 4$. This is almost a 5σ effect, and we therefore have confidence that we are indeed seeing a signal.

To investigate correlations in like-type and unlike-type events, we require both candidates have $1.106\text{GeV} \leq m(p\pi) \leq 1.126\text{GeV}$, defined as "loose cuts" (inside dotted lines of Figure 4.14 and Figure 4.15). We also look at correlations with the more restrictive requirement of $1.111\text{GeV} \leq m(p\pi) \leq 1.121\text{GeV}$, defined as "tight cuts" (inside dotdashed lines of Figure 4.14 and Figure 4.15). Correlations in jets are investigated through the quantities $\cos\xi \equiv (\vec{p}_1 \cdot \vec{p}_2)/(p_1 p_2)$ where p_1 and p_2 refer to the momenta of the two candidates, $\Delta Y \equiv \mid Y_1 - Y_2 \mid$ (again subscripts 1 and 2 refer to the two candidates) where Y is the rapidity along the sphericity axis, and $\Delta\phi \equiv \phi_1 - \phi_2$ where ϕ is the angle of the candidate momentum in the plane perpendicular to the sphericity axis. Since we see that the number of real like-type ($\Lambda\Lambda$ and $\bar{\Lambda}\bar{\Lambda}$) events in the region of interest is consistent with 0, we can consider this a background for the unlike-type ($\Lambda\bar{\Lambda}$) events. Figure 4.18 shows the $\cos\xi$ distribution for both like-type and unlike-type events in the two mass regions. To subtract the background, we employ the same method used above (using the $N(real, real)$ events and subtracted the properly weighted $N(real, fake)$ and $N(fake, fake)$ events). In Figure 4.19 we again see evidence of baryon correlation. Correlations in rapidity (ΔY) can be seen in Figure 4.20

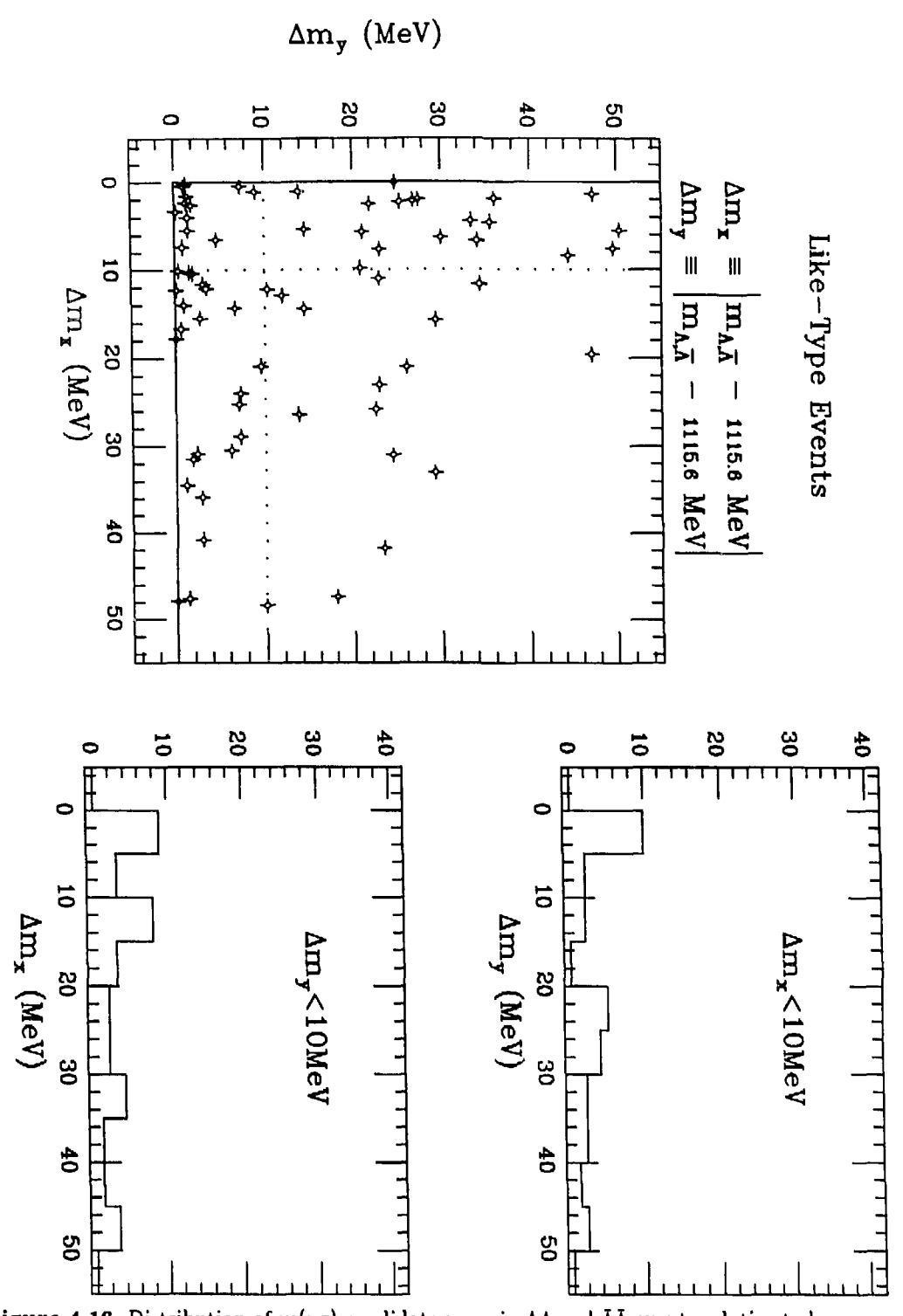

Figure 4.16. Distribution of $m(p\pi)$ candidate mass in $\Lambda\Lambda$ and $\bar{\Lambda}\bar{\Lambda}$ events relative to know mass (1.1156 GeV $/c^2$). Dotted lines delineate $\pm$ 10MeV. Histograms are projections onto x-axis and y-axis for $\mid m(p\pi) - 1115.6 MeV \mid \leq 10 MeV$. The choice of which candidate of the two gets plotted along which axis is random.

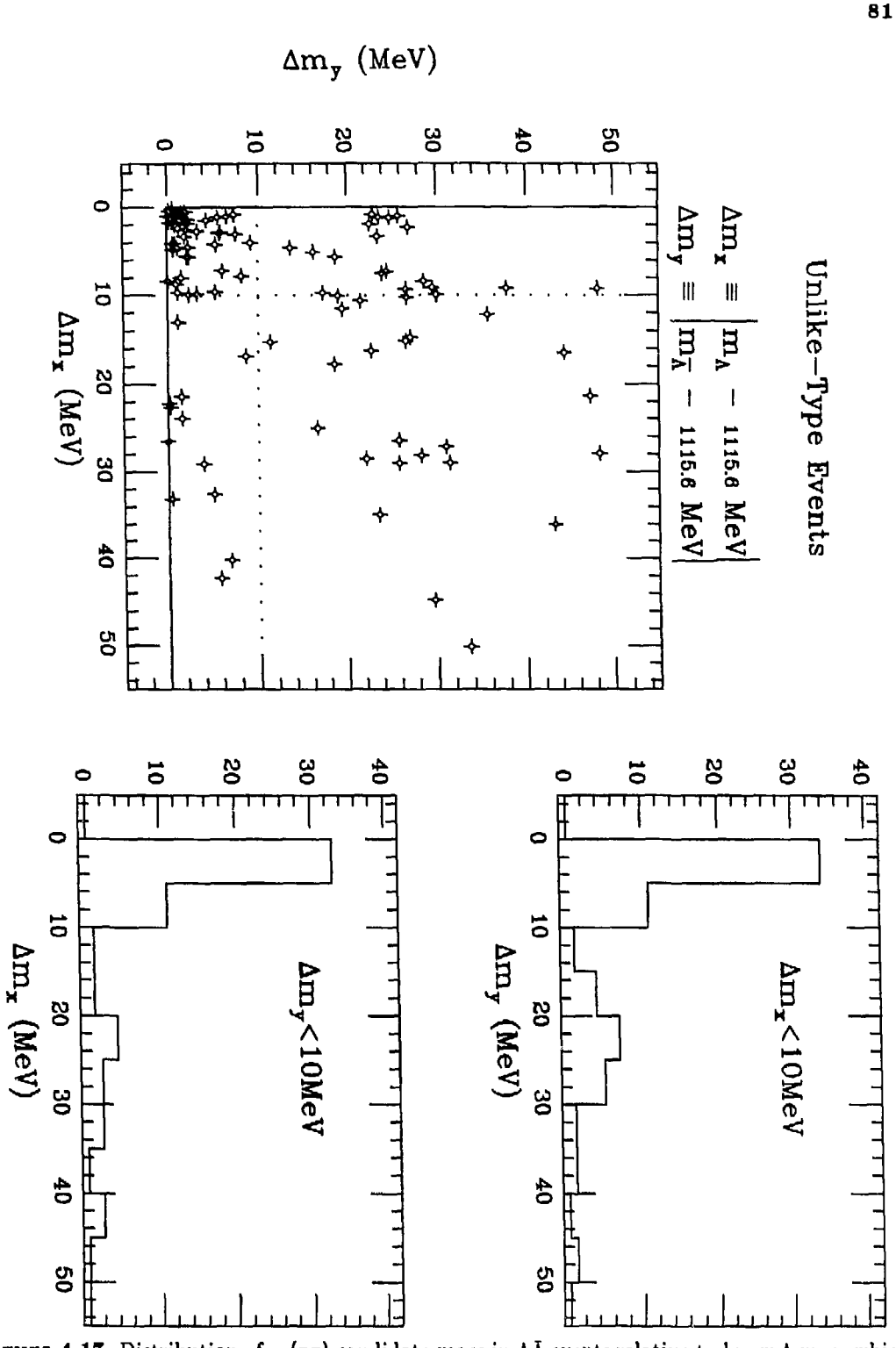

Figure 4.17. Distribution of $m(p\pi)$ candidate mass in $\Lambda\bar{\Lambda}$ events relative to know Λ mass which is (1.1156 GeV $/c^2$). Dotted lines delineate $\pm$ 10MeV. Histograms are projections onto x-axis and y-axis for $|\ m(p\pi)$ -- $1115.6MeV\ | \leq 10MeV$. The $\bar{\Lambda}$ candidates are plotted along the y-axis (Δm_y) and the Λ candidates are plotted along the x-axis (Δm_x).

for both like-type and unlike-type events and for the two mass regions. The grouping in the region $\Delta Y \sim 0$ and $\cos\xi \sim 1$ is due to the fact that for events where both candidates are produced in the same jet ($\cos\xi > 0$) the sign of the rapidity is the same and so ΔY would cluster around 0. Correlations in angle between the two candidates in the plane perpendicular to the sphericity axis ($\Delta\phi$) can be seen in Figure 4.21. We see no evidence of any strong correlations.

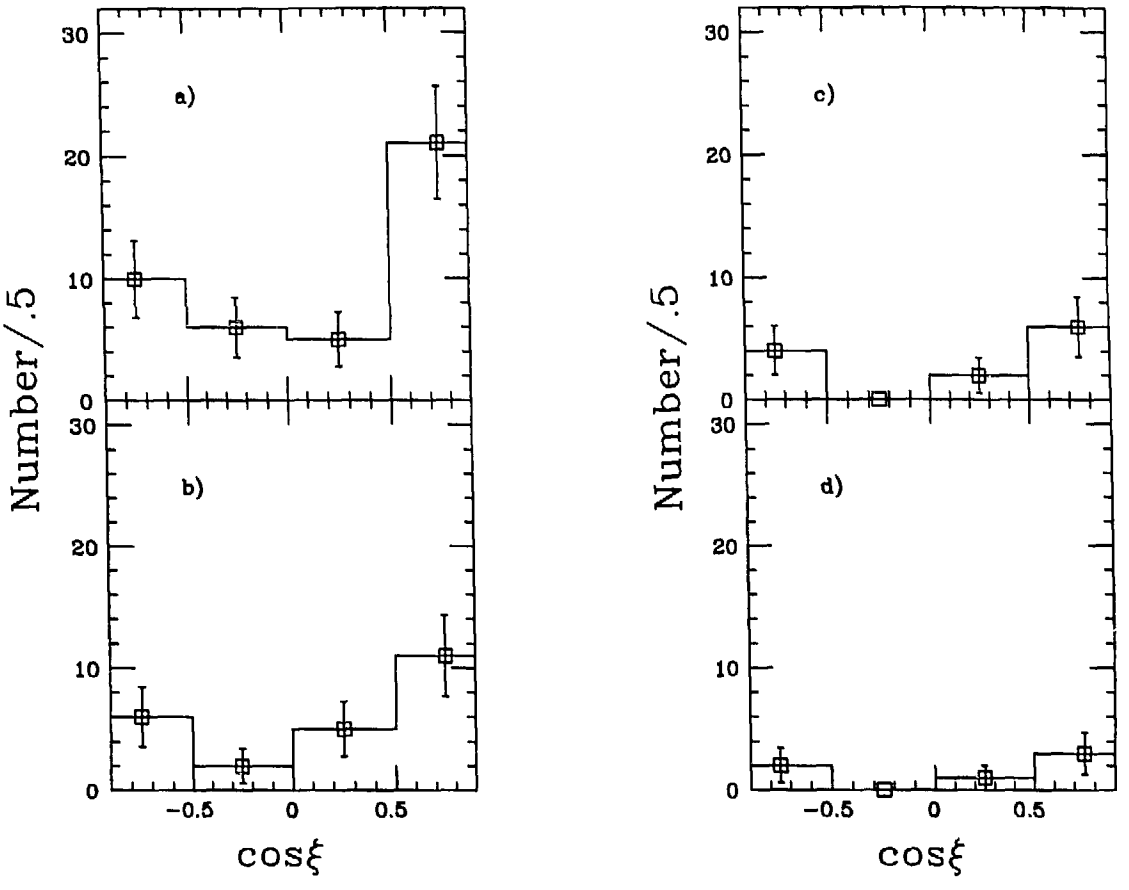

Figure 4.18. Correlations in angle between the two candidates for: unlike-type ($\Lambda\bar{\Lambda}$) events with a) "loose cuts" and b) "tight cuts"; and like-type events with c) "loose cuts" and d) "tight cuts" (see previous definitions). $\cos\xi \equiv (\vec{p}_1 \cdot \vec{p}_2)/(p_1 p_2)$.

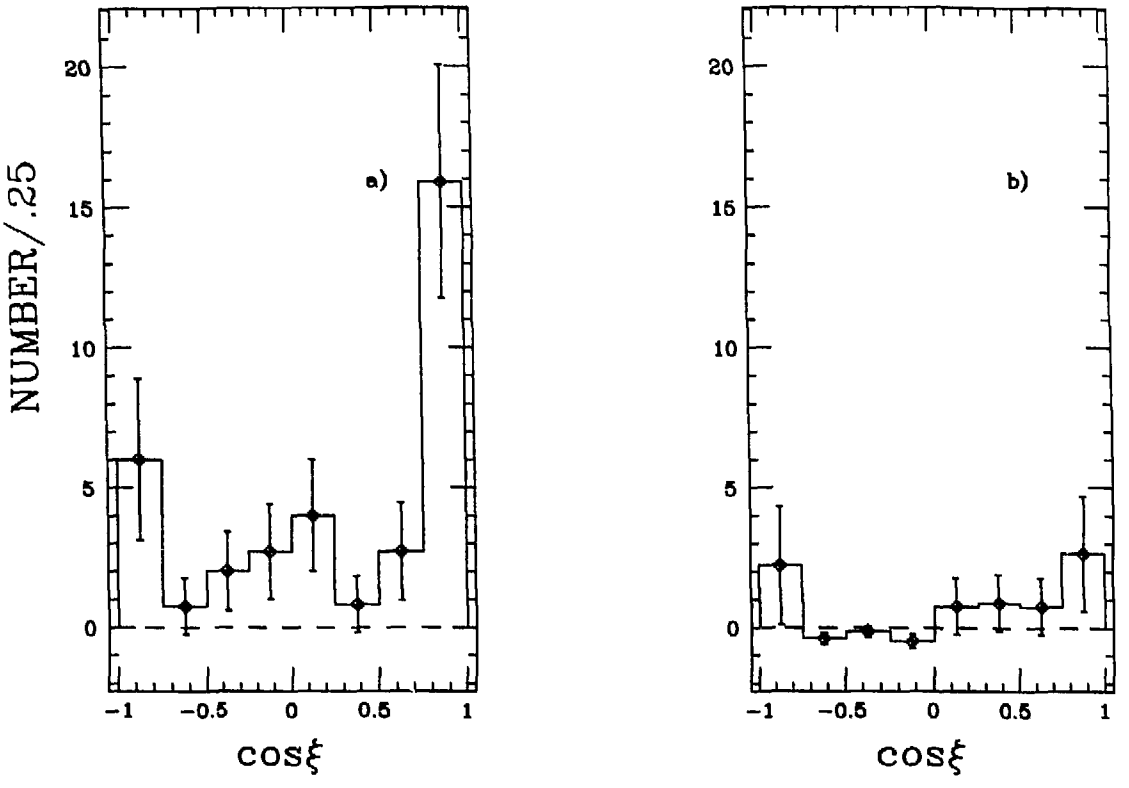

Figure 4.19. $\cos\xi$ distributions after background subtraction for both a) unlike-type and b) like-type events. $\cos\xi$ is the angle between the two candidates. Note the 0 offset.

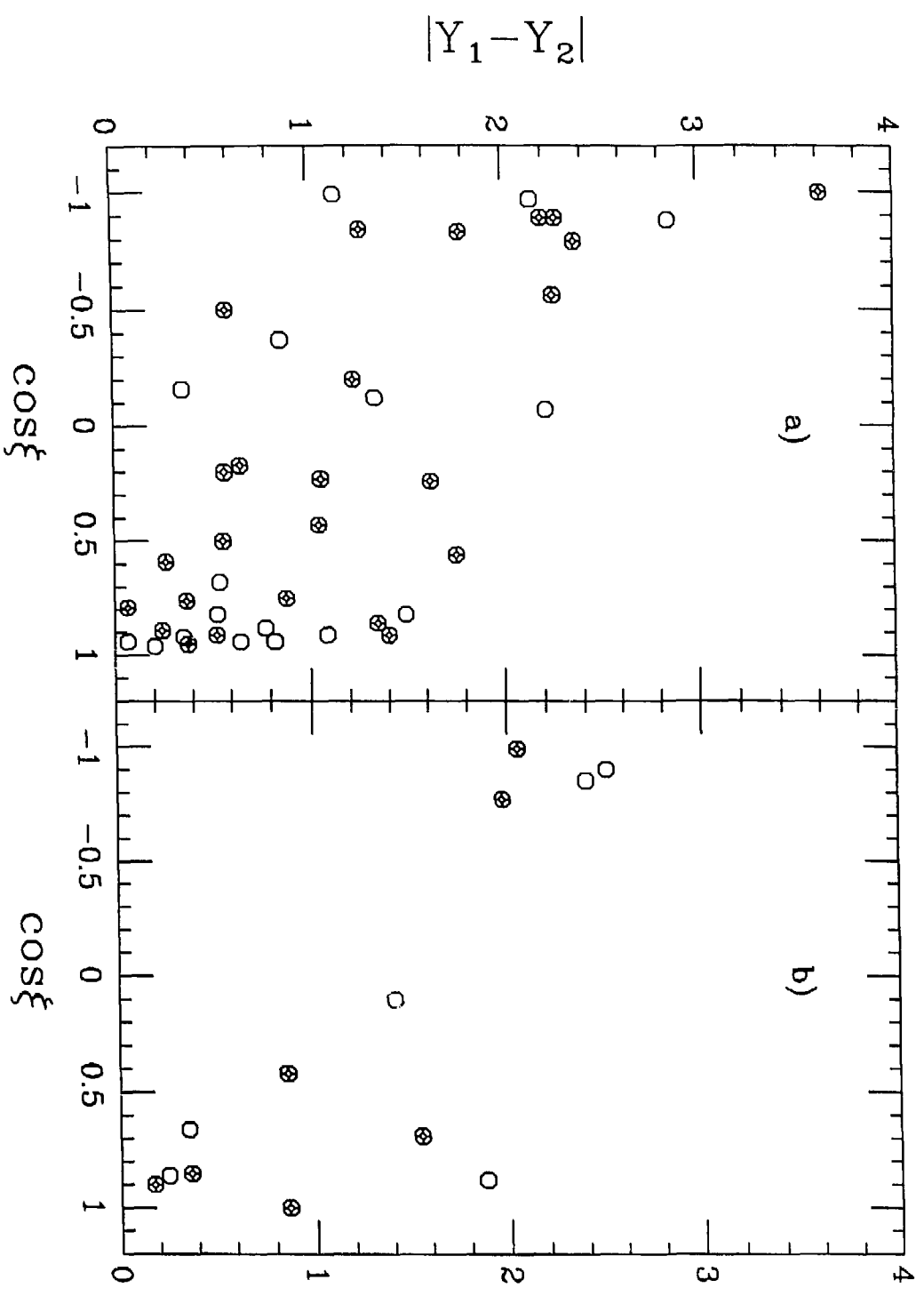

Figure 4.20. Absolute value of difference in rapidity ($| Y_1 - Y_2 |$) relative to sphericity axis versus cosine of angle between the two candidates ($\cos \xi$) for a) unlike-type events ($\Lambda\bar{\Lambda}$) and b) like-type events ($\Lambda\Lambda$ and $\Lambda\bar{\Lambda}$). All points have 1.106 GeV $/c^2 \leq m(p\pi) \leq$ 1.126 GeV $/c^2$. Points plotted with crosses have 1.111 GeV $/c^2 \leq m(p\pi) \leq$ 1.121 GeV $/c^2$.

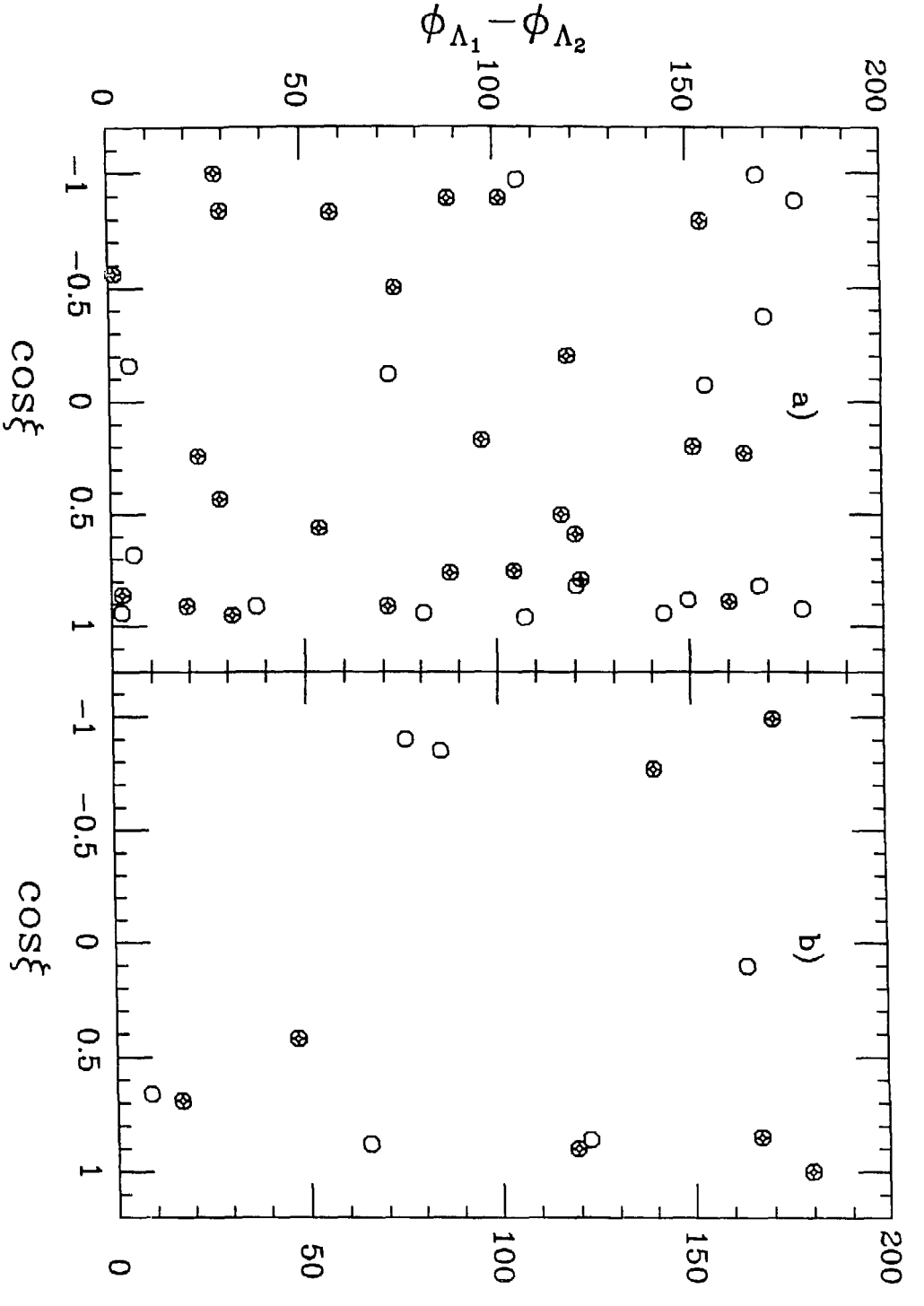

Figure 4.21. Angle between the two candidates in the plane perpendicular to the sphericity axis ($\Delta\phi$) versus cosine of angle between the two candidates in the detector ($\cos\xi$) for a) unlike-type events ($\Lambda\bar{\Lambda}$) and b) like-type events ($\Lambda\Lambda$ and $\bar{\Lambda}\bar{\Lambda}$). All points have 1.106 GeV $/c^2 \leq m(p\pi) \leq$ 1.126 GeV $/c^2$. Points with crosses have 1.111 GeV $/c^2 \leq m(p\pi) \leq$ 1.121 GeV $/c^2$.

5. Conclusion

We have measured the inclusive cross-section $\sigma(e^+e^- \rightarrow \Lambda/\bar{\Lambda}X)$ to be $82.5 \pm 4.5 \pm 9.8pb$ and the hadronic rate

$$R_{\Lambda/\bar{\Lambda}} = \frac{\sigma(e^+e^- \rightarrow \Lambda/\bar{\Lambda}X)}{\sigma(e^+e^- \rightarrow HADRONS)}$$
$$= .200 \pm .011 \pm .024$$

where in both measurements the first uncertainty is from statistics and the second from systematics. We have also measured the differential cross-sections $d\sigma/dp$ (see Figure 4.8) and $(1/\beta)(d\sigma/dx_{\Lambda/\bar{\Lambda}})$ (see Figure 4.9) where $x_{\Lambda/\bar{\Lambda}}$ is the energy of the $\Lambda/\bar{\Lambda}$ in units of the beam energy and find that the distributions compare favorably with other experiments. A search for polarization yields a result consistent with zero (no effect), and this rules out any statement on results of a test of CP invariance. Finally, we look at events with a pair of candidates (unlike-type pairs $\Lambda\bar{\Lambda}$ and like-type pairs $\Lambda\Lambda$ and $\bar{\Lambda}\bar{\Lambda}$) and find a tendency for the events with an unlike-type pair ($\Lambda\bar{\Lambda}$) to be produced in the same jet, but see no indication of any correlations in the production angle in the plane perpendicular to the jet axis.

Appendix A. Calculation of Inclusive $\Lambda/\bar{\Lambda}$ Hadronic Rate

Simulation of the production of hadrons in $e^+e^- \rightarrow q\bar{q}$ events employs quite complicated algorithms. To get a visual feel for this simulation, we use as a vehicle the calculation of the hadronic rate for producing $\Lambda/\bar{\Lambda}$.

In order to produce Λ and $\bar{\Lambda}$ baryons, one needs both an s quark and a di-quark pair. For the purpose of calculation, we distinguish between events where the $\Lambda/\bar{\Lambda}$ comes entirely from the "sea" and events where the $\Lambda/\bar{\Lambda}$ comes from the primary quark.

- If the $\Lambda/\bar{\Lambda}$ comes entirely from the "sea", we need to either produce a di-quark pair $ud\bar{d}\bar{u}$ (probability $P(ud) \sim .1$) and combine with a strange quark pair $s\bar{s}$ (probability $P(s) \sim .3$) or produce a strange di-quark pair $us\bar{s}\bar{u}$ (probability $P(us) \sim P(ud)P(s) \sim .03$) to combine with a quark pair $d\bar{d}$.
- The $\Lambda/\bar{\Lambda}$ can contain the primary quark from $e^+e^- \rightarrow q\bar{q}$ (u, d, s directly or decays of b, c into s). For u or d direct quark production (probability $P_u = 4/11$ and $P_d = 1/11$), the $\Lambda/\bar{\Lambda}$ can come from combining the produced isospin quark with a strange di-quark pair ($ds\bar{s}\bar{d}$ or $us\bar{s}\bar{u}$). For direct production of $s\bar{s}$ quarks (probability $P_s = 1/11$), the $\Lambda/\bar{\Lambda}$ could come from the combination of one of the direct quarks with an isospin di-quark pair. If the heavy c and b quarks are produced (with probabilities $P_c = 4/11$ and $P_b = 1/11$), the $\Lambda/\bar{\Lambda}$ would come from the combination of the primary quark with the isospin di-quark with the resulting heavy baryon decaying into the Λ.

We also must take into account the combinatoric factors (each channel has two ways of occurring (see figures)), the number of $\Lambda/\bar{\Lambda}$'s produced in each of the above mentioned cases, and include terms to second order when appropriate (production of Λ and $\bar{\Lambda}$ in the event). Thus, if one assumes that the $\Lambda/\bar{\Lambda}$ makes up 1/2 of all singly-strange baryons (3/4 of all singly-strange baryons are Σ's,

however $Br(\Sigma^0 \rightarrow \Lambda\gamma) = 100\%$) the number of $\Lambda/\bar{\Lambda}$ per hadronic event can be estimated to be

$$
\begin{aligned}
r &= r(sea) + r(direct) \\
&= \frac{1}{2}P(ud)P(s)\ ^{(a)} + 2(\frac{1}{2})^2P(ud)P(s)P(s)\ ^{(b)} + 2(\frac{1}{2})^2P(ud)P(ud)P(s)\ ^{(c)} + \\
&\quad 2(\frac{1}{2})^2P(us)\ ^{(d)} + 2(\frac{1}{2})^2(P_u + P_d)P(us)P_{direct}\ ^{(e)} + \frac{1}{2}P_sP(ud)P_{direct}\ ^{(f)} + \\
&\quad 2(\frac{1}{2})^2P_sP(ud)P_{direct}P(s)\ ^{(g)} + \frac{1}{2}P_cBr_{c\rightarrow s}P(ud)P_{direct}\ ^{(h)} + \\
&\quad 2(\frac{1}{2})^2P_cBr_{c\rightarrow s}P(ud)P_{direct}P(s)\ ^{(i)} + \frac{1}{2}P_bBr_{b\rightarrow c}Br_{c\rightarrow s}P(ud)P_{direct}\ ^{(j)} + \\
&\quad 2(\frac{1}{2})^2P_bBr_{b\rightarrow c}Br_{c\rightarrow s}P(ud)P_{direct}P(s)\ ^{(k)}
\end{aligned}
$$

where the superscripts refer to the forthcoming diagrams and the "2" refers to the number of strange baryons produced in each diagram and the $\frac{1}{2}$ refers to the probability of producing a $\Lambda/\bar{\Lambda}$ relative to all possible singly-strange baryons. An overall factor of 2 is implicitly included in the above equation to take care of the combinatoric possibilities for each diagram. Table A.1 summarizes the probabilities used in the above equation. P_{direct} is the probability of combining a di-quark pair with the primary quark, and is estimated to be 0.25 from naive combinatoric considerations. $Br_{c\rightarrow s} = .25 \pm .10$ is the branching ratio for the c baryon[41] to decay to the Λ and $Br_{b\rightarrow c} \sim .3$ is the branching ratio for the b baryon to decay into the c baryon[42]. We calculate $r \sim .08$ when including all the above factors. Table A.2 summarizes the results of varying the above parameters. Recent measurements have $R \sim .2$. We subtract the Ξ hadronic rate[43] (since $\Xi \rightarrow \Lambda$ always) of $.020 \pm .008 \pm .004$ from $R_{\Lambda/\bar{\Lambda}}$ to get $R \sim .18$. We note that for a $P(us)$ value near the upper end of the assumed range agreement with the experimental result can be achieved. Figures follow.

Table A.1. Quantities used in calculating $\Lambda/\bar{\Lambda}$ hadronic rate.

Quantities	Description	Values
P_u, P_d, P_s, P_c, P_b	Direct production	$4/11, 1/11, 1/11, 4/11, 1/11$
$P(ud)$	Di-quark suppression	0.1
$P(s)$	Strange quark suppression	0.3
$P(us)$	Strange di-quark suppression	0.03 [26]
P_{direct}	Di-quark combines with primary quark	.25
$Br_{c\to s}$	$Br(c - baryon \to \Lambda/\bar{\Lambda})$	0.25 ± 0.10
$Br_{b\to c}$	$Br(b - baryon \to c - baryon)$	0.3

Table A.2. Dependency of $R_{\Lambda/\bar{\Lambda}}$ on parameters.

Parameter	Range	Change in R
$P(ud)$	0.05 – 0.15	0.06 – 0.10
$P(s)$	0.2 – 0.4	0.06 – 0.10
$P(us)$	0.01 – 0.10	0.06 – 0.16
P_{direct}	0.1 – 1.0	0.07 – 0.10
$Br_{c\to s}$	0.01 – 1.00	0.08 – 0.09
$Br_{b\to c}$	0.0 – 1.0	no change

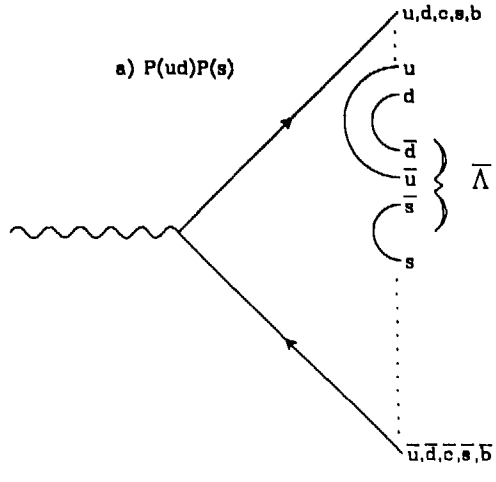

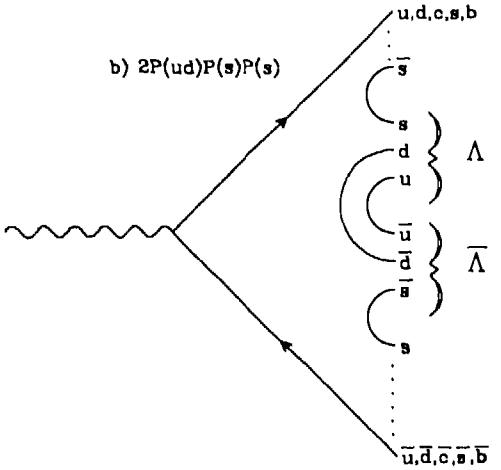
b) 2P(ud)P(s)P(s)
u,d,c,s,b
s̄
s
d
u
Λ
ū
d̄
Λ̄
s̄
s
ū,d̄,c̄,s̄,b̄

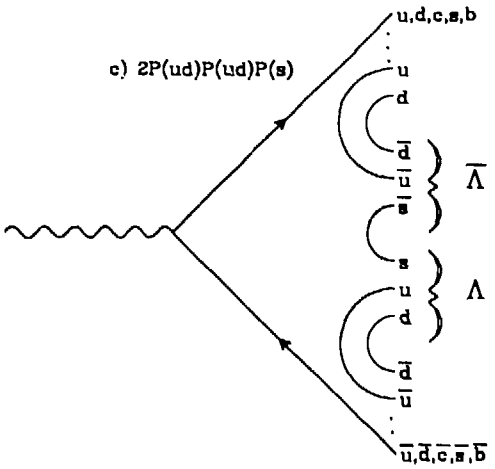
c) 2P(ud)P(ud)P(s)
u,d,c,s,b
u
d
d̄
ū
Λ̄
s̄
s
u
Λ
d
d̄
ū
ū,d̄,c̄,s̄,b̄

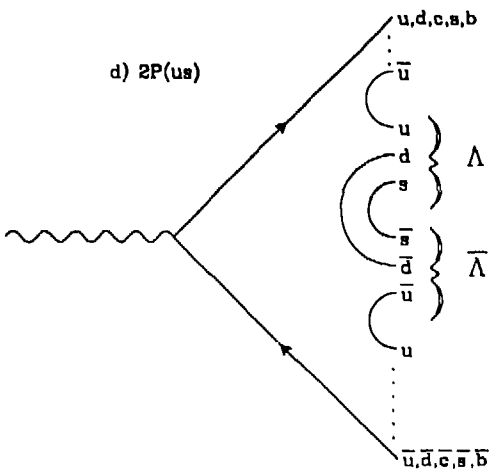
d) 2P(us)
u,d,c,s,b
ū
u
d
s
Λ
s̄
d̄
Λ̄
ū
u
ū,d̄,c̄,s̄,b̄

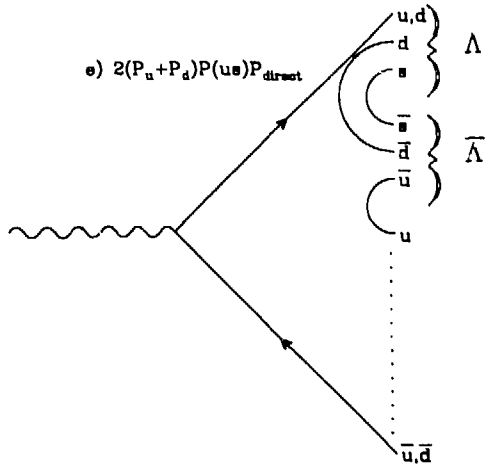
e) $2(P_u+P_d)P(us)P_{direct}$
u,d
d
s
$\bar{s}$
$\bar{d}$
$\bar{u}$
u
$\bar{u},\bar{d}$
Λ
$\bar{\Lambda}$

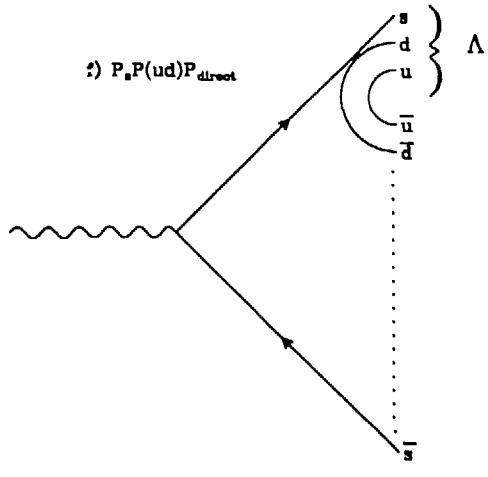
f) $P_sP(ud)P_{direct}$
s
d
u
$\bar{u}$
$\bar{d}$
$\bar{s}$
Λ

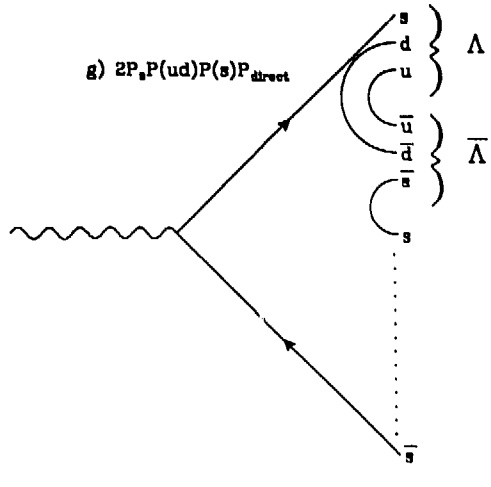
g) $2P_sP(ud)P(s)P_{direct}$
s
d
u
$\bar{u}$
$\bar{d}$
$\bar{s}$
s
$\bar{s}$
Λ
$\bar{\Lambda}$

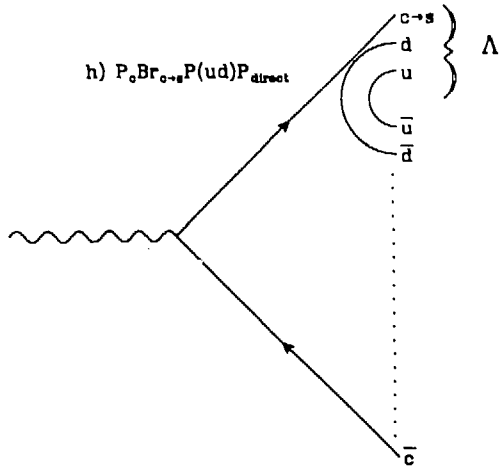
h) $P_c Br_{c\to s} P(ud) P_{direct}$
c→s
d
u
ū
d̄
Λ
c̄

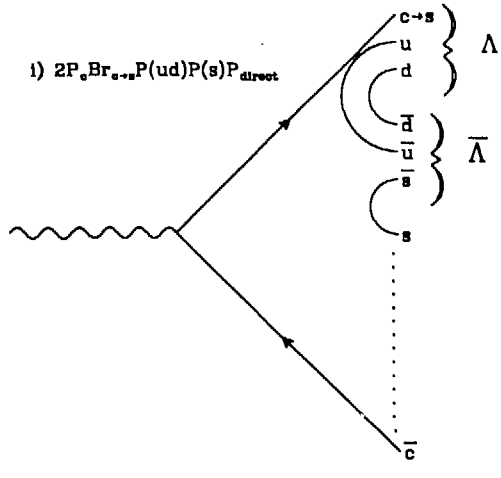
i) $2P_c Br_{c\to s} P(ud) P(s) P_{direct}$
c→s
u
d
d̄
ū
s̄
s
Λ
Λ̄
c̄

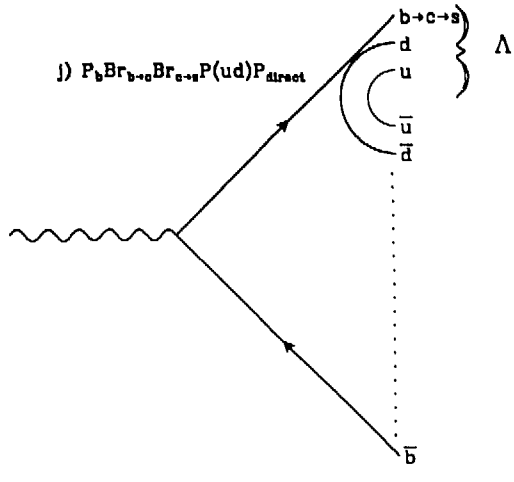
j) $P_b Br_{b\to c} Br_{c\to s} P(ud) P_{direct}$
b→c→s
d
u
ū
d̄
Λ
b̄

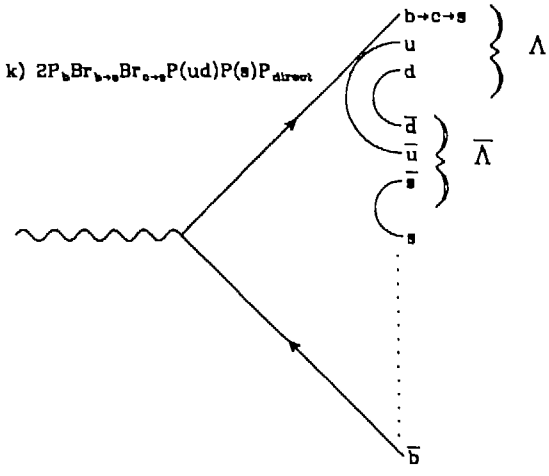
k) $2P_bBr_{b\to s}Br_{c\to s}P(ud)P(s)P_{direct}$
b→c→s
u
d
Λ
$\bar{d}$
$\bar{u}$
$\bar{\Lambda}$
$\bar{s}$
s
$\bar{b}$

REFERENCES

1. P. A. M. Dirac, *Proc. Roy. Soc. (London) A* **177**, 610 (1928)
2. R. P. Feynman, *Phys. Rev.* **76**, 749, 746 (1949)
3. M. E. Levi *et al.*, *Phys. Rev. Lett.* **51**, 1941 (1983)
4. R. Field and R. Feynman, *Nucl. Phys. B* **136**, 1 (1978)
5. B. Andersson *et al.*, *Phys. Rep.* **97**, 31 (1983)
6. C. Peterson, D. Schlatter, I. Schmitt and P.M. Zerwas, *Phys. Rev. D* **27**, 105 (1983)
7. H. Schellman, thesis, University of California, Berkeley, LBL-18699 (1984)
8. G. Altarelli and G. Parisi, *Nucl. Phys. B* **126**, 298 (1977)
9. F. A. Berends and R. Kleiss, *Nucl. Phys. B* **177**, 239 (1981)
10. SLAC Report No. 146 and LBL Report No. 750, April 1972
11. SLAC Report No. 171 and LBL Report No. 2688, April 1974
12. D. Amidei, thesis, University of California, Berkeley, LBL-17795 pp. 14-26 (1984)
13. R. Schindler, thesis, Stanford University, SLAC-219 pp. 35-53 (1979)
14. M. Nelson, thesis, University of California, Berkeley, LBL-16724 pp. 44-46 (1983)
15. P. C. Rowson, thesis, University of California, Berkeley, LBL-20463 pp. 17-20 (1983)
16. P. C. Rowson, thesis, University of California, Berkeley, LBL-20463 pp. 41-44 and pp. 62-64 (1983)
17. G. Hanson *et al.*, *Phys. Rev. Lett.* **35** , 1609 (1975)
18. J. Patrick *et al.*, *Phys. Rev. Lett.* **49**, 1229 (1982)
19. J. Patrick, thesis, University of California, Berkeley, LBL-14585 (1982)
20. Reviews of Modern Physics, Vol 56 Num. 2 Part II page S64 (1984)
21. For more on the details, see internal memos Technical Note TG-232 and TG-234
22. H. Schellman, thesis, University of California, Berkeley, LBL-18699 p. 32 (1984)
23. Nigel Lockyer, MarkII internal memo 21JUNE84
24. C. P. de la Vaissiere *et al.*, *Phys. Rev. Lett.* **54**, 2071 (1985)

25. C. P. de la Vaissiere *et al.*, *Phys. Rev. Lett. (Erratum)* **55**, 263 (1985)

26. P. Baringer *et al.*, *Phys. Rev. Lett.* **56**, 1346 (1986)

27. H. Aihara *et al.*, *Phys. Rev. Lett.* **54**, 274 (1985)

28. D. H. Perkins *Introduction to High Energy Physics* (2nd Ed., Addison Wesley 1982), pp. 237-239.

29. Particle Data Group, *Rev. Mod. Phys.* **56**, 92 (1984)

30. T. D. Lee in *Preludes in Theoretical Physics*, edited by A. deShalit, H. Feshback, and L. Van Hove (North-Holland Publishing Co., Amsterdam, 1966), p. 5.

31. R608 Collaboration (P. Chauvat *et al.*), *Phys. Lett. B* **163**, 273 (1985)

32. S. A. Gourlay *et al.*, *Phys. Rev. Lett.* **56**, 2244 (1986)

33. T. A. Armstrong *et al.*, *Nucl. Phys. B* **262**, 356 (1985)

34. K. Heller *et al.*, *Phys. Rev. Lett.* **41**, 60 (1978)

35. J. Harris *et al.*, *Phys. Rev. Lett.* **47** , 229 (1981)

36. G. Kane, J. Pumplin, and W. Repko, *Phys. Rev. Lett.* **41**, 1689 (1978)

37. B. Andersson, G. Gustafson, and G. Ingelman, *Phys. Lett.* **85B**, 417 (1979)

38. T. A. DeGrand and H. I. Miettinen, *Phys. Rev. D* **24**, 2419 (1981)

39. K. Heller and G. Bunce *et al.*, *Phys. Rev. Lett.* **41**, 607 (1978)

40. Private communications, M. Suzuki (U.C. LBL) and R. Cahn (LBL)

41. K. Abe *et al.*, *Phys. Rev. D* **33**, 1 (1986)

42. $R_{\Lambda/\bar{\Lambda}}$ is insensitive to $Br_{b\to c}$. The value 0.3 is chosen to be close to $Br_{c\to s}$.

43. H. Yamamoto, in *QCD and Beyond*, Proceedings of the 20^{th} Rencontre de Moriond, 1985, Edited by J. Tran Thanh Van, p. 93.